K. Kamalanand, Ph.D.

D. Najumnissa Jamal, Ph.D.

P. Mannar Jawahar, Ph.D.

Editors

Advances in

nano

Instrumentation Systems and Computational Techniques

NOVA

NANOTECHNOLOGY SCIENCE AND TECHNOLOGY

ADVANCES IN NANO INSTRUMENTATION SYSTEMS AND COMPUTATIONAL TECHNIQUES

NANOTECHNOLOGY SCIENCE AND TECHNOLOGY

ADVANCES IN NANO INSTRUMENTATION SYSTEMS AND COMPUTATIONAL TECHNIQUES

K. KAMALANAND

D. NAJUMNISSA JAMAL

AND

P. MANNAR JAWAHAR

EDITORS

CONTENTS

PREFACE

Nanotechnology is the art and science of manipulating atoms, molecules and matter at nanometric length scales, to create new systems, materials, devices and instruments (Kaur et al., 2012). The developed nanometric systems are proved to be faster, robust, light weight, durable and small in size (Roco, 2007). The field of nanotechnology provides encouraging opportunities and challenges for scientists and technologists irrespective of their discipline. The rapidly emerging innovations in nano systems have enabled the creation of new sensors and devices with dramatic improvements in sensitivity and accuracy, along with significant size reductions. In recent years, nanotechnology has been utilized in the multi-disciplinary fields such as medicine, engineering, computing etc. (Bhattacharyya et al., 2009). Nanotechnology and nano engineering stand to produce significant scientific and technological advances in diverse fields including medicine and physiology, automation, space research, and sensor technology. Also, recent advances in computational nanoscience enables scientists and technologists to study nano materials and nano systems more efficiently with the help of mathematical models and simulation techniques (Owens 2018). Further, nano instrumentation is

an emerging technology and has the potential to revolutionize the field of industrial and medical instruments.

This edited book consists of seven excellent chapters highlighting the recent developments in the fields of nanotechnology, instrumentation and computational techniques. The first chapter entitled "Nanopositioning Systems using Piezoelectric Actuators", authored by Sabarianand and Karthikeyan focuses on piezoelectric actuators-based Nano positioning systems. Also, this chapter presents the challenges and control issues on integrating nanopositioning systems using piezoelectric actuators.

The second chapter entitled "Synthesis and Characterizations of Sustainable $Ti/SnO_2-Sb_2O_3/PbO_2$ Electrode using Sol-Gel Electrochemical Combined Coating and Application to Electrochemical Degradation of Methyl Orange" authored by Kannan et al. presents the synthesis of $SnO_2-Sb_2O_3$ oxides doped nano-PbO_2 electrode by sol-gel combined with electrochemical multicoated method from non-aqueous electrolyte solution. The authors have discussed the methods involved and the experimental results, in detail.

In the third chapter entitled "Thermally Induced ZnO Nanoparticles Synthesis through Bulk Addition Method: An Innovative Approach", the authors Praveen Kumar et al. have introduced a new innovative method called instant bulk addition process which leads to the formation of nanoparticles with controlled morphology in large quantity, in a short period of time. The authors have presented experimental results and have provided an extensive comparison between conventional and new methods for synthesis of nano materials.

Computational methods help in the development of several useful applications involving nano materials and instrumentation. The fourth chapter entitled "Automatic Detection of *Malarial parasitema* using Efficient Fractal Analysis" authored by Prabha Sathees, presents an automated technique based on fractals for the detection of four different malarial parasites in microscopic images. The author has presented the needs for automated detection of malarial parasites in blood smear

images along with fractal techniques for achieving high detection accuracy.

The fifth chapter entitled "A Three Tier Pre-Processing Validation for Image Segmentation and Analysis of RBCs in SEM Images" authored by Priya presents the, digital image processing techniques for red blood cells in Scanning Electron Microscopy (SEM) images. The author has presented several computational methods such as Surface Fitting Method (SFM), Multiple Regression Method (MRM) and Bi-dimensional Empirical Mode Decomposition (BEMD)for preprocessing of SEM images and further presents the active contour-based segmentation technique for identification of the contours of the RBCs which can enable shape-based investigation for clinical diagnosis and treatment of blood cell diseases.

In the sixth chapter entitled "Influence of Nano Powder Addition and Emulsification Technique on Engine's Behaviour of a Waste Cooking Oil Based Diesel Engine", the author Senthilkumar Masimalai has experimentally analyzed the influence of emulsification and nano powder addition on the performance and emission characteristics of a diesel engine operating on a waste cooking oil (WCO) of sunflower oil. The author demonstrated that the waste cooking oil can be efficiently utilized in diesel engines by converting it into its solid nano additive emulsion, without much loss in efficiency.

In the last chapter entitled "Synthesis Techniques of Nanostructured Materials and Its Image Analysis for Particle Size Distribution", authored by Padmalaya et al., a detailed description highlighting the image analysis of TEM images for soot nanoparticles using Euclidian distance mapping-surface based scale analysis along with its benefits, is presented.

The editors thank Nova Publishers, the contributing authors and the reviewers who have helped to bring out this unique book on nano instrumentation systems and computational techniques.

REFERENCES

Bhattacharyya, D., Singh, S., Satnalika, N., Khandelwal, A., & Jeon, S. H. (2009). Nanotechnology, big things from a tiny world: a review. *Nanotechnology*, 2(3), 29-38.

Kaur, G., Singh, T., & Kumar, A. (2012). Nanotechnology: a review. *Inter J Edu and Appli Res*, 2(1), 50-53.

Owens, F. J. (2018). *The Physics of Low Dimensional Materials*. World Scientific.

Roco, M. C. (2007). *Handbook on nanoscience, engineering and technology*.

Chapter 1

NANOPOSITIONING SYSTEMS USING PIEZOELECTRIC ACTUATORS

D. V. Sabarianand and P. Karthikeyan[*]

Department of Production Technology,
Madras Institute of Technology, Anna University, Chennai, India

ABSTRACT

Nanopositioning is increasingly relying on piezoelectric actuators. Nanopositioning systems with piezoelectric actuators (piezo-actuated nanopositioners) are compact, high-precision mechatronic devices that are capable of generating mechanical motion with nanometer or sub-nanometer resolution. The piezoelectric actuator based nanopositioning systems are designed to providegreatest possible accuracy and unlimited resolution, but in practice they exhibit inherent non ideal characteristics such as creep, hysteresis and vibration effects that severely degrade its performance. In addition to this nonlinearities, the performance characteristics of nanopositioning system are highly affected by mechanical dynamics/ design of the motion stage, external disturbances and thermal drift due to the temperature variation. This study reveals the

---

[*] Corresponding Author's Email:pkarthikeyan@mitindia.edu.

challenges and control issues on integrating nanopositioning systems using piezoelectric actuators.

INTRODUCTION

A constant demand in achieving higher accuracy and precision in production machinery and other devices has led to the development of different technologies in production industries. Precision engineering emerged from mechanical engineering followed by micromechanics and recently evolved with nanomechanics. The fact of smaller volume per unit alone often opens a new market. Further, the smaller volume per unit enables to combine several functions within one product with an acceptable price and size. On the other hand, the miniaturization of devices enables the development of new functions. Nowadays, industry is quite interested in using precision manufacturing and assembly for small parts with a size ranging from very few millimetres down to micrometres. Also, there exists a worldwide interest in nano tools. Micro-motion devices that can perform very small motions with very high positioning accuracy potentially have wide application in industry. Typical applications are chip assembly in the semiconductor industry (Gaurav Singh Naruka, 2009), cell manipulation in biotechnology (Götze & Pagel, 2007; Lopez-Martinez & Campo, 2011), and automatic surgery in medicine (Stevenson et al., 2010), manufacturing & inspection systems such as laser beam machining in 50nm (Kuang et al., 2016) and SEMin meterology applications (Maroufi & Moheimani, 2016), autofocuses in camera (Xie et al., 2016).

Specific operations of micromanipulation includes positioning (Pinskier et al., 2018), inserting(Laribi et al., 2012), gripping(Jain et al., 2014), injecting (Götze & Pagel, 2007) etc. Among different operations, micro-/nano-positioning is considered as the most important, because

most of the other operations are the extended application of positioning. For example, gripping is implemented by the relative positioning of two gripper tips; puncturing is the positioning of the needle (Laribi et al., 2012). The precision of the used positioning method directly affects the accuracy of the corresponding operation, especially at a small scale at the micro /nano-meter level. Therefore, precision positioning plays a key role in the micromanipulation domain. The majority of conventional positioning stages transmit force and motion by using rigid mechanisms, e.g., joints and linkages, lead screw driving and rack gear driving. Due to the existence of unavoidable friction and backlash between the interconnected rigid components, the positioning accuracy is greatly degraded (Wu & Xu, 2018). Although it is unapparent in large-scale (like centimetre- or meter-level) applications, the inaccuracy caused is significant at the small scale (micro- and nano-meter level). This investigations reveals the issues and its solutions nano postionsing tasks.

PIEZOELECTRIC ACTUATORS

The piezoelectric actuator (PZT) is a well-known commercially available device for managing extremely small displacements in the range of 100 μm. A PZT actuator is an electromechanical device that undergoes a dimensional change when voltage is applied. The conversion of electrical energy into mechanical energy takes place without generating any significant magnetic field or the need for moving electrical contacts. Dimensional changes are proportional to the applied voltage and can therefore be adjusted with extremely high resolution (Jia et al., 2017). PZT actuators can be operated over millions of cycles without wear or deterioration. Their high response speed is limited only by the inertia of the object being moved and the output capability of the electronic driver.

Piezo actuators offer the following advantages:

- Sub-nanometre resolution
- Large force generation
- Sub-millisecond response
- No magnetic fields
- Extremely low steady state power consumption
- No wear and tear
- Vacuum and clean room compatibility

The holding function of the PZT actuator, which is one of the important requirements for any positioning device, depends on the shape of electronic signals which can be made rather accurate. The PZT actuator has its disadvantages: highly nonlinear input/output behaviour, creep, and hysteresis. This disadvantage can be, nevertheless, alleviated with advanced modelling and controlling technologies. Another major disadvantage with the PZT actuator is that it has a very small motion range. There are many ways to amplify the displacement by stacking multiple piezo actuators in different configurations (Lopez-Martinez & Campo, 2011). Although modest motion amplification can be achieved through such means, many of such arrangements are cumbersome and impose a heavy penalty of voltage requirements. The length of a piezo stack is limited due to the position error generated at the end of the stack. The stacking is also limited due to the stress generated in the piezo slice (Ding et al., 2017).

The various linear and rotary piezoelectric actuators commericially available in the market as listed in Table 1 ranging between 10 to 125mm in travel range, resolution in 0.02 to 20 nm and in terms of force in 10 to 2000 N.

Table 1. Various piezoelectric actuators commericially available in the market

S. No.	Web Address	Actuator type	Travel range (mm)	Resolution (nm)	Force (N)
1	https://www.physikinstrumente.com/	Linear (N-470 Piezo Mike)	10 to 125	0.08 to 20	10
		Rotary (UPR-100)	full 360°	0.05	0.5
		Rotary (UPR-120)	full 360°	0.02	2.08
2	http://www.cedrat-technologies.com/	Linear (PPA10M)	11	0.08	1151
		Linear (CAµ10)	60	0.04	4
		Rotary (RSPA30XS)	full 360°	0.11 mrad	5.32
3	https://www.piezosystem.com/	Linear (series N)	123	0.04	500
		Linear (RA 14/24 SG)	50	0.03	2000
		Linear (P18 S08)	18	0.03	200
		Rotary (10SG)	11 mili radian	0.02 µrad	40
4	https://www.piezodrive.com/	Linear (SA series)	120-830	0.05	11-90
		Linear ring actuator (SR Series)	14-30	0.08	1300-3000
5	http://www.johnsonelectric.com/	Linear piezo stages	40-150	0.1-10	16-32
		Rotary piezo stages	full 360	5-100	16-32
6	http://www.dynamic-structures.com/	Linear (FPA series)	80 µm to 2 mm	0.09-0.15	56-300
		Linear (DSM Model I-20)	12	20	15
7	https://www.mide.com/	Linear (PPA-1001)	4-8	0.02	0.2
8	http://www.mechano-transformer.com/	Linear	4.6-48.5 µm	0.08	237-945

NANOPOSITIONING SYSTEMS USING PIEZOELECTRIC ACTUATORS

A 6-degree of freedom (DOF) serial-parallel precision positioning system, which consists of two compact type 3-DOF parallel mechanisms (Cai et al., 2018). Each parallel mechanism is driven by three piezo-electric actuators (PEAs), guided by three symmetric T-shape hinges and three elliptical flexible hinges, respectively. It can extend workspace and improve flexibility of the operation end, which will greatly reduce the assembly errors and improve the positioning accuracy. Furthermore, in order to reduce the tracking error and improve the positioning accuracy (Cai et al., 2018). An experimental master-slave manipulator is investigated, consisting of a 4-DOF hybrid parallel-serial slave mechanism. Internal sensors and kinematic information enable the estimation of slave position and orientation. Master mechanism inverse dynamics control is implemented to offset master mechanism inertia, whilst passivity control guarantees stability. Experimental analysis demonstrates precisions of approximately 30 nm can be achieved during low speed interactions, with intuitive environmental force feedback. With appropriate choice of end-effector, the system could be used for tasks such as the assembly of micro electro mechanical systems (MEMS)(Pinskier et al., 2018).

The nano-positioner can output a two-dimensional motion at a maximum speed of 0.187 mm/s within a 5 mm×5mm workspace. In order to solve the contradiction between the motion velocity and the motion resolution, the coarse and the fine motion modes. The coarse motion and the fine motion are realized based on the power-function-shaped signal and the combined piecewise-curve signal respectively. The performance of the nano-positioner, e.g., the resolution, the velocity and the fluctuation, based on different driving signals. Compared with other nano- positioners, the proposed system in this paper is superior in respect of compact size, high resolution, high

velocity and two switchable motion modes (Dong et al., 2017). The 3-RPR mechanism has three DOF, including two linear translational DOF along the x-y axis and one rotational DOF about the z-axis. The mechanism is composed of three parts: the lower stage, the upper stage and three kinematic chains, which connect the lower and upper stages. The three chains are divided into two groups and are arranged into two perpendicular directions. All three chains possess the same configuration. Each chain includes two revolute joints (R-joint) and one prismatic joint (P-joint) between them (Dong et al., 2016).

A flexure mechanism, which is a monolithic elastic structure that deforms under load to produce extremely high quality motion due to lack of any firction and backlash lies at the heart of the nanopositioning systesms and provides motion guidance. Parallel-kinematic XY designs are well suited for multi-axis nanopositioning because of their ground-mounted actuators, thus avoiding large masses and moving cables. However, due to the lack of a systematic synthesis approach, most existing designs exhibit kinematic or geometric coupling between their motion axes leading to a restricted motion range (Awtar & Parmar, 2010). This error is a consequence of the fact that over a motion range of several millimetres, even a small difference in the actual phase of the two axes leads to a pronounced deviation from the command trajectory. One of the reasons why command tracking in the two-axis control case suffers is a reduction in the controller gain to avoid an unexpected instability.

A novel control strategy for a nonlinear bilateral macro–micro teleoperation system with time delay. Besides position and velocity signals, force signals are additionally utilized in the control scheme and typical nanopositioning systems as shown in Figure 1. This modification significantly improves the poor transparency during contact with the environment. To eliminate external force measurement, a force estimation algorithm is used for the master and slave robots (Amini et al., 2016).
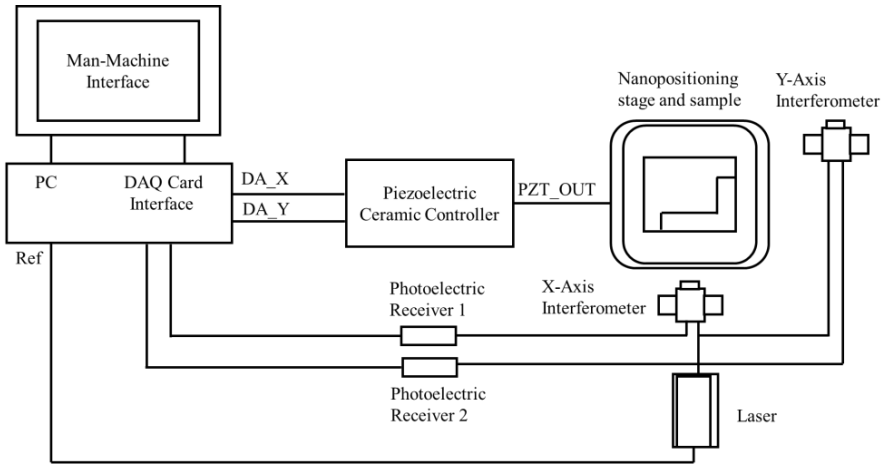
Figure 1. A typical nanopositioning systems.

A new idea of multistage compound parallelogram flexure for the mechanical design of a novel parallel-kinematic XY micropositioning systems, which has a motion larger than 10 mm along with the compact structure. The concept of multistage compound parallelogram flexure is useful in designing a multiaxis micropositioning sysytems with both a compact sizr and a large workspace (Xu, 2012). It has been found that the pre- sented EMPC scheme is capable of improving the positioning performance in terms of settling time and steady-state error, as compared with conventional PID and MPC methods.

A Dual-Axis Long Traveling Nanopositioning stage (DALTNPS) is designed to extend the traveling and increase the accuracy, the two sorts of stages, a traditional ball-screw stage and a three degrees of freedom (3-DOF) piezostage. The measuring system which is composed of two laser interferometers and two plane mirrors is a 3-DOF optical measuring system (Liu et al., 2010).

A 2-degrees-of-freedom micro electromechanical systems (MEMS) nanopositioner with fully integrated electro thermal actuators and sensors. The stage displacement is effectively measured by varaiations in their resistance, which is dependent on the position of the stage (Rakotondrabe et al., 2014). A control scheme based on the

combination of feedforward and internal model control-feedback is contructed to enhace the general performance of MEMS device.
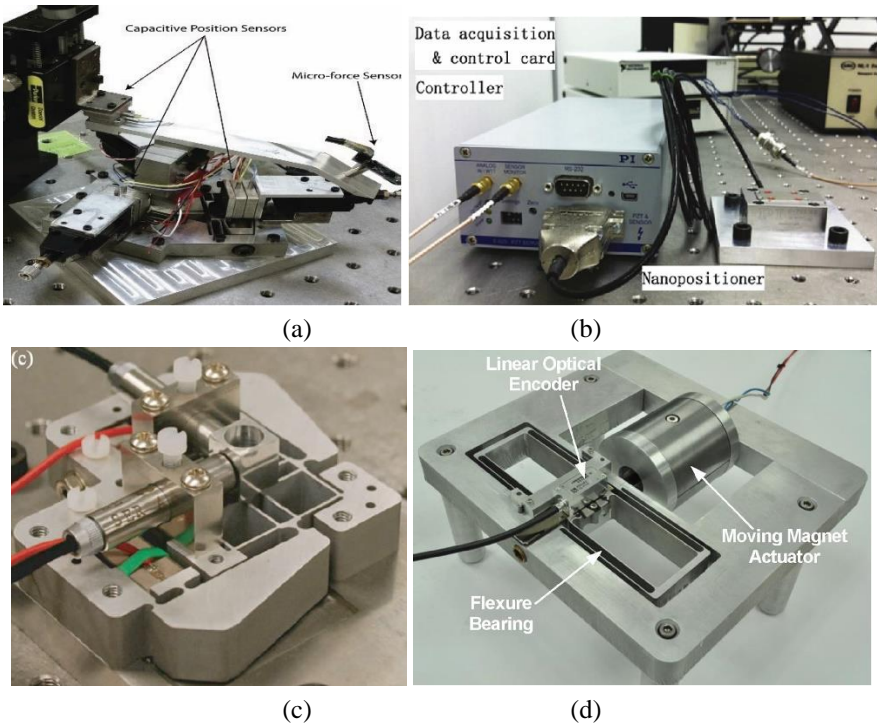
Figure 2. (a) 4 DOF nanopositioning systems (Pinskier et al., 2018) (b) nanopositioners (Fleming et al., 2016) (c) two-axis nanopositioner (Liu et al., 2015) (d) single-axis nanopositioner (Awtar & Parmar, 2010).

A six-DOF (degress of freedom) piezoelectric stage for positioning error compensation. The relationship between the displacement of the piezoelectric actuators and stage can be computed according to the geometric relationships of the actuators are installed. The combination of feedforwared and PI controller gives the stage positioning and tracking performance (Lee et al., 2014). The measurement signal is acquired and processed using an FPGA based processor for real time control. Some of the nanopositioners using piezoelectric actuators are

shown in Figure 2 used for various applications(Pinskier et al., 2018), (Fleming et al., 2016), (Liu et al., 2015), (Awtar & Parmar, 2010).
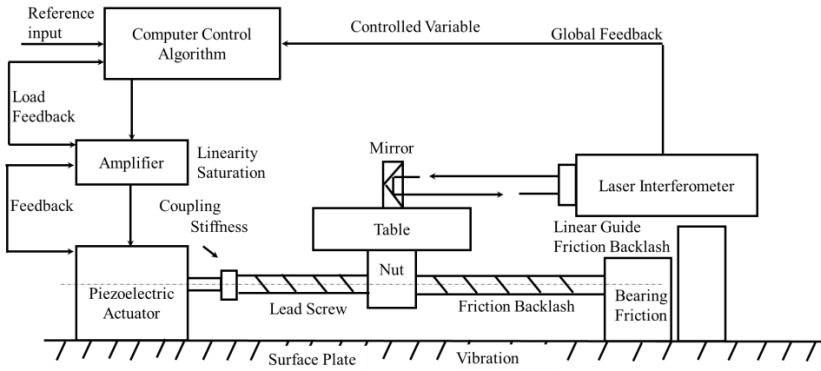
Figure 3. Typical locations of various non-linearities in nano positioning system.

The monolithic nanopositioner is constructed from a single sheet of piezoelectric material where a set of flexures are used for actuation and guidance, and another set are used for position sensing. A new class of monolithic nanopositioning design was recently reported where an XY nanopositioner was constructed from a single sheet of piezoelectric material. Active flexures were formed by removing parts of the sheet to provide both actuation and motion guidance. In addition, it is possible to use the flexures as sensors. These piezoelectric strain sensors have a wide sensing bandwidth, low noise at high frequencies and high sensitivity (Omidbeike et al., 2017). These are some of the nano positioners using piezoelectric actuators which give micro/nano motions for the applications of cell inserting, pipetting, targeting and cell investigation.

The developed control design utilizes the representation of the original plant through the MIMO-form, choosing model state variables for outputs instead of the measurable object position. This enables a MIMO plant simplification through the use of a decoupling network, resulting in two virtually independent plants, both of them described in SISO-form. After this simplification due the control measure like

hysteresis compensation for the nonlinearities of the plant separate designs of the DC drive and PEA controller can be performed. For the accurate estimation of the not measurable plant states, a second coordinate-transformation is involved. This is advantageous because of the very different operating range of the coarse and the fine actuator. In order to minimize trajectory-tracking errors, a state-space control concept with fast dynamic response due to a feedforward control by a novel trajectory generator for both actuators is designed (Dong et al., 2015).

The typical location of various non-linearities in nanopositioning control model is as shown in Figure 3. The linear, bearing friction, coupling, lead screw are the places non-linearities occurs in the closed loop systems. The author designed a novel X–Y parallel piezoelectric-actuator driven nanopositioner is studied from the perspectives of design optimization, dynamical modelling, as well as controller synthesis for high precision positioning and the positioning control model and dynamical modelling are provided to analyse the mechatronic structure of the proposed two-dimensional nano-stage, where the system model, including the hysteresis loop, is derived analytically and further verified experimentally. Real time experiments on the nano-stage platform demonstrate good robustness, high precision positioning and tracking performance, as well as recovery speed in the presence of saturation (Liu et al., 2015).

These are some of the nanopositioning systems used in various applications to achieve micro to nano motion with high positional accuracy, travel range and control of the system integration components and also the overall performance of the nano systems using piezoelectric actuators. These are all the various piezoelectric based nano/micro positioners were commericially available in the market as listed in Table 2 ranging between 5 to 125 mm in travel range, resolution in 0.02 to 40 nm and in terms of force in 10 to 300 N.

Table 2. Different types of positioners using piezoelectric actuators commercially available in the market

S. No.	Address	Positioners	Travel Range (mm)	Resolution (µm)	Force (N)
1	https://www.physikinstrumente.com/	Micropositioning stage	05 to 25	0.0069	10
		Miniature linear stage	13	0.12	10
		Miniature hexapods	40x40x13	40 nm	15
2	https://www.piezosystem.com/	3D Piezo nano positioner	9 to 13	0.02-0.07 nm	10
		Nano xy positioner	120 µm	0.24	65
3	http://www.xeryon.com/	Rotary piezo stages	full 360	6.25 micro radian	10
4	http://www.janssenprecisionengineering.com/	Miniature hexapods	10	50	300
		Nano positioning stage	10x10x4	0.05	50
		Linear piezo stage	51.5	1 nm	5
5	http://www.prior-us.com/	Piezo Z stage system	400 µm	1 nm	8
		Piezo XYZ stage system	8x8x6	0.05	20
6	http://www.nanopositioning.com/	Nanopositioner	6 µm	0.05	15
		Nanopositioning stage	500 µm	0.05	25
		XYZ piezo stage	100 µm	0.05	12
7	http://www.madcitylabs.com/	Z-axis nanopositioner	100 µm	0.2-0.4 nm	22
		XY axis nano positioner	50-75 µm	0.1-0.15 nm	32
		XYZ axis nanopositioner	100x100x100 µm	0.2-0.6 nm	27
8	https://www.aerotech.com/	Single axis nanopositioner	100-500 µm	0.30-0.9 nm	10

Issues in Control Systems of Nanopositioning

The performance of a nanopositioning system is specified in terms of its motion precision, accuracy, and resolution, along with speed of operation (Yang et al., 2018). In closed-loop operation, these specifications can be translated to equivalent control system design objectives, as follows:

1. Accuracy and precision depend on command tracking as well as low frequency noise and disturbance rejection.
2. Positioning noise and the minimum incremental motion determine the resolution. While positioning noise and disturbance rejection, and minimum incremental motion is determined by command tracking.
3. Closed-loop bandwidth determines the speed and response time of the nanopositioning systems and robustness against modelling uncertainties and parameter variations affect in all of the above.

Most of existing nanopositioning systems have a high first natural frequency because operate over relatively small motion range. Therefore, simple lower-order controllers with integrators provide good overall performance. In order to achieve a bandwidth greater than this first natural frequency, a higher order controller is needed, which poses greater performance trade-offs, particularly in terms of bandwidth and noise rejection (Devasia et al., 2007a). In general, lightly damped poles and zeros in a flexible system severely affect the closed loop stability and performance. In addition to this, the non-collocation of sensor and the actuator in our case leads to additional challenges in terms of bandwidth. The parameter variation due to coupled dynamics between the two axes and resulting variations in the frequency response along

each axis, poses further challenges in obtaining robust stability and performance (Leang et al., 2009).

Real time implementation often requires access to the fast digital signal processing software. For small tubes, with the first resonance frequency in the tens (or hundreds) of kilohertz, such implementations remain quite challenging. Analog control implementation could be an answer, although one would need to address a significant number of issues that naturally arise in such implementations (Moheimani, 2008). Control of distributed nanopositioning systems would require on-chip control schemes. Issues in such control include developing and implementing embedded, distributed, analog controllers (needed due to fast time scales); managing sensor/actuator failures; and maintaining robustness under substantial uncertainty prevalent in nano scale phenomena.

Various sources of noise and disturbance in the system limits the achievable resolution. This includes feedback sensor noise, actuator driver noise, electronic noise in the data acquisition hardware, and last but not the least, mechanical floor vibrations (Okyay et al., 2018). The individual contribution of these sources to the positioning noise will depend upon their respective magnitude, where they enter the system, the control architecture, and the controller design. When designing controllers for the vibrational dynamics of piezoelectric actuators, high-frequency vibrational modes are often neglected to obtain a simplified model (for controller design). However, the high-frequency vibrational modes can affect the stability of the closed-loop system as well as impose limitations on the achievable performance of the closed-loop system. Therefore, the spillover effects on these unmodeled modes should be considered in the controller design (Devasia et al., 2007b).

These are some of the control systems issues and solutions for controlling the overall nanopositioning systems using piezoelectric actuators. The challenge in the developing of control algorithm for the nano systems because of the positional accuracy less than 100 nm.

Iterative control can significantly increase the operational bandwidth of piezoelectric actuators without loss of positioning precision. For example, in Scanning Probe Microscopy (SPM) applications, iterative feedforward approaches can be used to position the probe precisely over a sample surface. Such iterative approaches are particularly useful for precise control of the tip-sample interactions such as the tip-sample force to avoid damage of soft biological samples during SPM imaging (Eghiaian et al., 2014). When imaging surfaces at the atomic scale with a scanning tunneling microscope (STM). One of the difficulties with feedback approaches in STM is that external sensors cannot directly measure the position of an STM-probe's atomically sharp tip. Instead, they measure the position of a different point on the STM scanner and then infer the position of the STM-probe's tip. Thus, it is challenging to directly measure the position of the STM-probe's tip over the sample surface with external sensors, also making feedback control challenging.

The performance of a nanopositioning system is affected by induced structural vibration (vibrational dynamics), hysteresis, and creep in the piezoactuator, cross coupling behaviours in both the actuator and mechanical system, external disturbances, and drift due to temperature variations (Altaher & Aphale, 2018). Cross-coupling effects can be handled using multi-input-multi-output controllers and iterative methods. External disturbances are often dealt with using passive or active vibration isolation systems. The effects of vibrational dynamics, hysteresis, and creep are discussed, as well as their impact on positioning performance.

For nano-motions, the thermal effects cannot be ignored. As mentioned, for coil-moving configurations, the heat generates via Joule heating in the coils and dissipates through radiation, convection and conduction. Among these, heat conduction to compliant guiding mechanisms predominates. The increased temperature will lead to thermal expansion effects, resulting in significant drift and positioning error (Parmar et al., 2014). In material selection and mechanical

arrangement are effective ways to minimize thermal expansion effects. Using the materials with small coefficient of thermal expansion (CTE) ensures less expansion with increased temperatures. Moreover, materials of high thermal conductivity should be selected in case that quick thermal equilibrium will be achieved.

CONCLUSION

In this study, the different types of piezoelectric actuators and nano positioners widely used in most of the nanosystems commercially available in the market are discussed. This paper reveals the challenges, control issues and their solutions for integrating the nanopositioning systems were illustrated. The measured output response of a piezo-based nanopositioners consists of combinational effects of vibration, hysteresis and creep. The oscillations are caused by vibrational dynamics, the slow upward drift of the output overtime is due to the creep effect and finally curved distortion in the output trajectory is due to hysteresis. To improve robustness, feedforward can be integrated with feedback control, as well to account for non-linearity such as hysteresis. Integrated feedback and feedforward control also eliminates the need for modelling and inverting the non-linear behaviours. The feedback controllers have been used to minimize the thermal drift occurs in piezoelectric actuators.

REFERENCES

Altaher, M., & Aphale, S. (2018). High-Precision Control of a Piezo-Driven Nanopositioner Using Fuzzy Logic Controllers. *Computers*, *7*(1), 10. https://doi.org/10.3390/computers7010010.

Amini, H., Farzaneh, B., Azimifar, F., & Sarhan, A. A. D. (2016). Sensor-less force-reflecting macro–micro telemanipulation systems by piezoelectric actuators. *ISA Transactions*, *64*, 293–302. https://doi.org/10.1016/j.isatra.2016.05.006.

Awtar, S., & Parmar, G. (2010). Physical and control system design challenges in large range nanopositioning. *IFAC Proceedings Volumes (IFAC-Papers Online)*, 152–159. https://doi.org/10.3182/20100913-3-US-2015.00129.

Cai, K., Tian, Y., Liu, X., Fatikow, S., Wang, F., Cui, L.,… Shirinzadeh, B. (2018). Modeling and controller design of a 6-DOF precision positioning system. *Mechanical Systems and Signal Processing*, *104*, 536–555. https://doi.org/10.1016/j.ymssp.2017.11.002.

Devasia, S., Eleftheriou, E., & Moheimani, S. O. R. (2007a). A survey of control issues in nanopositioning. *IEEE Transactions on Control Systems Technology*, *15*(5 SPEC. ISS.), 802–823. https://doi.org/10.1109/TCST.2007.903345.

Devasia, S., Eleftheriou, E., & Moheimani, S. O. R. (2007b). A Survey of Control Issues in Nanopositioning. *IEEE Transactions on Control Systems Technology*, *15*(5), 802–823.

Ding, B., Li, Y., Xiao, X., Tang, Y., & Li, B. (2017). Design and analysis of a 3-DOF planar micromanipulation stage with large rotational displacement for micromanipulation system. *Mechanical Sciences*, *8*(1), 117–126. https://doi.org/10.5194/ms-8-117-2017.

Dong, R., Tan, Y., & Xie, Y. (2015). Identification of micropositioning stage with piezoelectric actuators. *Mechanical Systems and Signal Processing*, *75*, 618–630. https://doi.org/10.1016/j.mechatronics.2011.11.007.

Dong, W., Chen, F., Li, H., Yang, M., & Du, Z. (2017). A two-dimensional nano-positioner: Design, modelling and experiments. *Robotics and Computer-Integrated Manufacturing*, *48*(April), 167–173. https://doi.org/10.1016/j.rcim.2017.03.003.

Dong, Y., Gao, F., & Yue, Y. (2016). Modeling and experimental study of a novel 3-RPR parallel micro-manipulator. *Robotics and Computer-Integrated Manufacturing*, *37*, 115–124. https://doi.org/10.1016/j.rcim.2015.07.006.

Eghiaian, F., Rico, F., Colom, A., Casuso, I., & Scheuring, S. (2014). High-speed atomic force microscopy: Imaging and force spectroscopy. *FEBS Letters*, *588*(19), 3631–3638. https://doi.org/10.1016/j.febslet.2014.06.028.

Fleming, A. J., Berriman, G., & Yong, Y. K. (2016). *Design, Modeling, and Characterization of an XY Nanopositioning Stage Constructed from a Single Sheet of Piezoelectric Material**, 1333–1338.

Gaurav Singh Naruka, N. J. and H. D. S. (2009). Automatic Control System Design ME 364. L Automatic Control System Design. *System*, *4*(February), 364–364.

Götze, H., & Pagel, L. (2007). Development of a micro-manipulator based on piezoelectric-technology. *Microelectronic Engineering*, *84*(5–8), 1333–1336. https://doi.org/10.1016/j.mee.2007.01.275.

Jain, R. K., Majumder, S., Ghosh, B., & Saha, S. (2014). Micro Manipulation by a Compliant Piezoelectric Micro Gripper towards Robotic Micro Assembly. *Conference Paper*, (Aimtdr), 1–7. https://doi.org/10.1504/IJMMS.2016.075402.

Jia, Q., Zhou, C., Deng, L., Du, Z., & Cao, Z. (2017). *Research on Nanoscale Displacement Online Modeling and Control of PCA,* (4152054), 1545–1550.

Kuang, Y., Hilgers, A., Sadiq, M., Cochran, S., Corner, G., & Huang, Z. (2016). Modelling and characterisation of an ultrasound-actuated needle for improved visibility in ultrasound-guided regional anaesthesia and tissue biopsy. *Ultrasonics*, *69*, 38–46. https://doi.org/10.1016/j.ultras.2016.02.018.

Laribi, M. A., Arsicault, M., Riviere, T., & Zeghloul, S. (2012). Toward new minimally invasive surgical robotic system. *2012 IEEE International Conference on Industrial Technology, ICIT 2012, Proceedings*, 504–509. https://doi.org/10.1109/ICIT.2012.6209988.

Leang, K., Zou, Q., & Devasia, S. (2009). Feedforward control of piezoactuators in atomic force microscope systems. *IEEE Control Systems Magazine*, *29*(1), 70–82. https://doi.org/10.1109/MCS.2008.930922.

Lee, H.-W., Hsieh, T.-T., Liu, C.-C., & Liu, C.-H. (2014). Development of a Flat Type Six-Axis Stage Based on Piezoelectric Actuators. *Mathematical Problems in Engineering*, *2014*. https://doi.org/10.1155/2014/523786.

Liu, C. H., Jywe, W. Y., Jeng, Y. R., Hsu, T. H., & Li, Y. tsung. (2010). Design and control of a long-traveling nano-positioning stage. *Precision Engineering*, *34*(3), 497–506. https://doi.org/10.1016/j.precisioneng.2010.01.003.

Liu, P., Yan, P., Zhang, Z., & Leng, T. (2015). Modeling and control of a novel X-Y parallel piezoelectric-actuator driven nanopositioner. *ISA Transactions*, *56*, 145–154. https://doi.org/10.1016/j.isatra.2014.10.005.

Lopez-Martinez, M. J., & Campo, E. M. (2011). Micro-Nano Technologies for Cell Manipulation and Subcellular Monitoring. *Biomedical Engineering-From Theory to Applications*. https://doi.org/10.5772/20038.

Maroufi, M., & Moheimani, S. O. R. (2016). A 2DOF SOI-MEMS Nanopositioner with Tilted Flexure Bulk Piezoresistive Displacement Sensors. *IEEE Sensors Journal*, *16*(7), 1908–1917. https://doi.org/10.1109/JSEN.2015.2504846.

Moheimani, S. O. R. (2008). Accurate and fast nanopositioning with piezoelectric tube scanners: Emerging trends and future challenges. *Review of Scientific Instruments*, *79*(7). https://doi.org/10.1063/1.2957649.

Okyay, A., Erkorkmaz, K., & Khamesee, M. B. (2018). Mechatronic design, actuator optimization, and control of a long stroke linear nano-positioner. *Precision Engineering*, (January), 0–1. https://doi.org/10.1016/j.precisioneng.2018.01.007.

Omidbeike, M., Teo, Y. R., Yong, Y. K., & Fleming, A. J. (2017). Tracking Control of a Monolithic Piezoelectric Nanopositioning Stage using an Integrated Sensor. *IFAC-PapersOnLine*, *50*(1), 10913–10917. https://doi.org/10.1016/j.ifacol.2017.08.2455.

Parmar, G., Barton, K., & Awtar, S. (2014). Large dynamic range nanopositioning using iterative learning control. *Precision Engineering*, *38*(1), 48–56. https://doi.org/10.1016/j.precisioneng.2013.07.003.

Pinskier, J., Shirinzadeh, B., Clark, L., & Qin, Y. (2018). Development of a 4-DOF haptic micromanipulator utilizing a hybrid parallel-serial flexure mechanism. *Mechatronics*, *50*(January), 55–68. https://doi.org/10.1016/j.mechatronics.2018.01.007.

Rakotondrabe, M., Fowler, A. G., & Moheimani, S. O. R. (2014). Control of a novel 2-DoF MEMS nanopositioner with electrothermal actuation and sensing. *IEEE Transactions on Control Systems Technology*, *22*(4), 1486–1497. https://doi.org/10.1109/TCST.2013.2284923.

Stevenson, D. J., Gunn-Moore, F. J., Campbell, P., & Dholakia, K. (2010). Single cell optical transfection. *Journal of the Royal Society, Interface/the Royal Society*, *7*(47), 863–71. https://doi.org/10.1098/rsif.2009.0463.

Wu, Z., & Xu, Q. (2018). Survey on Recent Designs of Compliant Micro-/Nano-Positioning Stages. *Actuators*, *7*(1), 5. https://doi.org/10.3390/act7010005.

Xie, Y., Zeng, F., Xi, W., Zhou, Y., Liu, H., & Chen, M. (2016). A Robot-Assisted Cell Manipulation System with an Adaptive Visual Servoing Method. *Micromachines*, *7*(6), 104. https://doi.org/10.3390/mi7060104.

Xu, Q. (2012). New flexure parallel-kinematic micropositioning system with large workspace. *IEEE Transactions on Robotics*, *28*(2), 478–491. https://doi.org/10.1109/TRO.2011.2173853.

Yang, Y., Wei, Y., Lou, J., Fu, L., Fang, S., & Chen, T. (2018). Dynamic modeling and adaptive vibration suppression of a high-speed macro-micro manipulator. *Journal of Sound and Vibration*, *422*, 318–342. https://doi.org/10.1016/j.jsv.2018.02.034.

Chapter 2

SYNTHESIS AND CHARACTERIZATIONS OF SUSTAINABLE TI/SNO$_2$-SB$_2$O$_3$/PBO$_2$ ELECTRODE USING SOL-GEL ELECTROCHEMICAL COMBINED COATING AND APPLICATION TO ELECTROCHEMICAL DEGRADATION OF METHYL ORANGE

K. Kannan[1,], S. Praveen Kumar[1], T. K. Srinivasan[1],
G. Muthuraman[2] and I. S. Moon[2]*

[1]Micro Electro-Mechanical System (MEMS) Laboratory,
Saveetha Engineering College, Chennai, India
[2]Department of Chemical Engineering,
Sunchon National University, Suncheon, Republic of Korea

---

[*] Corresponding Author's Email: kannank@saveetha.ac.in.

ABSTRACT

Developing the sustainable electrode materials leads to widen the applications in the various platforms such as biosensors, battery and pollutant treatment process. But the preparation of active material is a crucial process and which enable to overcome the hard electrochemical and mechanical conditions. Here we discuss the synthesis of SnO_2-Sb_2O_3 oxides doped nano-PbO_2 electrode by sol-gel combined with electrochemical multicoated method from non-aqueous electrolyte solution. The results show that as synthesized nano-PbO_2 electrode was highly stable for 530 hours at 500 mA/cm^2 and harden than traditional PbO_2 electrode prepared from aqueous electrolyte. Crystalline, surface morphology and electrochemical characterizations were performed by XRD, SEM and cyclic voltammogram techniques respectively and results observed that prepared Ti/SnO_2-Sb_2O_3/PbO_2 electrode showed highly crystalline, star like morphology with high charging current and good electro-catalytic activity. Hence the synthesized electrode utilized as an anode for electrochemical degradation of Methyl orange (MO) as a model dye pollutant. The electrolysis results reveal that, complete de-colorization of MO was observed at short period of electrolysis at Ti/SnO_2-Sb_2O_3/PbO_2 electrode and the COD removal efficiency reached 82% which was 21% higher than rest of the other electrodes.

Keywords: nano-PbO_2 electrode, sol-gel, electrochemical deposition, dye degradation

INTRODUCTION

The PbO_2 (PbO_2) is a well-known semi conductive material. However, it was used an efficient conductive material in various fields such as lead acid battery (Zerroual et al., 1993; Yamashita & Matsumaru et al., 1988), super capacitor (Ni et al., 2013; Dan et al., 2015), electrochemical pollutant treatment (Riyanto & Wulandari, 2017; Feng et al., 2016; Ghanbari et al., 2016), dye degradation (Elaissaoui et al., 2016; Zhou et al., 2005), production of ozone (Rufino et al., 2010), active oxidants, and soon. Researches were on course for the development of PbO_2 electrodes for useful applications (Karami &

Alipour, 2009). PbO_2 is generally unstable in hard conditions and degrades to harmful $Pb^{(0)}$ and Pb^{2+} (Lin et al., 2010; Zhang et al., 2017). Efficient way to increase the stability is decreasing the size of the material to nanoscale level by adding dopants. The nano PbO_2 was prepared by wet chemical and electrochemical method. Among them electrochemical synthesis is efficient as various parameters such as current density, electrode area/volume ratio, concentration of the electrolyte, and temperature can be controlled (Amadelli et al., 1999). Over the past fifteen decades, researches were trying to increase the stability of PbO_2. For instance the transition metal ions like Cu^{2+} (Hung et al., 2015), Ag^+ (Ge & Johnson, 1995), Fe^{2+} (Velichenko et al., 1998), Bi^{2+} (Sobrinho et al., 2015), Ce^{3+} (Duan et al., 2014), Ni^{2+} (Xia & Dai, 2015) were added in presence of Pb^{2+} electrolyte. Some researchers, promoting the surface morphology by the addition of metal oxides like CO_3O_4 (Dan et al., 2011), Mn_3O_4 (Zhang et al., 1994) to the PbO_2 medium and reported that the oxygen evolution potential has been shifted to more positive value and mutual enhancement in the electro-catalytic activity and stability.

Hong et al. (2011) reported that addition of polymers like PTFE, as a composite material to increase the stability towards 1000 hrs and promoted the O_2 evolution potential. Similarly Li et al. (2016) used PVA (Polyvinyl alcohol) into PbO_2 to increase the electrochemical activity and stability. Many research team has found the relationship between morphological orientation of material and their sustainability. The addition of a surfactant like cationic, anionic and non-ionic was reported to be used as a morphological controlling agent as well as a stabilizer of nano particles (Ghaemi et al., 2006; Cao et al., 2003). The major problem with the PbO_2 synthesis is the growth of $Pb^{(0)}$ dendrites on the cathode surface during deposition, which has been controlled by the addition of additive to the electrolyte system (Sun et al., 2013). Generally, the pH of the electrolyte determines the orientation of PbO_2. α and β-PbO_2 (Perry & Wilkinson 2007). Instead of aqueous electrolytes, recently non-aqueous and RTIL (room temperature ionic

liquids) is being used as an electrolyte for the synthesis of nano-PbO_2 electrode and application to degradation of bacteria and phenol (Yu et al., 2016; Ju et al., 2012). Significantly, nano PbO_2 are widely prepared from methane sulfonic acid (MSA) in the presence of lead methylsulfonateas precursors (Perret et al., 2011). Few researchers used CH_3CN as an electrolyte in presence of TBAP and 6M water as supporting electrolytes. The result implies that, synthesized nano-PbO_2 is more adhere than conventional aqueous method (Abaci et al., 2003).

Here, we discuss about the synthesis of nano-PbO_2 electrode by sol-gel coating followed by electrochemical multi-step deposition method. SnO_2-Sb_2O_3 were prepared initially to act as an inner layer over nano-PbO_2 electrode. The morphology of as synthesized nano-PbO_2 was characterized by XRD and SEM respectively. Electrochemical characterization studies was carried on redox behavior, sustainability of the electrode and electro catalytic activity towards oxidation of methyl orange as model pollutant.

MATERIALS AND METHODS

The nano-PbO_2 electrode was prepared from the following chemicals: Lead perchlorate ($Pb(ClO_4)_2.6H_2O$, 99%), Tin tetrachloride, ($SnCl_4$, 99%), Antimony trichloride ($SbCl_3$, 99%) are purchased from the Sigma Aldrich, South Korea. Lead nitrate ($PbNO_3)_2$, 99%) Duksan Pure Chemicals, South Korea. Acetonitrile (CH_3CN, 99%) from Daejung Chemical Metal, South Korea.

EXPERIMENTAL METHODS
PRETREATMENT OF TITANIUM ELECTRODE

The Ti mesh electrode working area of $4cm^2$ (2X2) was taken and the pretreatment process has been performed before electrode synthesis. At first, surface TiO_2 layer was removed by cleaning with SiC (100) paper followed by washing with DI water. The cleaned electrode was first boiled with 5M NaOH solution and then Oxalic acid solution boil the solution till turned into blackish brown which indicates the removal of all oxides from the surface of Ti electrode. Finally, the electrode washed with DI water, ethanol and dry at room temperature.

SYNTHESIS OF TI/SNO₂-SB₂O₃ ELECTRODE

The inner layers of SnO_2-Sb_2O_3 were prepared by two different methods: a) cathodic electrochemical and dip coating methods and the electrodes preparation as follows. The schematic diagram for the preparation of multilayered PbO_2 is given in the Figure 1. Though the stepwise synthesis method as given here.

ELECTRODE POSITION

Cathodic electrode position of SnO_2 and Sb_2O_3 were performed in the electrochemical systems which contained 17.5g $SnCl_4$, 0.73 g Sb_2O_3 and 2 mL conc. HCl mixed together in 100mL ethanol; the current density (j) of 20 mA/cm^2 passed into the electrolyte system which connected into Ti and Pt electrode represented as cathode and anode respectively. Finally, the metal deposited Ti electrode put into muffle furnace for 1 hr (Li et al., 2005).
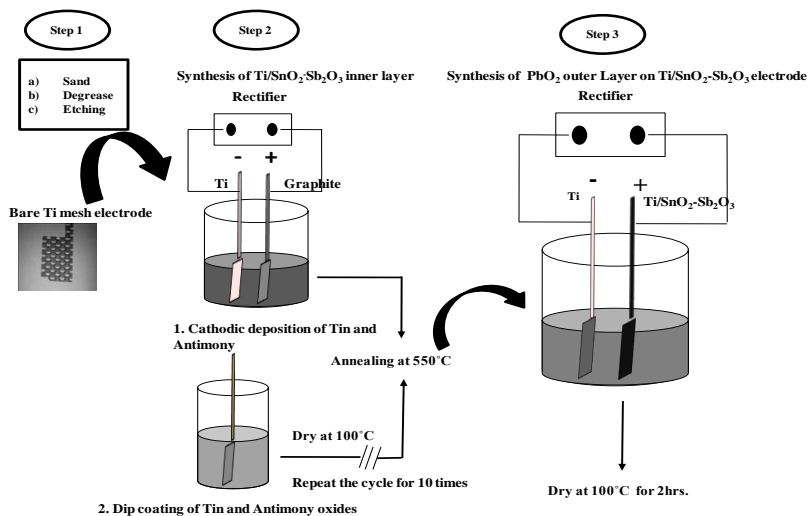
Figure 1. Schematic representation of Synthesis of inner layer SnO_2-Sb_2O_3 and Outer layer nano PbO_2.

DIP COATING

The electrodeposited electrode was taken as a base electrode for the preparation of secondary layer SnO_2-Sb_2O_3 electrode and the dip coating solution can be prepared as following: The homogeneous solution contained 30 g $SnCl_4$, 0.8 g Sb_2O_3 and 2.5 mL conc. HCl were mixed together and then the base electrode kept for 5 min and dry at 100°C. Finally, the electrodes under annealing at 550°C for 1 hr. repeat this process for 10 times and at last electrodes kept at 550°C for 2 hrs (Li et al., 2005).

SYNTHESIS OF TI/SNO₂-SB₂O₃/PBO₂ ELECTRODE

The primary PbO_2 layer electrochemically deposited on the Ti/SnO_2-Sb_3O_5 electrode where the electrochemical cell consisted of Ti/SnO_2-Sb_2O_3 and Ti electrodes represented as anode and cathode

respectively which dip into the non-aqueous electrolyte mixture consists of 0.1 M $Pb(ClO_4)_2$, 0.1M TBAP and 6M H_2O in Acetonitrile solvent. To deposition of PbO_2 current density of 100 mA/cm^2 was passed into the electrodes through rectifier for 15 mins. Finally, the PbO_2 deposited electrode kept for dry at 100°C for 2 hrs (Abaci et al., 2003). Which is designated as Ti/SnO_2-Sb_2O_3/PbO_2 (non-aqu). The same procedure has been followed to prepare the single layered PbO_2 electrode without incorporation SnO_2-Sb_2O_3 layer and denoted as Ti/PbO_2 (non-aqu). Finally, traditional PbO_2 electrode has been synthesized from HNO_3 medium which as reported earlier and denoted as Ti/PbO_2 (aqu) (Lee et al., 2000).

CHARACTERIZATIONS

The morphologies of the mixed oxides were examined by HRTEM using a JEOL JEM-2000EX2 microscope operated at 200 kV, particle sizes were determined by SEM (Zeiss EVO-MA10), and crystal structures were by XRD using an X'PERT-PRO X-ray diffractometer and Al Ka radiation (l = 1.540598 [A]). The UV–Vis spectrum of the methyl orange at various time intervals was carried out by using a Scinco s-3100 spectrophotometer. The electrochemical measurements were performed in electrolyte of 0.1 Na_2SO_4 solutions by using PARSTAT 3 (AMETEK Instruments, USA) electrochemical workstation. As synthesized Ti/PbO_2 (aqu), Ti/PbO_2 (non-aqu) and Ti/SnO_2-Sb_2O_3/PbO_2 (non-aqu) (electrodes were used as working electrode, Pt mesh was taken as Counter and Ag/AgCl (in saturated with KCl) as reference electrode. The voltammogram was run in the electrolyte of 0.1 M H_2SO_4 solution in potential limit between 0.0-2.0 V at scan rate of 50 mV/s.

The accelerated life time test was conducted by electrochemical cell, where fabricated PbO_2 electrodes were used an anode and Ti electrode was used as a cathode. The electrolyte solution was 3M

H_2SO_4 and the cell temperature was maintained to 60°C, a constant current density 500 mA/cm^2 was supplied by DC rectifier.

The electro-catalytic oxidation of methyl orange was performed by galvano static electrolysis process. The electrochemical cell consists of 30mg/L MO into the 0.1 M Na_2SO_4 as electrolyte. The fabricated PbO_2 electrodes and unfabricated PbO_2 electrodes were used as an anodes and graphite electrode (20 mm × 10 mm × 10 mm) was placed as cathode with the distance of 2cm. The constant current density of 10 to 50 mA/cm^2 was passed into the electrolyte solution at 40°C for 80 min. The samples were collected at each 10 min intervals for monitoring the concentration of MO by UV-Vis spectrophotometer. The chemical oxygen demand(COD) content of MO before and after degradation was detected through dichromate titrimetric standard method, the COD content before degradation was marked COD_0, the COD content after degradation was marked COD_t, the calculated formula was

$$\eta = \frac{COD_0 - COD_t}{COD_0} \ X100\%$$

(1)

RESULTS AND DISCUSSIONS
MORPHOLOGICAL CHARACTERIZATIONS

The crystal structure of synthesized PbO_2 electrodes were characterized by X-Ray diffraction technique and the results are depicted in the Figure 2. The results emphasize that, peaks position and intensities are nicely correlated with the reference PbO_2 electrodes and there is no difference was found on the related peak position which corresponds to 2θ angle at 25.64, 28.71, 36.53, 49.37 and 52.48 are attributed to (110), (101), (200), (211), (220) phases respectively (Lee et al., 2000). Sharpen the peak intensity was observed for Ti/PbO$_{2(aqu)}$, Ti/PbO$_{2(non-aqu)}$ and Ti/SnO$_2$-Sb$_2$O$_3$/PbO$_{2(non-aqu)}$electrode which means

highly crystalline morphology of PbO_2 was deposited on the surfaces and no peak for SnO_2-Sb_2O_3 was observed that indication of complete and evenly deposition of PbO_2 on the inner layer which confirmed in SEM analysis.
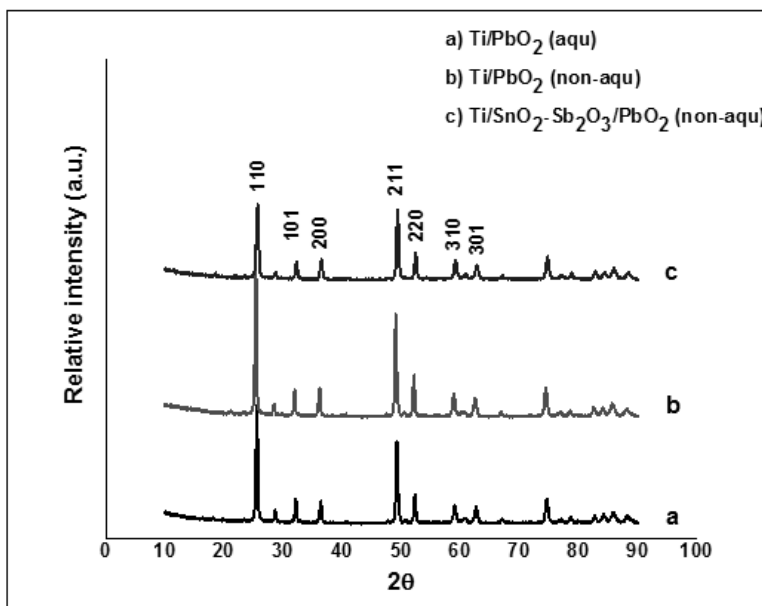
Figure 2. XRD image for a) Ti/PbO$_2$ (aqu) (b) Ti/PbO$_2$ (non-aqu) and (c) Ti/SnO$_2$-Sb$_2$O$_3$/PbO$_2$ (non-aqu) electrodes.

The surface morphological analyses for Ti/SnO$_2$-Sb$_2$O$_3$ electrodes were obtained from SEM techniques and electrodes were synthesized from electrochemical and dip coated method are depicted in Figure 3 (a) and (b) respectively. In Figure 3(a), the electrochemically prepared SnO$_2$-Sb$_2$O$_3$ oxide electrode show layered and the lateral arrangement of oxides. The small pin holes were spread over the surface indicate the evolution of H$_2$ during cathodic electrochemical
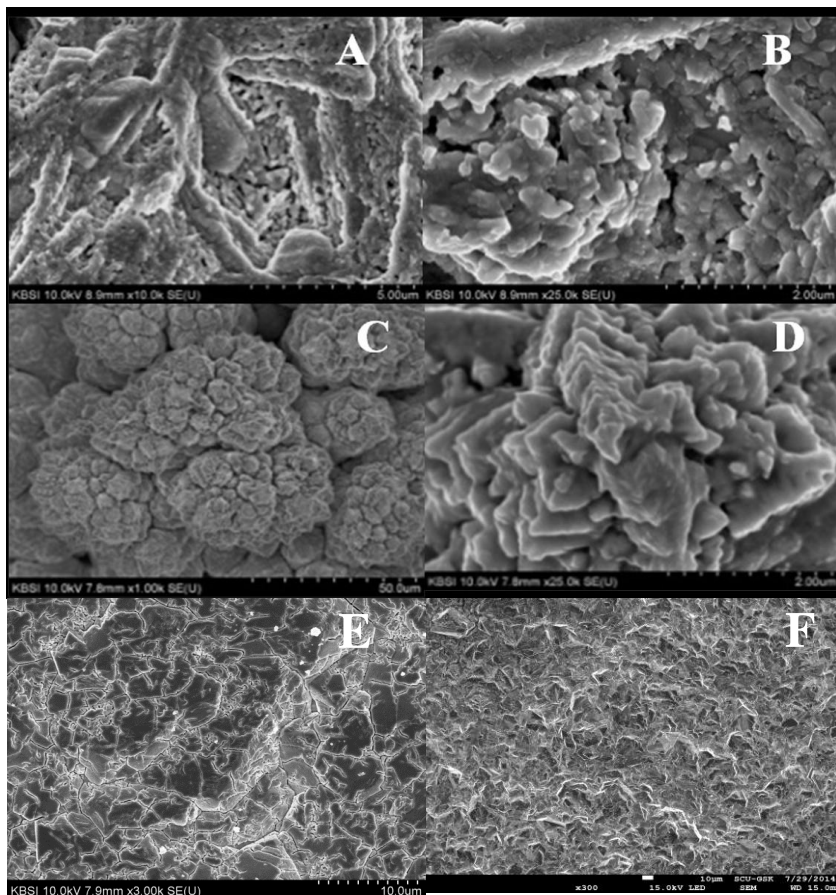
Figure 3. SEM images for the (A) Ti/SnO$_2$-Sb$_2$O$_3$ electrodes synthesized by electrochemical method and (B) Ti/SnO$_2$-Sb$_2$O$_3$ electrodes synthesized Dip coating method. (C) SEM image for PbO$_2$ layer on Ti/SnO$_2$-Sb$_2$O$_3$ electrodes at low magnification and (D) the same electrode at high magnification. (E) SEM image for Ti/PbO$_2$ electrode synthesized from aqueous electrolyte and (F) SEM image for Ti/PbO$_2$ electrode synthesized from non-aqueous electrolyte.

deposition. The evolution of hydrogen suppressing the nucleation of the metal results in enhancing agglomeration particles on the Ti-surface. Similarly, the SEM image for dip coated SnO$_2$-Sb$_2$O$_3$ electrode depicted in Figure 3 (b) and the oxides are arranged as similar as fish skin "placoid" scaling. Figure 3 (c) and (d) depict the SEM image of PbO$_2$ at

low and high magnified scale. At low magnification (Figure 3 (c)) clearly showed cauliflower like morphology of PbO_2 deposited over the SnO_2-Sb_2O_3 oxide inner layer. But while looking into high magnification it is very clearly seen that the formation of star like arrangement of PbO_2 oxide having the size of about 50 nm. Figure 3 (e) and 3 (f) depict the SEM image for Ti/PbO$_2$ (aqu) and Ti/PbO$_2$ (non-aqu) electrodes. For aqueous PbO_2 electrode showed non-even surfaces with many cracks and lines where as non-aqueous PbO_2 electrodes free from those obstacles.
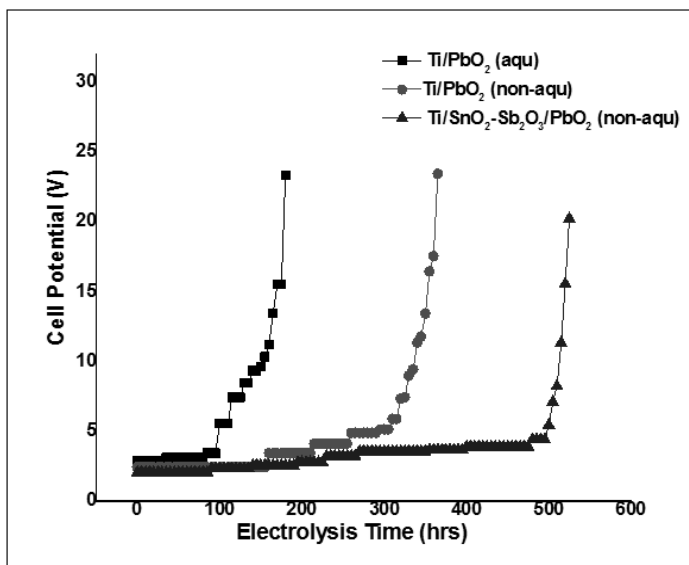
Figure 4. Electrode stability test for Ti/PbO$_{2(aqu)}$, Ti/PbO$_2$ (non-aqu) and Ti/SnO$_2$-Sb$_2$O$_3$/PbO$_{2(non-aqu)}$ electrodes in 3M H$_2$SO$_4$ at current density of 500 mA/cm^2.

Figure 4 depicts the comparative sustainability study for Ti/PbO$_2$ (aqu), Ti/PbO$_2$ (non-aqu) and Ti/SnO$_2$-Sb$_2$O$_3$/PbO$_2$ (non-aqu) electrodes in 3M H$_2$SO$_4$ at current density of 500mA/cm^2. All the synthesized electrodes are designated as anode and Ti as cathode. The results showed that the PbO_2 electrode synthesized from aqueous medium showed stability only up to 180 hrs and the single layered PbO_2 electrode synthesized

from non-aqueous medium showed stability up to 365 hrs which has been increased 2 folds than Ti/PbO$_{2(aqu)}$ electrode. But, SnO$_2$ and Sb$_2$O$_3$ doped PbO$_2$ electrode synthesized from non-aqueous medium showed maximum stability up to 530 hrs which was 1.4 times higher than Ti/PbO$_{2(non-aqu)}$ and 2.9 times higher than Ti/PbO$_{2(aqu)}$. It was proved that multi-coated PbO$_2$ synthesized from non-aqueous system enhances the stability and can be taken as an anode for further electrochemical applications.

ELECTROCHEMICAL CHARACTERIZATIONS OF PbO$_2$ ELECTRODES

As mentioned, SEM and XRD results showed fabricated Ti/SnO$_2$-Sb$_2$O$_3$/PbO$_2$ electrode has crystalline and more compact arrangement of PbO$_2$ particles at terminal layer. The results were correlated with the electrochemical redox studies and evaluated for all electrodes in 0.1 M Na$_2$SO$_4$ solution as electrolyte at the scan rate of 50 mV/s. The Figure 5 clearly indicated that, the position of Pb^{2+} to Pb^{4+} oxidation peak current (I$_A$) is varied for each electrode, for instance peak potential showed at 1250 mV, 1580 mV and 1830 mV for Ti/PbO$_{2(aqu)}$, Ti/PbO$_{2(non-aqu)}$ and Ti/SnO$_2$-Sb$_2$O$_3$/PbO$_{2(non-aqu)}$ electrodes respectively. Meanwhile anodic peak potential shifted more positive (ca. 570 mV) electrode which attributed to increases in the oxygen evolution potential of the electrode in order doped with SnO$_2$-Sb$_2$O$_3$ as inner layer (Li et al., 2005). Additionally, anodic peak current for multicoated electrode showed 2 folded higher than aqueous and non-aqueous PbO$_2$ electrode. The similar behaviour is being noticed in the reserves scan at which the Pb^{4+} to Pb^{2+} reduced peak appeared almost at 1230 mV, but the huge charging current has been observed for the Ti/SnO$_2$-Sb$_2$O$_3$/PbO$_{2(non-aqu)}$ electrode which is 10.82 times higher than rest of the PbO$_2$ compositions. The results indicate multicoated PbO$_2$ electrode

resemblance high crystalline and surface morphology which correlated with the results obtained from SEM and XRD analysis.

ELECTROCHEMICAL OXIDATION FOR MO

As mentioned, $Ti/SnO_2-Sb_2O_3/PbO_{2(non-aqu)}$ electrode showed better electrochemical performance and sustainability than the rest of the electrodes. In order to understand electro-catalytic activity of PbO_2 electrodes, MO was taken as model dye pollutant and electrochemical set up has denoted earlier. Figure 6 displays the effect of electrodes on the removal efficiency of MO from the 0.1M Na_2SO_4 electrolyte at the current density of 30 mA/cm^2 at 40°C. According to result, electrolysis duration to maximum MO removal efficiency was displayed to $Ti/PbO_{2(aqu)}$ and $Ti/PbO_{2\ (non-aqu)}$ electrodes as 200 min and 140 min respectively. But $Ti/SnO_2-Sb_2O_3/PbO_{2(non-aqu)}$ electrode attained maximum MO decolonization at short period of electrolysis time i.e., 80 min. The highest and quick removal efficiency attributed to the formation of OH • on the electrode surface and stimulated maximum efficiency (Hong et al., 2011; Yu et al., 2016; Ju et al., 2012) as one more clearly evidence that, multicoated PbO_2 electrode showed better electro-catalytic activity and which can be used for further analysis.

It is concluded that, $Ti/SnO_2-Sb_2O_3/PbO_{2(non-aqu)}$ electrode showed highest removal efficiency than the rest of electrodes, but the current density, which used for the electrolysis played an important role whereas electrolysis of MO has been studied at various current densities such that 10 mA/cm^2 to 50 mA/cm^2 at the optimum temperature of the bath fixed to 40°C. Figure 7 depicts the effect of current density on the removal efficiency of the MO at 0.1 M Na_2SO_4 solution.

The results show increases in the current density facilitated to increase in the removal efficiency MO, however RE displayed as
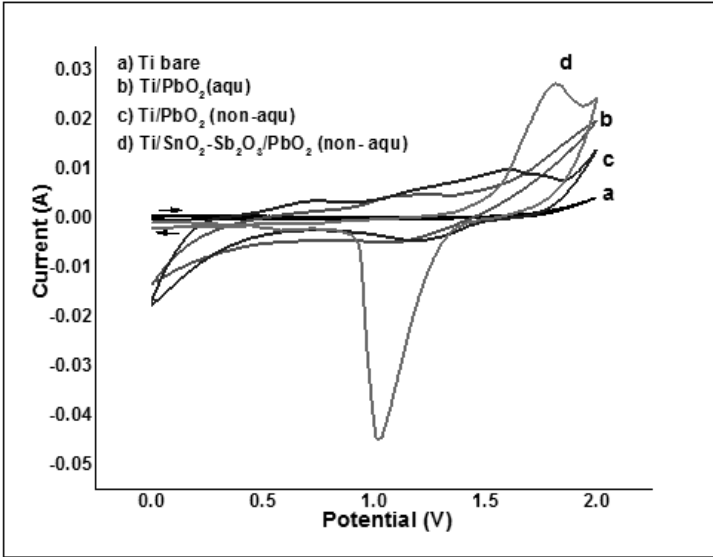
Figure 5. Cyclic voltammogram performances for $Ti/PbO_{2(aqu)}$, $Ti/PbO_{2\ (non-aqu)}$ and $Ti/SnO_2-Sb_2O_3/PbO_{2\ (non-aqu)}$ electrodes in 0.1M Na_2SO_4 at scan rate of 50 mV/s.
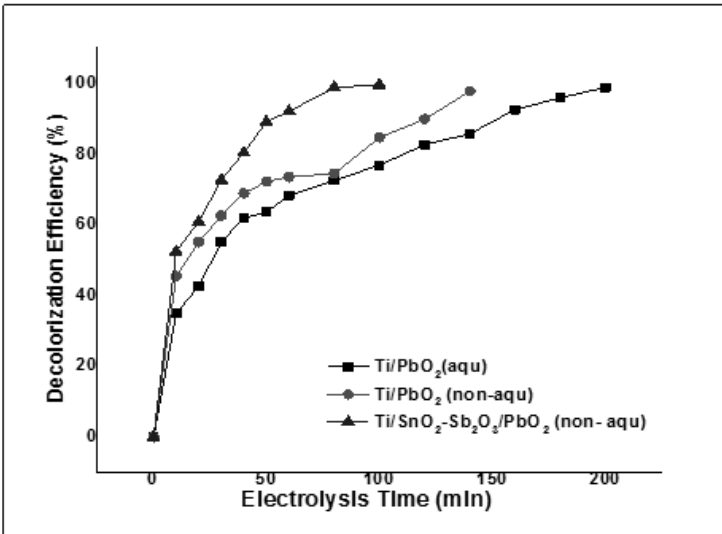
Figure 6. Effect of electrodes on the electrolysis of 30 mg/L of MO in 0.1 M Na_2SO_4 at current density of 30 mA/cm^2, pH the electrolyte of 3 at 45°C.
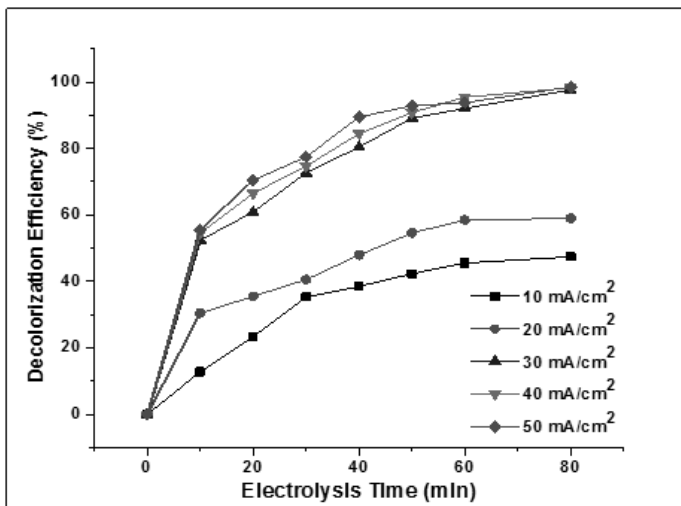
Figure 7. Effect of current density on the electrolysis of 30 mg/L of MO in 0.1 M Na$_2$SO$_4$. pH electrolyte of 3 at 45°C. The current density varied from 10 mA/cm^2 to 50 mA/cm^2.

28.58%, 58.99% and 96.58%, which corresponds to current density of 10 mA/cm^2, 20 mA/cm^2 and 30 mA/cm^2 respectively. But while further increasing the current density beyond 30 mA/cm^2 did not observe sufficient changes in the MO removal efficiency. It is worthy to note that the low current density affordable for industrial process and opening the pave to lower energy consumption mode.

Figure 8 displays the comparative study of COD removal efficiency by the three different PbO$_2$ electrodes and the electrolysis was carried out at optimum electrochemical condition such as current density of 30 mA/cm^2, temperature of 40°C in 0.1 M Na$_2$SO$_4$ solution. As for the results, the COD removal efficiency increases with increases in the electrolysis time but the maximum removal efficiency was attained by the Ti/SnO$_2$-Sb$_2$O$_3$/PbO$_{2(non-aqu)}$ electrode i.e., 82% which has been reached at 80 min of electrolysis and remaining Ti/PbO$_{2(non-aqu)}$ and Ti/PbO$_{2(aqu)}$ electrodes showed only 61% and 52% of COD removal efficiency respectively. The obtained COD removal efficiency by Ti/SnO$_2$-Sb$_2$O$_3$/PbO$_2$ $_{(non-aqu)}$ electrode is 21% higher than

Ti/PbO$_{2(non-aqu)}$ and 30% higher than Ti/PbO$_2$ $_{(aqu)}$ electrodes. The highest efficiency was achieved by the existence of O$_2$ evolution over potential of multicoated non-aqueous PbO$_2$ electrode.
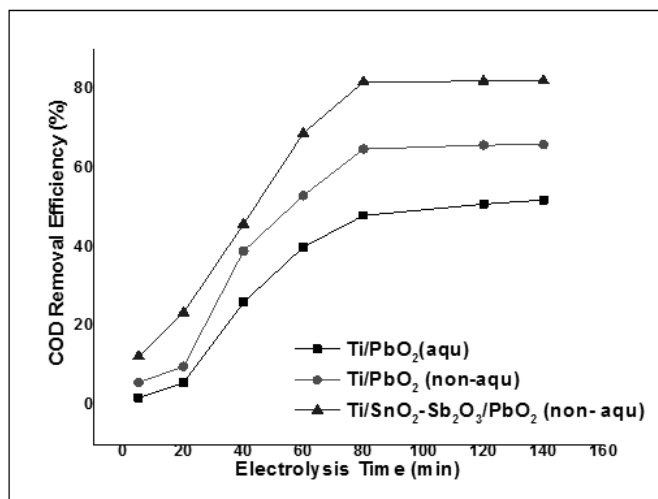
Figure 8. Comparative study for the COD removal efficiency by the Ti/PbO$_{2(aqu)}$, Ti/PbO$_2$ $_{(non-aqu)}$ and Ti/SnO$_2$-Sb$_2$O$_3$/PbO$_2$ $_{(non-aqu)}$ electrodes in presence of 30 mg/L of MO in 0.1 M Na$_2$SO$_4$ at current density of 30 mA/cm^2, pH the electrolyte of 3 at 45°C.

CONCLUSION

The PbO$_2$ electrodes were electrochemically prepared from the non-aqueous electrolyte such as acetonitrile and 6M H$_2$O at optimum current density. Prior to PbO$_2$ deposition, the Ti electrode was covered by inner layer of SnO$_2$-Sb$_2$O$_3$ by both electrochemical and dip-coating method. The SEM image showed the different morphological orientation of inner SnO$_2$-Sb$_2$O$_3$ surface and star like arrangement of outer layer PbO$_2$. The electrochemical stability test revealed that as Ti/SnO$_2$-Sb$_2$O$_3$/PbO$_{2(non-aqu)}$ electrode showed highest stability about 530hrs which was 1.45 times higher than Ti/PbO$_2$ $_{(non-aqu)}$ electrode. The cyclic voltammogram results concluded that, Ti/SnO$_2$-Sb$_2$O$_3$/

$PbO_{2(non-aqu)}$ electrode showed define redox peaks for PbO_2 with highest charging current and proven to show better electro-catalytic activity at short period of time than rest of the electrodes. For electrolysis of MO was studied under different current densities in 0.1M Na_2SO_4 at optimum pH of 3. Whereas 30 mA/cm^2 has showed maximum MO removal efficiency and no more sufficient changes were observed beyond this limit. The COD analysis revealed that, Ti/SnO_2-$Sb_2O_3/PbO_{2(non-aqu)}$ electrode showed 21% higher COD removal efficiency than $Ti/PbO_{2(non-aqu)}$ electrode and 30% higher than $Ti/PbO_{2(aqu)}$ electrode. The overall results concluded that the multicoated Ti/SnO_2-$Sb_2O_3/PbO_{2(non-aqu)}$ electrode is suitable anode material for the MO dye degradation and which can be enhances to pilot scale for the future purpose with enlarge size and optimum condition. The future direction of the work is expected to improvise the application of PbO_2 in sensor, red-ox flow battery, and supercapacitor applications. The limitation of this process is dissolution and of lead in to the electrolyte which could be controlled by deposition method optimized condition.

REFERENCES

Abaci, S., Pekmez, K., Pekmez, N. & Yildiz, A. (2003). Electrocatalysis of polyaniline formation by PbO2 in acetonitrile. *Journal of Applied Polymer Science*, *87*(4), 599-605.

Amadelli, R., Armelao, L., Velichenko, A. B., Nikolenko, N. V., Girenko, D. V., Kovalyov, S. V. & Danilov, F. I. (1999). Oxygen and ozone evolution at fluoride modified lead dioxide electrodes. *Electrochimica Acta*, *45*(4-5), 713-720.

Cao, M., Hu, C., Peng, G., Qi, Y. & Wang, E. (2003). Selected-control synthesis of PbO2 and Pb3O4 single-crystalline nanorods. *Journal of the American Chemical Society*, *125*(17), 4982-4983.

Dan, Y., Lin, H., Chen, L., Zhang, L., Su, J., Yue, H. & Cai, X. (2015). A composite electrodeposited PbO_2/SnO_2 positive electrode material for hybrid supercapacitors. *RSC Advances*, *5*(120), 98983-98989.

Dan, Y., Lu, H., Liu, X., Lin, H. & Zhao, J. (2011). Ti/PbO_2+ nano-Co_3O_4 composite electrode material for electrocatalysis of O_2 evolution in alkaline solution. *International Journal of Hydrogen Energy*, *36*(3), 1949-1954.

de Figueredo, F. D. A. A., de Souza Lucas, F. W., Fill, T. P., Rodrigues-Filho, E., Mascaro, L. H., da Silva Casciano, P. N., ... & Correia, A. N. (2015). Insights into electrodegradation mechanism of tebuconazole pesticide on Bi-doped PbO_2 electrodes. *Electrochimica Acta*, *154*, 278-286.

Duan, X., Zhao, Y., Liu, W., Chang, L. & Li, X. (2014). Electrochemical degradation of p-nitrophenol on carbon nanotube and Ce-modified-PbO_2 electrode. *Journal of the Taiwan Institute of Chemical Engineers*, *45*(6), 2975-2985.

Elaissaoui, I., Akrout, H. & Bousselmi, L. (2016). *J. Desal. Wat. Treat.*, *57*, 1-14.

Feng, Y., Yang, L., Liu, J. & Logan, B. E. (2016). Electrochemical technologies for wastewater treatment and resource reclamation. *Environmental Science: Water Research & Technology*, *2*(5), 800-831.

Ge, J. & Johnson, D. C. (1995). Electrocatalysis of Anodic Oxygen-Transfer Reactions: Aliphatic Amines at Mixed Silver-Lead Oxide-

Film Electrodes. *Journal of the Electrochemical Society*, *142*(5), 1525-1531.

Ghaemi, M., Ghafouri, E. & Neshati, J. (2006). Influence of the nonionic surfactant Triton X-100 on electrocrystallization and electrochemical performance of lead dioxide electrode. *Journal of Power Sources*, *157*(1), 550-562.

Ghanbari, F., Moradi, M., Mehdipour, F. & Gohari, F. (2016). Simultaneous application of copper and PbO_2 anodes for electrochemical treatment of olive oil mill wastewater. *Desalination and Water Treatment*, *57*(13), 5828-5836.

Ju, P., Fan, H., Guo, D., Meng, X., Xu, M. & Ai, S. (2012). Electrocatalytic degradation of bisphenol A in water on a Ti-based PbO_2–ionic liquids (ILs) electrode. *Chemical Engineering Journal*, *179*, 99-106.

Karami, H. & Alipour, M. (2009). Synthesis of lead dioxide nanoparticles by the pulsed current electrochemical method. *Int. J. Electrochem. Sci*, *4*, 1511-1527.

Lee, J., Varela, H., Uhm, S. & Tak, Y. (2000). Electrodeposition of PbO_2 onto Au and Ti substrates. *Electrochemistry Communications*, *2*(9), 646-652.

Li, C. H., Sengodu, P., Wang, D. Y., Kuo, T. R. & Chen, C. C. (2015). Highly stable cycling of a lead oxide/copper nanocomposite as an anode material in lithium ion batteries. *RSC Advances*, *5*(62), 50245-50252.

Li, X. Y., Cui, Y. H., Feng, Y. J., Xie, Z. M. & Gu, J. D. (2005). Reaction pathways and mechanisms of the electrochemical degradation of phenol on different electrodes. *Water Research*, *39*(10), 1972-1981.

Li, X., Xu, H. & Yan, W. (2016). Preparation and characterization of PbO_2 electrodes modified with polyvinyl alcohol (PVA). *RSC Advances*, *6*(85), 82024-82032.

Lin, Y. P. & Valentine, R. L. (2010). Reductive dissolution of lead dioxide (PbO$_2$) in acidic bromide solution. *Environmental Science & Technology*, *44*(10), 3895-3900.

Ni, J., Wang, H., Qu, Y. & Gao, L. (2013). PbO$_2$ electrodeposited on graphite for hybrid supercapacitor applications. *Physica Scripta*, *87*(4), 045802.

Perret, P., Khani, Z., Brousse, T., Bélanger, D. & Guay, D. (2011). Carbon/PbO$_2$ asymmetric electrochemical capacitor based on methanesulfonic acid electrolyte. *Electrochimica Acta*, *56*(24), 8122-8128.

Perry, D. L. & Wilkinson, T. J. (2007). Synthesis of high-purity α-and β-PbO and possible applications to synthesis and processing of other lead oxide materials. *Applied Physics A*, *89*(1), 77-80.

Rufino, É., Santana, M., Faria, L. & Silva, L. (2010). Influence of lead dioxide electrodes morphology on kinetics and current efficiency of oxygen-ozone evolution reactions. *Chemical Papers*, *64*(6), 749-757.

Sun, M., Liao, H. G., Niu, K. & Zheng, H. (2013). Structural and morphological evolution of lead dendrites during electrochemical migration. *Scientific Reports*, *3*, 3227.

Velichenko, A., Girenko, D. V., Kovalyov, S. V., Gnatenko, A. N., Amadelli, R. & Danilov, F. I. (1998). Lead dioxide electrodeposition and its application: influence of fluoride and iron ions. *Journal of Electroanalytical Chemistry*, *454*(1-2), 203-208.

Wulandari, S. (2017, November). Utilization of Pb and PbO$_2$ from lead storage battery waste for batik wastewater treatment using electrochemical method. *In Journal of Physics: Conference Series* (Vol. *909*, No. 1, p. 012074). IOP Publishing.

Xia, Y., Dai, Q. & Chen, J. (2015). Electrochemical degradation of aspirin using a Ni doped PbO$_2$ electrode. *Journal of Electroanalytical Chemistry*, *744*, 117-125.

Xiaping, H., ZHANG, R., Shaoping, T. & Chun'an, M. A. (2011). Preparation of Ti/PTFE-F-PbO2 electrode with a long life from the

sulfamic acid bath and its application in organic degradation. *Chinese Journal of Chemical Engineering*, *19*(6), 1033-1038.

Yamashita, J. & Matsumaru, Y. (1988). Studies on the microstructure of the positive lead-acid battery plate and its electrochemical reactivity. *Journal of Applied Electrochemistry*, *18*(4), 595-600.

Yu, L., Xue, J., Luo, Y., Tang, C. & Li, G. (2016). Ionic Liquids Assisted Electrodeposition and Electrocatalytic Activity of PbO_2 electrodes. *International Journal of Electrochemical Science*, *11*(2), 1199-1212.

Zerroual, L., Tedjar, F., Guitton, J. & Mousser, A. (1993). Mechanism of PbO_2 formation in lead/acid battery positive plates. *Journal of Power Sources*, *41*(3), 231-238.

Zhang, H. & Park, S. M. (1994). Electrochemical oxidation of manganese (II) in $HClO_4$ solutions. *Journal of the Electrochemical Society*, *141*(9), 2422-2429.

Zhang, X., Sun, Y. & Pan, J. (2017). A Clean and Highly Efficient Leaching–Electrodeposition Lead Recovery Route in $HClO_4$ Solution. *International Journal of Electrochemical Science*, *12*(8), 6966-6979.

Zhou, M., Dai, Q., Lei, L., Ma, C. A. & Wang, D. (2005). Long life modified lead dioxide anode for organic wastewater treatment: electrochemical characteristics and degradation mechanism. *Environmental Science & Technology*, *39*(1), 363-370.

Chapter 3

THERMALLY INDUCED ZNO NANOPARTICLES SYNTHESIS THROUGH BULK ADDITION METHOD: AN INNOVATIVE APPROACH

S. Praveen Kumar[1], S. Manikandan[2,], P. Mahiz Mathi[1] and D. Lingaraja[1]*

[1]MEMS Design Center,
Department of Electronics and Communication Engineering,
Saveetha Engineering College, Chennai, Tamilnadu, India
[2]Department of Biomedical Engineering,
Saveetha Engineering College, Chennai, Tamilnadu, India

ABSTRACT

Now a days, miniaturization technologies reign the modern world. The mass production of nano-materials and their related synergistic

---

* Corresponding Author's Email: kntm.gene@gmail.com.

compounds are yet to reach larger scale by the industries due to their conventional synthetic strategies. Among chemical precipitation process, the conventional drop wise addition method has been widely adopted for the synthesis of nanoparticles in which we obtain controlled morphological nano-material and those particle sizes would have been lesser than primary system. The conventional process poses longer time for reaction to occur and also for the formation of nanoparticles. Hence, we introduce a new innovative method called instant bulk addition process where it takes lesser time for the reaction and for the formation of nanoparticles with controlled morphology in large quantity. The novel bulk addition method results have been compared with conventional methods and the results show that bulk process at room temperature produces 4.64% mass higher than conventional method. Similarly, 7.64% higher mass was obtained from the bulk addition at 70°C. This also shows the results compared between the bulk addition processes in which reaction occurs at higher temperatures where it shows2.69% mass higher than the room temperature method. Analyzing the results such as morphological features, primary particle size, obtained mass and time taken for the formation of nanoparticles, bulk addition at higher temperature (SEM, XRD & mass %), show superiority because of the temperature influence which is more on reaction and nucleation process during synthesis.

Keywords: nanoparticles, instant bulk addition, dropwise addition, precursors, structural morphology, crystalline

NOMENCLATURE

Symbol	Meaning
K	Constant
Greek symbols	
λ	Wavelength of the incident X-ray beam
θ	Angle between the incident beam and the detector
B	Full Width at Half Maximum(FWHM)

INTRODUCTION

Nano technology is one of the emerging research fields among researchers because it brings knowledge from interdisciplinary fields like physics, chemistry, biology, medicine, etc. During 1960, Richard P. Feynman has made drastic development in the field of nanotechnology. In general, the Greek word nano means one billion or below 0.1 mm or 1-100nm [1,2]. Nanotechnology is used to produce the materials which are in nanosize [3–6]. The overall shape of Nano particles (Nps) can be used to identify the dimensions like 1D, 2D, 3D, etc. For example, the shape of nano sized rod, needles, spring, tubes, wires and belt help us to identify the Nps dimension that are in 1D. Similarly, Nano sized pellets, plates, sheets and nano sized flower, dandelion, snowflakes help us to find the dimension that are in 2D and 3D respectively [7].Though it is nano sized particle, it also have the following three layers, surface layer, shell layer and core layer. Due to its unique properties, it has imprinted its footprint almost in all the fields include biomedical, electronics and optics. Characterization of nano particles are highly dependent on the size, structure and shape. Due to its high surface area and small size, Nps exhibits unique physical, chemical and optical characteristics. Researchers have given their special attention towards these nanoparticles, when they realized that, the Nps have the potential of exhibiting different thermal and optical characteristics with respect to its size [8–28].

Synthesis Methods for Nanoparticles

Nanoparticle synthesis was carried out using different methods, each method having specificity for the synthesis of desired nanoparticles and it is shown in Figure 1. Top-down methods in which bulk material have been reduced to nanomaterials/nanosized particles

and whereas, in Bottom-up process the nanoparticle formation was initiated by a nucleation process from atom level. In both the approaches the Mechanical milling, Nanolithography, Sputtering, Chemical precipitation, Sol-gel, methods were specifically used for the synthesis of metal, metal oxide and polymeric nanoparticles. The Laser ablation, Thermal decomposition, Pyrolysis and Chemical vapor deposition methods were used for the synthesis of carbon based nanoparticles. Among the various methods of nanoparticle synthesis, chemical precipitation and sol-gel process was used widely for the preparation of metal, metal oxide nanoparticles, in which the preparation methodology was simple, time requirement could be lesser and procurement of precursors were quite easy, most of them were easily available in the chemical market.
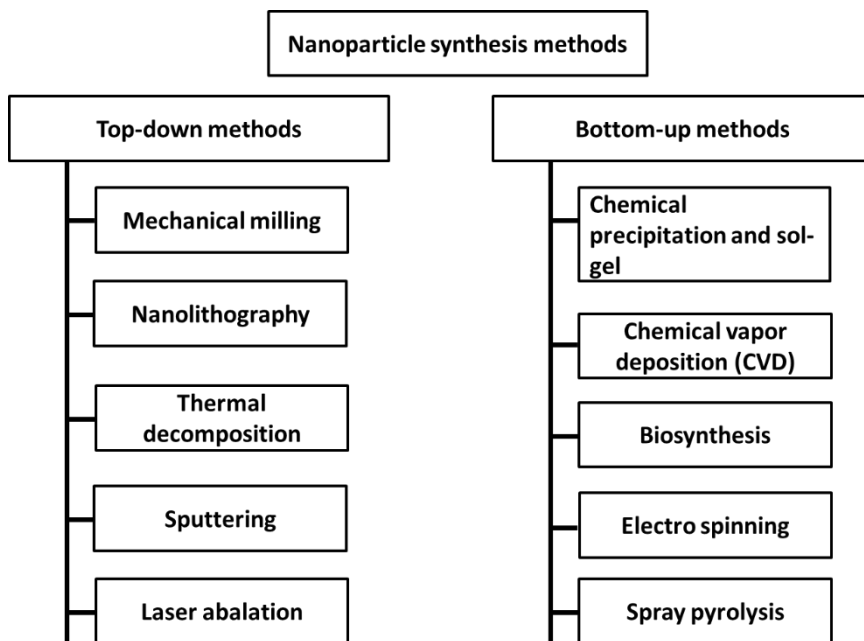
Figure 1. Schematic representation of different methods for nanoparticle synthesis.
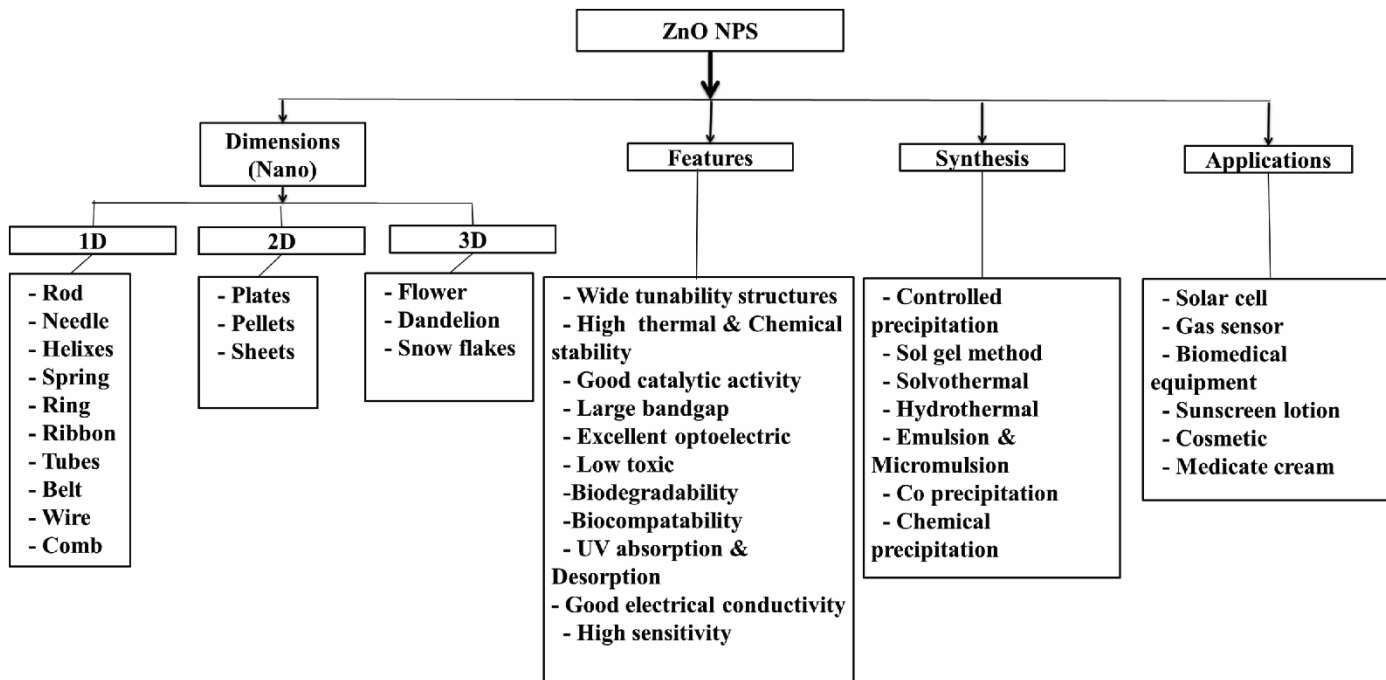
Figure 2. Schematic representation of properties and applications of ZnO nanoparticle.

ZnO is a semiconductor of N-type and an interesting material in II-VI compound in the periodic table [14,29,30]. The highlighted features of ZnO is that, it is non-toxic, highly applicable for doping and biodegradability [25,31]. To synthesize ZnO Nps, several methods like physical, chemical and metallurgical method are used. Among these methods, chemical methods are widely used due to its low cost, simple procedure and controllability in shapes [30,32–34]. Chemical methods may include sol-gel method, chemical precipitation method, co-precipitation, controlled precipitation, solvothermal, emulsion and micro emulsion, etc. Because of the simple methodology, less time consumption and fast response, chemical precipitation method is widely used. The shape, features and application of ZnO Nps are shown in Figure 2.

Even though, the conventional method has advantages in producing nanoparticles with controlled size and desired morphology, it also have some drawbacks such as utilizing more time for reaction to occur, very less mass was obtained and it may not be sufficient for industries for the production of nano products. Herein, we are reviewing new and novel synthesis of ZnO nanoparticles by conventional (drop wise) and bulk addition method at higher temperature and obtained results were showed that the excellent mass difference and morphological features was achieved at variable physical parameters.

MATERIALS AND METHODS

Materials

Double de-ionized water was used for the experiments. Precursors for the synthesis of Zinc oxide nanoparticles were Zinc nitrate hexahydrate and Ammonium carbonate procured from Merck, India and Fisher Scientific, India.

Methods

Preparation of Zinc Oxide Nanoparticles Using Drop Wise Addition: A Conventional Method

The equimolar concentration of well dispersed zinc nitrate hexahydrate and ammonium carbonate solutions was prepared individually using a magnetic stirring process. The reducing agent solution could be kept in the stirrer whereas, the precursor solution zinc nitrate is taken in the burette. The controlled dropwise addition of the precursor solution into reducing agent was carried out with a constant radial mixing at 500 rpm in magnetic stirrer. For the addition of 100 mL of the precursor solution into the reducing agent, it takes at least 10-12 hours and it is shown in Figure 3. The colloidal precipitate filtered off and dried under hot air condition in an oven until it completely gets dried without any moisture.
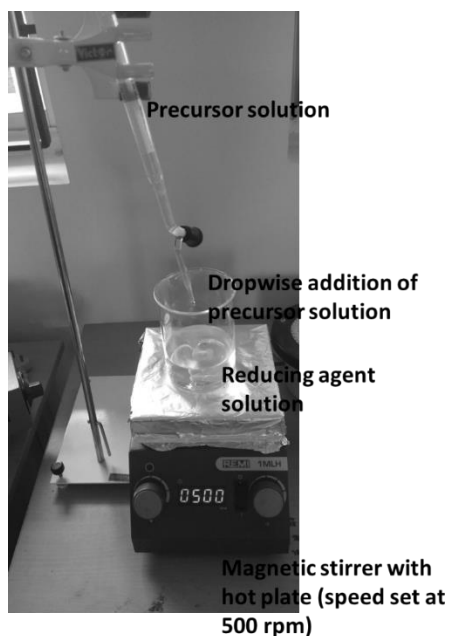
Figure 3. Photographic representations of dropwise addition method.

Preparation of Zinc Oxide Nanoparticles Using Bulk Addition Method at Higher Temperature

The bulk addition was carried out at higher temperatures above 70°C and addition has been done instantly within 5 minutes of time and it is shown in Figure 4. The colloidal precipitate could be filtered off and dried under hot air condition in an oven until it completely gets dried without any moisture.
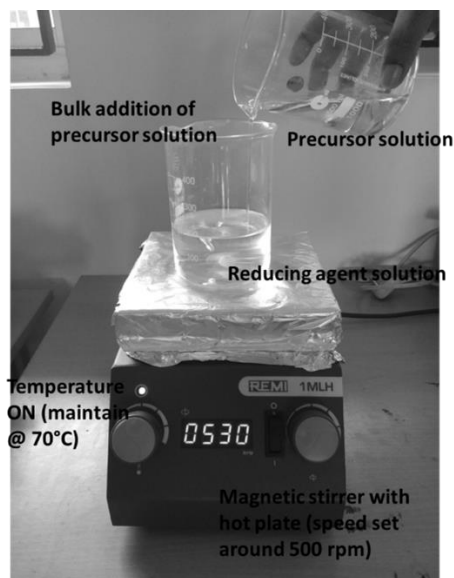
Figure 4. Photographic representations of Bulk addition method at higher temperature.

Preparation of Zinc Oxide Nanoparticles Using Bulk Addition Method at Room Temperature

Similarly, equimolar solutions are prepared in the bulk addition method and the individual solutions are mixed together instantly (within 5 minutes) with constant stirring using a magnetic stirrer. The instant mixing of precursor solution is carried out at room temperature, which is shown in Figure 5. The colloidal precipitate was filtered off and dried under hot air condition in an oven until it completely gets dried without any moisture.
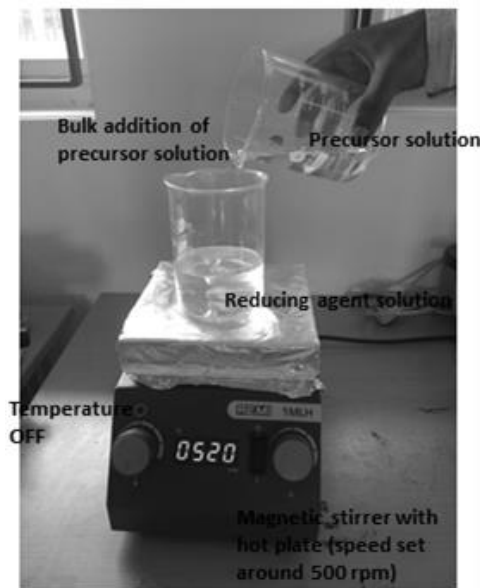
Figure 5. Photographic representations of Bulk addition method at room temperature.

Calcination Process

The obtained powder could be in zinc carbonate form. The transformation of zinc carbonate to Zinc oxide can be done through calcination process. The dried samples are kept in the crucible and heated up with 550°C for one hour in a muffle furnace.

Characterization of Zinc Oxide Nanoparticles

The crystalline nature of ZnO nanoparticles and transformation of zinc carbonate to zinc oxide has been confirmed through X-ray diffraction analysis (D8Focus, Bruker, Germany) in the 2θ range 20° to 80°. The primary particle size and morphological features of ZnO nanoparticles have been studied through Scanning Electron Microscopy (JSM 6701F, JEOL, Japan).

RESULT AND DISCUSSION

Precipitation Test: Formation of Nanoparticles

The precipitation test was performed with various molar (M) concentrations between precursor and reducing agent. In the Figure 6, it is observed that there is no visible formation of nanoparticles at lower concentrations such as 0.1 M, 0.2 M and in 0.3 M, whereas in 0.4 M the nanoparticles formation has been visualized and in 0.5 M concentration the formation was clearly visualized and has obtained larger mass. The precipitation test results states that the 0.5 M concentration shows better observation, hence 0.5 M concentration was chosen as the optimal concentration for nanoparticle synthesis.
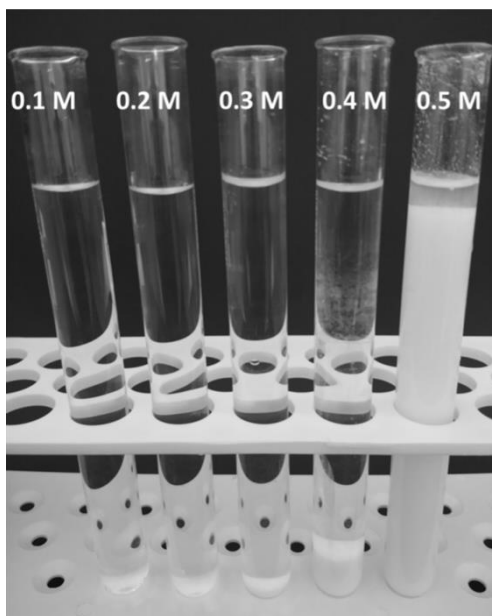
Figure 6. Visualization and analysis of precipitation at different molar concentration at room temperature: the formation of ZnO nanoparticles (it is in Zinc carbaonate form before calcination).

Comparative Study on Morphology and Crystallite Properties of ZnO Nanoparticles

(Why did you fix the temperature of 70°C) ZnO nanoparticles have been synthesized in three different methods: drop wise slow addition method, instant addition of higher temperature in 70°C and thirdly, instant bulk addition method at room temperature? Many literatures have stated that, the conventional Dropwise addition has resulted in the formation of nanoparticles with controlled morphology. The process of Dropwise addition is not suitable for mass production in Industries. Therefore, the consumption of Nanoparticles, large scale industries is still considered to be difficult. Figure 7 shows that the SEM images of the three different processes and their comparison, where the first sample details about the Dropwise addition method, in which ZnO Nps that are below 100 nm are formed. Similarly, Sample B also shows the formation of well-defined nanoparticles in which the primary particles are found to be below 100 nm in diameter and is obtained by the bulk addition method at 70°C. Sample C uses Bulk addition methods at room temperature where ZnO Nps are formed that are below 100 nm. In all these three processes, the synthesized ZnO Nps are below 100 nm but in the Bulk addition method at 70°C proves to be efficient with the formation of well-defined Nps. Therefore, the morphological properties of the proposed method are much better than the conventional method.

The X-ray diffraction characterization results (Figure 8a) shows that the well defined crystalline hexagonal ZnO nanoparticles were formed according to JCPDS card no. 75-0576. In Figure 8b, the elemental analysis results confirm that the obtained nanoparticles are zinc oxide whose crystallite size is 35.91206 nm could be calculated from Scherrer's formula [35, 36, 37] which is given below in equation (1)

$$D = \frac{K\lambda}{\beta \cos \theta} \tag{1}$$
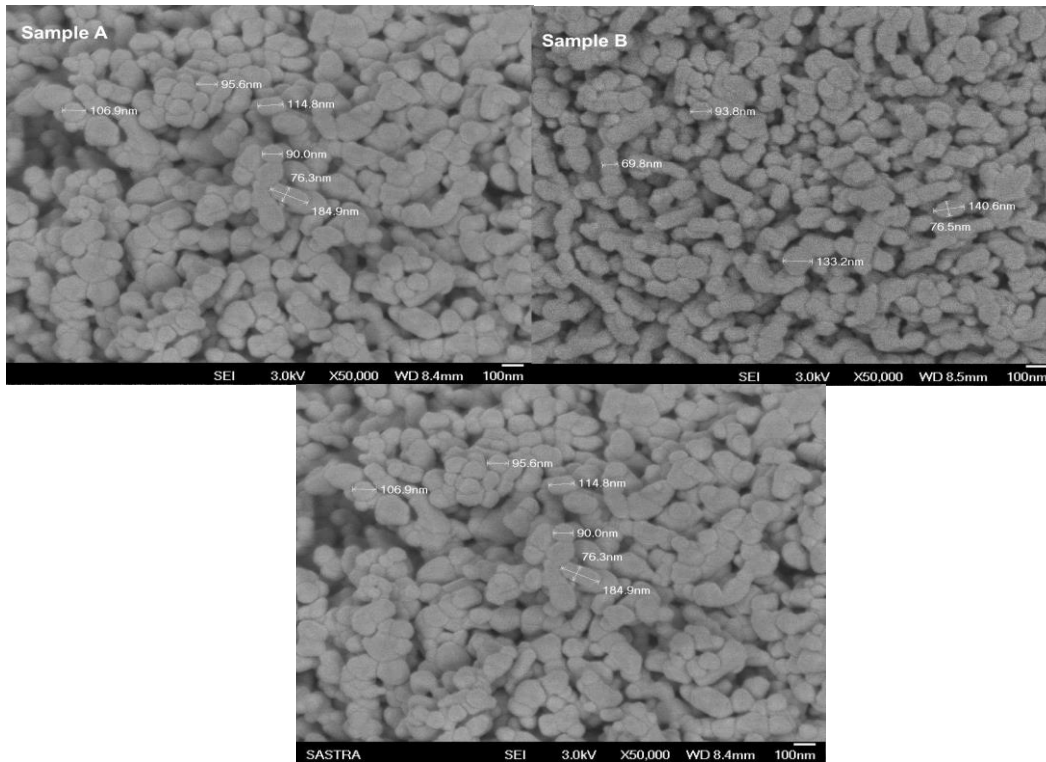
Figure 7. Morphology analysis (Scanning Electron Microscopy) of ZnO nanoparticles (a) Sample A: Dropwise method, (b) Sample B: Bulk addition at 70°C, and (c) Sample C: Bulk addition at room temperature.

Figure 8. (a) X-ray diffraction pattern of ZnO nanoparticles, and (b) Elemental analysis for the conformation of zinc oxide transformation from zinc carbonate through calcination process.

Mass Analysis

The conventional methods for nanoparticle synthesis have been widely used in which the process takes prolonged time for the reaction to occur between the precursor and the reducing agent. Hence, the reasonable amount of the mass of nanoparticles with controlled morphology can be obtained. Here the mass of the nanoparticles has been compared between conventional methods, the sample obtained from a bulk addition sample at higher temperature (70°C) and instant addition method at room temperature.

It is shown in the Figure 9, the mass of sample B is quite higher than that of the sample A and C, the reason behind that is the reaction process has been carried out at higher temperatures of 70°C. With the influence of temperature the complete reaction of precursors and reducing agent has taken place which is attributed to the production of the larger mass. The percentage mass difference of bulk addition, samples have been compared shown in Figure 10. The result states that, there is a 7.46% increase in the mass of sample B and 4.64% of sample C. Hence, the results show that at higher temperatures the precursors react fully and obtain the whole mass.
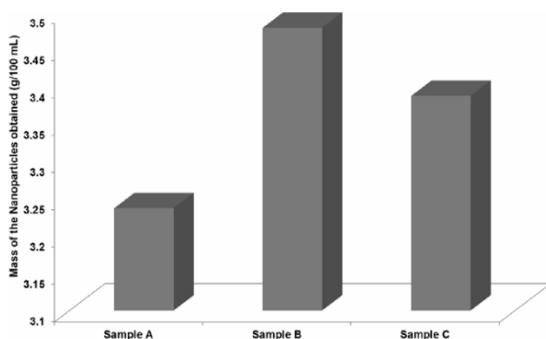
Figure 9. Determination of mass for calcined ZnO nanoparticles (a) Sample A: Dropwise addition method, (b) Sample B: Bulk addition at 70°C, and (c) Sample C: Bulk addition at roomtemperature.
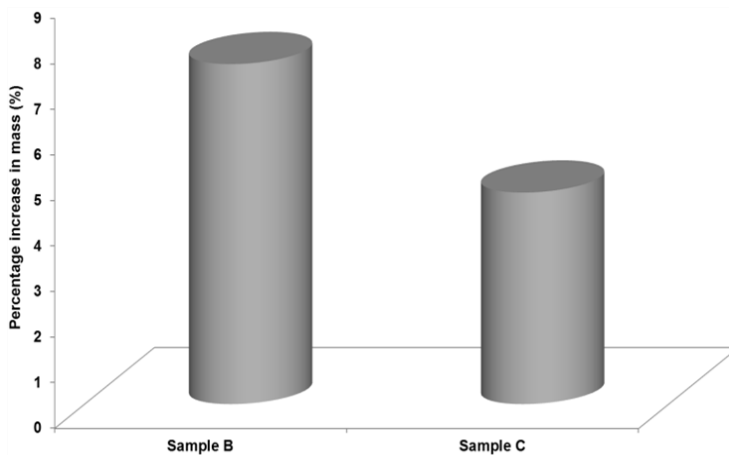
Figure 10. Determination of mass percentage forSample B: Bulk addition at room temperature, and Sample C: Bulk addition at 70°C.

CONCLUSION

The Zinc oxide nanoparticles around 100 nm size was prepared using three different methods. Dropwise conventional method consumes longer time (10-12 h) for the reaction and the formation of nanoparticles and mass obtained was 3.2370 g/100 mL. Whereas innovative bulk instant addition method at the room temperature process gives 3.3873 g/100 mL and at 70°C we obtained 3.4786 g/100 mL. The percentage comparison data of bulk samples with the dropwise method shows that the process at room temperature had an increase in mass percentage of 4.64% and for higher temperature processed sample it was 7.46%. The higher mass has been obtained at higher temperature and morphological features of bulk addition sample was similar to dropwise it could be the influence of higher temperature on nucleation process. The bulk instant addition the innovative process has been a successfully developed for the production of very large mass of nanoparticles in lesser time and this will promote the production of nanoparticles based products in larger scale in industries.

REFERENCES

[1] Khan, I., Saeed, K. & Khan, I. (2017). Nanoparticles: Properties, applications and toxicities, *Arab. J. Chem.* doi.org/10.1016/j.arabjc.2017.05.011.

[2] Lee, S., Choi, S. U. S., Li, S. & Eastman, J.A.(1999). Measuring Thermal Conductivity of Fluids Containing Oxide Nanoparticles, *J. Heat Transfer.*, *121*, 280–289. doi:10.1115/1.2825978.

[3] Shimpi, N.G., Jain, S., Karmakar, N., Shah, A.,Kothari, D. C. & Mishra, S. (2016). Synthesis of ZnO nanopencils using wet chemical method and its investigation as LPG sensor, *Appl. Surf. Sci.*,*3*, 216–221. doi:10.1016/j.apsusc.2016.08.050.

[4] Ganesh, R.S., Durgadevi, E., Navaneethan, M., Patil, V.L., Ponnusamy, S., Kawasaki, S.,et al., *AC SC* (2017). doi:10.1016/j.jallcom.2017.05.315.

[5] Manikandan,S., Karthikeyan, N., Silambarasan, M., Suganthi, K. S. & Rajan, K.S. (2012).Preparation and Characterization of sub-micron dispersions of sand in ethylene glycol-water mixture, *Brazilian J. Chem. Eng.*,*29*, 699–712.

[6] Manikandan, S. & Rajan, K.S.(2015). MgO-Therminol 55 nanofluids for efficient energy management: Analysis of transient heat transfer performance, *Energy.*,*88*, 408–416. doi:10.1016/j.energy.2015.05.061.

[7] Poloju, M., Jayababu, N. & Reddy, M.V.R. (2018). Materials Science & Engineering B Improved gas sensing performance of

Al doped ZnO/CuO nanocomposite based ammonia gas sensor, *Mater. Sci. Eng. B.*, *227*, 61–67. doi:10.1016/j.mseb.2017.10.012.

[8] Manikandan, S., Shylaja, A. & Rajan, K.S. (2014). Thermophysical properties of engineered dispersions of nano-sand in propylene glycol, *Colloids Surfaces A Physicochem. Eng. Asp.*,*449*, 8–18. doi:10.1016/j.colsurfa.2014.02.040.

[9] Manikandan, S. & Rajan, K.S. (2014). Rapid synthesis of MgO nanoparticles & their utilization for formulation of a propylene glycol based nanofluid with superior transport properties, *RSC Adv.*,*4*, 51830–51837. doi:10.1039/C4RA09173F.

[10] Leela Vinodhan, V., Suganthi, K. S. & Rajan, K.S. (2016). Convective heat transfer performance of CuO–water nanofluids in U-shaped minitube: Potential for improved energy recovery, *Energy Convers. Manag.*, *118*, 415–425. doi:10.1016/j.enconman. 2016.04.017.

[11] Chen, M., He, Y., Zhu, J. & Kim, D.R. (2016).Enhancement of photo-thermal conversion using gold nanofluids with different particle sizes, *Energy Convers. Manag.*, *112*, 21–30. doi:10.1016/ j.enconman.2016.01.009.

[12] Cabaleiro, D., Nimo, J., Pastoriza-Gallego, M.J., Piñeiro, M.M., Legido, L. & Lugo, J.L. (2015).Thermal conductivity of dry anatase and rutile nano-powders and ethylene and propylene glycol-based TiO_2 nanofluids, *J. Chem. Thermodyn.*,*83*, 67–76. doi:10.1016/j.jct.2014.12.001.

[13] Pokropivny, V., Hussainova, I. & Vlassov, S. (2007). *Introduction to Nanomaterials and Nanotechnology*, doi:978–9949–11–741–3.

[14] Hou, Y. & Jayatissa, A.H. (2017). *Progress in Natural Science: Materials International Influence of laser doping on nanocrystalline ZnO thin films gas sensors*. doi:10.1016/ j.pnsc. 2017.07.002.

[15] Farbod, M., Kouhpeymani asl, R. & Noghreh abadi, A.R. (2015). Morphology dependence of thermal and rheological properties of oil-based nanofluids of CuO nanostructures, *Colloids Surfaces A*

Physicochem. Eng. Asp., *474*, 71–75. doi:10.1016/j.colsurfa. 2015.02.049.

[16] Angayarkanni, S. A. & Philip, J. (2015). Review on Thermal Properties of Nanofluids: Recent Developments, *Adv. Colloid Interface Sci.*, *225*, 146–176. doi:10.1016/j.cis.2015.08.014.

[17] Wu, B., Lin, Z., Sheng, M., Hou, S. & Xu, J. (2015). Visible-light activated ZnO/CdSe heterostructure-based gas sensors with low operating temperature, *Appl. Surf. Sci.*, doi:10.1016/j.apsusc. 2015.11.037.

[18] Rohini Priya, K., Suganthi, K. S. & Rajan, K.S. (2012).Transport properties of ultra-low concentration CuO-water nanofluids containing non-spherical nanoparticles, *Int. J. Heat Mass Transf.*, *55*, 4734–4743. doi:10.1016/j.ijheatmasstransfer.2012. 04.035.

[19] Yang, L. & Du, K. (2017).A comprehensive review on heat transfer characteristics of TiO2 nanofluids, *Int. J. Heat Mass Transf.*, *108*, 11–31. doi:10.1016/j.ijheatmasstransfer. 2016.11.086.

[20] Asadi, M. & Asadi, A. (2016). Dynamic viscosity of MWCNT/ZnO–engine oil hybrid nanofluid: An experimental investigation and new correlation in different temperatures and solid concentrations, *Int. Commun. Heat Mass Transf.*, *76*,41–45. doi:10.1016/j.icheatmasstransfer.2016.05.019.

[21] Goutham, S., Kaur, S., Sadasivuni, K.K., Bal, J.K., Jayarambabu, N.,Kumar, D.S., et al. (2017). *Mater. Sci.Semicond. Process.*, *57*, 110–115. doi:10.1016/j.mssp.2016.09.037.

[22] Zhao, M., Wong, M.H., Man, H. C. & Ong, C.W. (2017). Resistive hydrogen sensing response of Pd-decorated ZnO "nanosponge" film, *Sensors Actuators B. Chem.*, doi:10.1016/ j.snb.2017.04.020.

[23] Devi, G.S., Reddy, P.S. P. & Ramya, K. (2016). Sol-Gel Derived ZnO: Nb_2O_5 Nanocomposite as Selective Hydrogen (H_2) *Gas Sensor.*, *3*, 224–229. doi:10.1016/j.matpr.2016.01.061.

[24] Khan, I.I., Saeed, K., Khan, I.I., Ganesh, R.S., Durgadevi, E.,Navaneethan, M., et al. (2007). Introduction to Nanomaterials and Nanotechnology, *Appl. Surf. Sci.*,*3*, 6–11. doi:978–9949–11–741–3.

[25] A. Manuscript, Biomedical Applications of Zinc Oxide Nanomaterials, (2014). *NIH Public Access.*, *13*, 1633–1645.

[26] Gu, C.,Huang, H., Huang, J., Jin, Z., Zheng, H. & Liu, N. (2016). Sensors and Actuators A : Physical Chlorobenzene sensor based on Pt-decorated porous single-crystalline ZnO nanosheets, *Sensors Actuators A. Phys.*, *252*, 96–103. doi:10.1016/j.sna. 2016.11.004.

[27] Bhatia, S., Verma, N. & Bedi, R.K. (2017).Ethanol gas sensor based upon ZnO nanoparticles prepared by different techniques, *Results Phys.*,*7*, 801–806. doi:10.1016/j.rinp.2017.02.008.

[28] Rasmussen, J. W., Martinez, E., Louka, P. & Wingett, D.G. (2010). Zinc oxide nanoparticles for selective destruction of tumor cells and potential for drug delivery applications, *Expert Opin. Drug Deliv.*, *7*, 1063–1077.

[29] Firkala, T., Nagy, Z. K. & Baji, Z. (2017). TiO$_2$/ZnO and ZnO/TiO$_2$ core/shell nanofibers prepared by electrospinning and atomic layer deposition for photocatalysis and gas sensing, *Appl. Surf. Sci.*,*424*, 190–197. doi:10.1016/j.apsusc.2017.03.030.

[30] Basha, S.K., Lakshmi, K.V. & Kumari, V.S. (2016). Sensing and Bio-Sensing Research Ammonia sensor and antibacterial activities of green zinc oxide nanoparticles, *SBSR.*, *10*, 34–40. doi:10.1016/j.sbsr.2016.08.007.

[31] Hassana, H.S.,Kashyouta, A.B., Morsib, I. & Nasserb Ibrahim Alib, A.A.A. (2014). Synthesis,characterization and fabrication of gas sensor devices using ZnO and ZnO : In nanomaterials, *Beni-Suef Univ. J. Basic Appl. Sci.*, 2–7. doi:10.1016/j.bjbas. 2014.10.007.

[32] Suganthi, K. S., Leela Vinodhan, V. & Rajan, K.S. (2016). ZnO–Propylene Glycol–Water Nanofluids with Improved Properties for Potential Applications in Renewable Energy and Thermal Management, *Colloids Surfaces A Physicochem. Eng. Asp.*, *506*, 63–73. doi:10.1016/j.colsurfa.2016.06.007.

[33] Suganthi, K. S., Anusha, N. & Rajan, K.S. (2013). Low viscous ZnO–propylene glycol nanofluid: a potential coolant candidate, *J. Nanoparticle Res.*, *15*,1986. doi:10.1007/s11051-013-1986-6.

[34] Suganthi, K. S. & Rajan, K.S. (2014). A formulation strategy for preparation of ZnO–Propylene glycol–water nanofluids with improved transport properties, *Int. J. Heat Mass Transf.*, *71*, 653–663. doi:10.1016/j.ijheatmasstransfer.2013.12.044.

[35] Sivapalan, B., Neelesh Chandran, M., Manikandan, S., Saranprabhu, M. K., Pavithra, S. & Rajan, K.S. (2018). Paraffin wax–water nanoemulsion: A superior thermal energy storage medium providing higher rate of thermal energy storage per unit heat exchanger volume than water and paraffin wax. *Energy Conversion and Management*, 162/2018, 109-118. DOI: 10.1016/j.enconman.2018.01.073.

[36] Manikandan, S. & Rajan, K.S. (2017). New hybrid nanofluid containing encapsulated paraffin wax and sand nanoparticles in propylene glycol-water mixture: Potential heat transfer fluid for energy management. *Energy Conversion and Management*, 137/2017, 74–85. DOI: 10.1016/j.enconman.2017.01.033.

[37] Neelesh Chandran, M., Manikandan, S. & Rajan, K.S. (2017). Novel hybrid nanofluid with tunable specific heat and thermal conductivity: Characterization and performance assessment for energy related applications. *Energy*, 140/2017, 27-39.DOI:10. 10.1016/j.energy.2017.08.056.

Chapter 4

AUTOMATIC DETECTION OF *MALARIAL PARASITEMA* USING EFFICIENT FRACTAL ANALYSIS

Prabha Sathees[*]

Department of ECE, Hindustan Institute
of Technology and Science, Chennai, India

ABSTRACT

In this work, an ingenious process has been proposed for automatic detection of parasitic protozoa of the genus plasmodium based on the technical developments in the arena of bio imaging processing. The investigation of malaria in clinical diagnosis is basically the explicit microscopic estimate of the parasite. Generally, blood smears are collected and then stained with romanowsky stain and red blood cells are examined for intercellular malaria parasite. The red corpuscles in the blood samples of vertebrates consist of precise structure if infected that helps to recognize their existence. Fractal based threshold analysis has been implemented in this paper to categorize the kind of parasite by their

---

[*] Corresponding Author's Email: harprabha@gmail.com.

color and shape. The existence of *Malarial parasitema* and its severity can be detected within seconds using this technique and consequently can substitute the conventional approaches. Fractal based malarial detection technique is proposed to minimize human reliance and hence it is high reliable in applying diagnostic benchmark. Thus, this technique has an ability to carry out the diagnosis in a robust and unsupervised manner.

Keywords: malaria, parasite, shape detection, fractal analysis

INTRODUCTION

Protozoan parasites are the reason for creating the disease malaria that is spreaded from one individual to another by the Anopheles mosquito. The bug is formed by tiny parasitic protozoa of the genus Plasmodium, that firstly contaminate the liver cells of human, secondly the red cells, and finally the insect hosts instead. The present manual laboratory exposing technique includes determination of contaminated blood slides through visual inspection. Erroneous analysis leads to other secure complications and hence proper care is needed for diagnosis (Raviraja et al., 2011).

Three types of blood cells such as RBC, WBC, platelets have disparate dimensions and color. Initially, the arrival of parasites into blood stream influences RBC blood cells. The malarial parasites acclimate to divergent environment in vertebrate host as well as mosquito vector in variety of different forms. These parasites develop through different cycles in their vertebrate host. They exhibit several shapes and stages of development during the lifecycle of plasmodium. They endure in the design of slide and hence for diagnose protozoan's presence, the blood has to be investigated in image format. Plasmodium cell surface are generally in the range of 6-8 μm with three different shapes such as spherical, cylindrical and elliptical. There are four different types of plasmodium parasite based on which it is classified

and the result is indicated (Ruberto et al., 2000). The four types are explained as follows:

PLASMODIUM VIVAX

Plasmodium vivax is a protozoan parasite, the development of it becomes amoeboid in shape and its size is 2.5 µm. vivax schizonts have 12-24 merozoites yellowish brown coalesced pigments, whereas tropozoites have tight cytoplasm and enormous chromatin dot.

PLASMODIUM OVALE

The parasitic protozoa which agenting tertian malaria in humans is known as *Plasmodium ovale*. Ovale schizonts basically consist of 6-14 merozoites having huge nuclei, clustered in the region of mass dark brown pigments where as tropozite have bulky cytoplasm with broad chromatin dots. In comparison to *Plasmodium vivax* the pigments are brown and coarser.

PLASMODIUM FALCIPARUM

Main dangerous one in the plasmodium parasite is the *Plasmodium falciparum*. The *Plasmodium falciparum* consist of elegant cytoplasm and very few cramped chromatin dots. The trophozoites actually refer to older ring stage parasites. Trophozoites having cytoplasm is much denser then in younger rings. Schizonts are very rarely in peripheral blood.

PLASMODIUM MALARIAE

The parasitic protozoan that agenting malaria in human is called *Plasmodium malariae*. Rings and trophozoites are the two forms of *Plasmodium malariae*. These rings consist of hulking cytoplasm and extensive chromatin dots of size 6.5-7μm. the trophozoites have solid cytoplasm and a enormous chromatin dot (Raviraja et al., 2011).

There are two major methods for detection of malaria parasites: microscopy and rapid diagnostic tests (RDTs). Microscopy is superior over RDTs with esteem to costs and is diagnosed as the gold standard in parasite quantification (Wongsrichanalai et al., 2007). Yet, microscopy necessitates skilled operators, maintenance of equipment, and capital investment. Microscopy is time consuming particularly in regions with high caseload and this issue typically results in variable reports (Meara et al., 2006) and poor performance (Wongsrichanalai et al., 2007; Zhu et al., 2013). The microscopy results attained by human operators shows that the accuracy is unpredictably low and only 51% of parasite quantification tasks are satisfactory (Frean et al., 2012). The cure is to minimize the human role in the diagnosis process. Diverse features such as color, texture and shape from images are used by more researches for vision-based detection and quantification of malaria parasites (Tek et al., 2009; Mehrjou et al., 2014). Diagnosing malarial disease with vision-based methods are generally supervised and must contract with subjects like staining quality, illumination variability, image pre-processing, feature extraction, feature selection and classification schemes (Tek et al., 2009). Deliberating the high infection rates and enormous amount of image data, we need a fast-accurate method with minimum human intervention which is robust against diverse sources of disparities.

The malarial parasites exposed to diverse environment in both the vertebrate host and mosquito vector in variety of different forms. These parasites develop through different cycles in their vertebrate host

(Ruberto et al., 2011). They exhibit several shapes and stages of development during the lifecycle of plasmodium. They survive in the shape of slide and hence to diagnose protozoan's presence, first analyzing blood samples in the arrangement of image format. The cell surface of the plasmodium is in the range of 6-8μm with spherical, cylindrical and elliptical shapes (Ruberto et al., 2011).
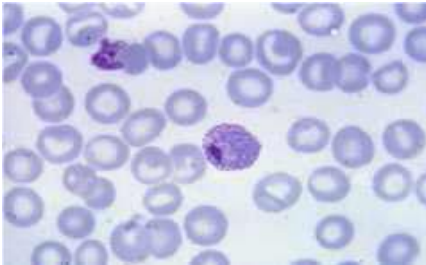
Figure 1 (a). *Plasmodium vivax.*
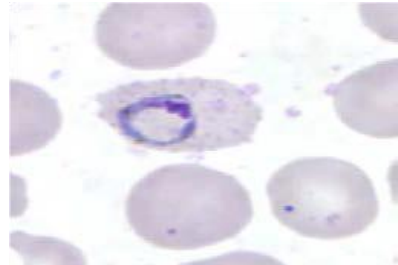
Figure 1 (b). *Plasmodium ovale*.
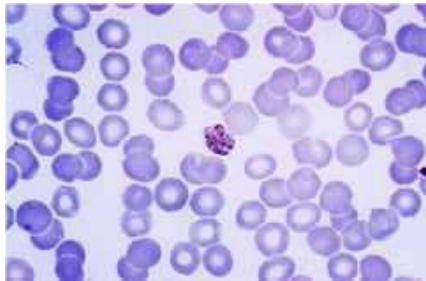
Figure 1 (c). *Plasmodium malariae*.
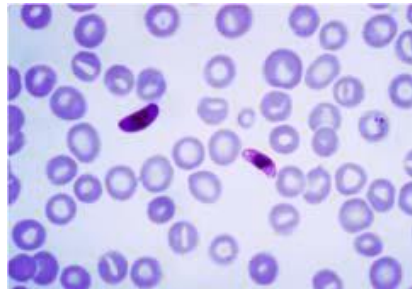
Figure 1 (d). *Plasmodium falciparum*.

In the existing methodology these parasites are detected using microscopy technique with the help of man power and its takes nearly a half to determine the result. These parasites multiply in large number inside the cells if late diagnosis is made. Another method called rapid diagnostic test is also used in which antigen is added with the blood cells to indicate the presence of parasitema.

Edge detection is the approach used most frequently for segmenting images depend on intensity changes locally (Prabha et al., 2014; Suganthi & Ramakrishnan, 2014). Edge models are divided dealing to the profile of their intensity. A step edge includes a evolution between intensity levels of two happening preferably concluded the distance of 1pixel. For example, images are created by a computer for practice in zones such as compact modeling and animations. There perfect, ideal edge can happen over the distance of 1 pixel, afforded that no addition action is adopted to make them to look "real". The step edges in digital are used regularly as edge models in procedure growth. For example, the canny edge detection algorithm was derived using step-edge model.

Another type of edge model is roof edge. It is having the lines over a region, in which the base of roof edge being resolute by the density and sharpness of the line. Roof edge arises, for example, the ranges of images having thin object are closer to the sensor that their equidistant background the pipes appear brighter and thus create an image similar to the model.

It is not unusual to find images that contain all three types of edges. Although blurring and noised result in deviations for the ideal shapes, the edges in images that are reasonable sharp and have a moderate amount of noise do resembles the characteristics of the edge models. Even a simple region descriptor such as normalized area can be quite useful in extracting information from images. Images such as a provide a global inventory of human settlements. The sensor use to collect these images as the capability to detect visible and near infrared emissions, such as lights fires and flares. The table alongside the images shows the area having ratio occupied by the white to the total light area in all four regions. Simple measurements like this can give, for example, a relative estimate by region of electrical energy consumed.

Consider the two M*N color images composed of the three component images. The gradient of each of the component images are computed and the results were added to form the two corresponding RGB gradient images, the value of the gradient at point

[(M+1)/2,(M+1)/2] would be the same in both cases. The gradient at that point is stronger for the image because the edges of the R, G and B images are in the same direction in that image, as opposed to the image in which only two of the processing the three individual planes to form a composite gradient image can yields erroneous results.

The amount of edge is sensibly associated to spatial heterogeneity which is recognized by edge detection image processing techniques (Prabha et al., 2015). Spatial heterogeneity is captured in improved way of methodology using fractal analysis (Xu et al., 2010).

Fractal geometry is illustrated by means of fractal tools that permits detaining heterogeneity of irregular shapes which is unavailable in conventional representation of geometry (Lopes & Betrouni, 2009). Fractal analysis is an effective approach that would be used for characterizing the image statistically (Stosic & Stosic, 2006). It reflects the real features of the image accurately since it is associated with the probability of pixel distribution. Detecting fractal dimension is an essential step in any fractal analysis, since it conveys information about their geometric structure.

Nonlinear fractal analysis was applied for finding the erythrocyte aggregation composed by progress of RBC through Ascaris lumbricoides and Trichinella spirallis larvae excerpt (Lupo et al., 2016). Estimation of fractal signatures and multifractal spectrum are applied for complex structured images to perform segmentation (Ampilova et al., 2016). Segmentation of blood cells with morphological process is a asserting owing to complication of the cells. Rao's method and bounding box is adapted for segmentation and finally, ANN is used for classification of malarial parasites (Razzak 2015).

Fuzzy involved color image segmentation along with the features that are extracted by fractal through ARTNN classifier has been implemented for the detection of malaria in blood slides. Quantification of micro structural alterations of malaria parasites is very difficult. Quantitative analysis which is performed through the different types of classifier such as SVM, NN-BPFF and KNN for the investigation

ofmalaria parasite in image dataset. In these analysis, 94.45% accuracy, 96.41% precision, 94.68% specificity and 94.32% sensitivity are reported for image dataset using various classifiers (Chayadevi & Raju, 2014).

Recent progresses in image investigation and machine learning methods are used to enumerate parasitemia for improved diagnosis in the detection of malaria (Poostchi et al., 2018). Screening of malarial parasite involves the description of erythrocytes that plays a major role in microscopic image analysis. Illustration of malaria infected and non-infected erythrocyte are reviewed with diverse features (Devi et al., 2016). Innovative method of Morphological model is adapted for the investigation of malaria parasite and also recent literature are reviewed about the computer aided diagnosis for detecting the approaches in malaria exposure (Loddo et al., 2018).

An effective feature extraction technique named as SFTA has been proposed to identify protozoan existence for realization. The detection method comprises a set of binary image which is portioned from original image from that the dimensions of fractal for the regions' borders are estimated to characterize the patterns of texture segmentation. SFTA method divulge diverse division of pixels and distinguish dissimilarities within the image. This technique can characterize both the roughness of the texture and its anisotropy. It is proficient of explaining the features of image as local and global spot of vision (Costa et al., 2012; Prabha et al., 2017).

The proposed methodology gives a general idea about the arrangement of various components of the automated identification of *Malarial parasitema* and its severity. The blood smear taken from the patient for the identification of malaria is kept under the microscopic camera for its image to be captured. The captured blood smear images are given to PC and programming is done to analyze the blood sample.

METHODOLOGY

The first step involves the collection of blood smears which can be either thin or thick. The test samples were collected for identification of malaria from various diagnostic centers that have specialized technicians and laboratory facilities. Also, we made a survey and also collected blood smears of different parasite affected malarial blood samples. We collected samples from different government organizations such as Central Malarial Laboratory at DMS (Teynampet) Rajiv Gandhi Government General Hospital (Central), Kings Institute of Preventive Medicines (Guindy) and also from private organizations such as Bharat Scans etc.

The samples collected are then stained for further diagnosis. There are different strains used namely Leishmen stain, Geimsa stain, Romanowsky stain. The Romanowsky stain is used here and the added blood smear is then examined using a microscopic camera. The USB microscopic camera used allows the users to drive deep into exploration of microscopic images and specimen. The magnification level start from 10X the sample of original image and extend to 60X or even 200X sample for investigating it in even deeper level. The resolution of the camera is about 640X480. The microscopic image is then sent to the personal computer which uses Matlab software to identify the presence and the type of parasites.

The automatic finding of malaria parasite in red blood cells is detected without human intervention and the process is automated. The parasites can be segmented based on Segmentation-based Fractal Texture Analysis (SFTA). SFTA extraction algorithm is isolated as two parts in which first part disintegrates the original image as a set of binary images. This process is attained by means of TTBD technique. Second part describes the fractal dimensions, mean gray level and size which are computed from the obtained image.

The original image $K(x, y)$ is divided into set of binary images that is named as Two-Threshold Binary Decomposition (TTBD). Features such as Fractal dimension (FD), mean gray level (MGL) and pixel count (PC) are acquired from these set of binary images. Binarization of images is achieved through the setting of lower and upper threshold value which is selected by means of Otsu method.

A set of binary images are obtained from the original image using TTBD procedure. A pair of thresholds are attained by implementing two-threshold segmentation technique which is described as

$$K_b(x, y) = \begin{Bmatrix} 1 \; if\, t_l < K(x,y) < t_u \\ 0 \quad\quad otherwise \end{Bmatrix} \tag{1}$$

where the lower and upper threshold values are denoted as t_l and t_u respectively (Costa et al. 2012).

RESULTS

The investigation procedures in automatic classification of malarial parasite is one of the major complex task since the complication involved in the segmentation of infected blood cells alone from the background and other cells. Cell shapes, light variation and noise are the other issues that make segmentation a complicated job. Accurate segmentation permits profitable consequence in sub-sequent levels. Cell segmentation desires to be precise to calculate the exact parasitemia. However, extracting cells in particular complicate the identification and segmentation of individual cells. For this problem, segmentation of objects and regions in medical images requires features which can afford explicit discernment (Prabha et al., 2014). Hence, segmentation-based fractal analysis is found to be adequate for this process.

Generally, the morphological analysis and segmentation of malaria cells is a challenging one owing to both the intricate cell nature and

ambiguity in microscopic videos. To progress the performance of malaria parasite analysis, diverse set of features are selected for malaria classification. The set of binary images are acquired by applying threshold segmentation technique from above equation in which multilevel Otsu algorithm is implemented for the calculation of thresholds. SFTA feature extraction process are resulted as fractal dimension, mean gray level and size which are achieved by two threshold binary decomposition technique. Box counting algorithm is utilized for proficiently calculation of fractal dimension in linear time. SFTA necessitates to establish the parameter nt which describes the number of thresholds that will be engaged in the input image decomposition. SFTA method shows the malarial parasite results in Figure 2 and Figure 3.
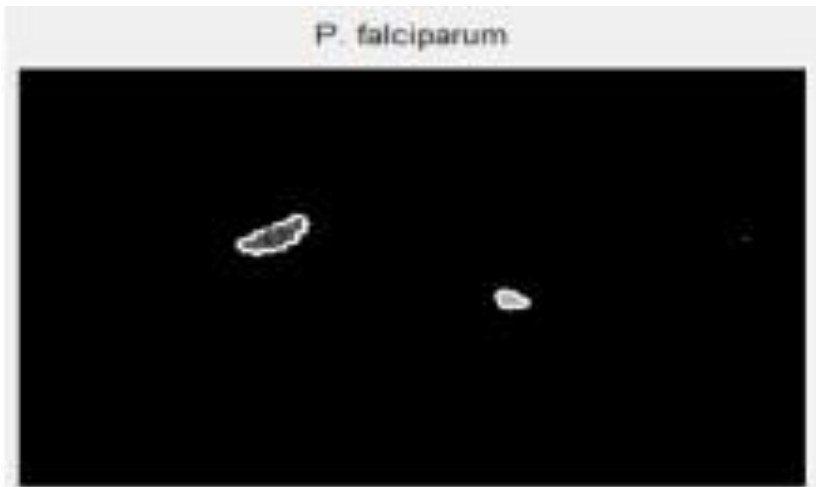
Figure 2. Structure and type of parasite detected.

The aim of diagnosis is the detection of different parasites regarding different varieties. It is implemented by clicking the "type of parasite" that afford the name of parasite by evaluating the sample of image with diverse parasite samples of stored data. Figure 3 shows that the
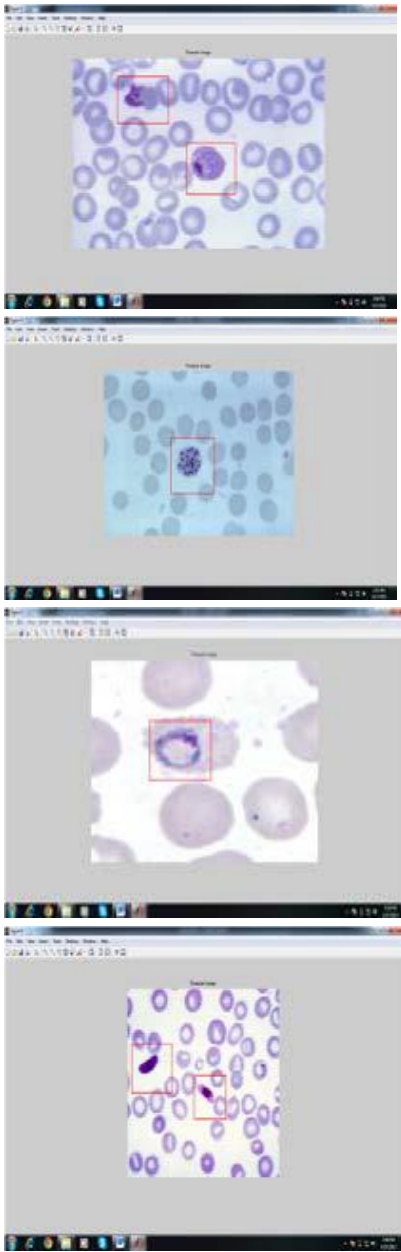
No. Of Cells affected: 2
Pixel Area of Parasite 1: 1.2230
Pixel Area of Parasite 2: 1.3620
Fractal Dimension : 1.90
P.VIVAX - DETECTED

No. Of Cells affected :1
Pixel Area of Parasite : 0.7320
Fractal Dimension: 1.88
P.MALARIAE-DETECTED

No. Of Cells affected: 1
Pixel Area of Parasite: 1.7030
Fractal Dimension : 1.86
P.OVALE - DETECTED

No. Of Cells affected : 2
Pixel Area of Parasite 1: 0.2670
Pixel Area of Parasite 2: 0.1050
Fractal Dimension: 1.91
P.FALCIPARUM-

Figure 3. Left side denotes the highlights of affected cells and Right side denotes the identification of types of parasites from SFTA features.

automatic diagnosis method is adequate to identify the presence of malaria parasite within seconds and its severity of the samples are analyzed which has resulted in better accuracy. This method thus can substitute the conventional methods of recognition of malaria in bio-medical applications. The number of parasite which affected the severity can be determined. The structure and type of the detected parasite is shown in Figure 2.

The output window for four types of malaria affected blood samples in Figure 3.

The chapter presented a method for automatic detection of different types of malarial parasites. User friendly environment is also afforded with the assistance of simple GUI that produces consequences devouring limited time and man power as compare to conventional methods. The adaptation of this methodology can be enhanced for the detection of other objects like various other parasites and viruses. Erroneous results are decreased to enormous amount by this approach.

CONCLUSION

The algorithm presented in this chapter is limited to the basic diagnosis of malaria with the types of parasite causing the malaria. This automatic diagnosis technique is able to detect the existence of malaria parasite within seconds and its severity which resulted in better accuracy. This method thus can replace the conventional methods of detection of malaria in bio-medical applications. Further a user friendly environment is also provided with the help of simple GUI which produces results consuming lesser time and man power as compare to conventional methods. The application of this algorithm can be extended to be used for the detection of other objects like various other parasites and viruses. Errors in results can be reduced to a great extent by using this project.

REFERENCES

Allain, C. & Cloitre, M. (1991). Characterizing the lacunarity of random and deterministic fractal sets. *Physical Review A*, *44*(6), 3552.

Ampilova, N. & Soloviev, I. (2016). Application of Fractal and Multifractal Analysis Algorithms to Image Segmentation and Classification. *WSEAS Transactions on Biology and Biomedicine*, *13*, 14-21.

Chayadevi, M. & Raju, G. (2014). Usage of art for automatic malaria parasite identification based on fractal features. *Int. J. Video Image Process. Netw. Secur*, *14*, 7-15.

Costa, A. F., Humpire-Mamani, G. & Traina, A. J. M. (2012, August). An efficient algorithm for fractal analysis of textures. In *25th SIBGRAPI Conference on Graphics, Patterns and Images (SIBGRAPI), 2012* (pp. 39-46). IEEE.

Dathe, A., Tarquis, A. M. & Perrier, E. (2006). Multifractal analysis of the pore-and solid-phases in binary two-dimensional images of natural porous structures. *Geoderma*, *134*(3-4), 318-326.

de Melo, R. H. C. (2007). *Using fractal characteristics such as fractal dimension, lacunarity and succolarity to characterize texture patterns on images*. Universidade Federal Fluminense, Niterói, Brazil.

Dempster, A. & Di Ruberto, C. (1999). Morphological processing of malarial slide images. In *Matlab DSP Conference* (pp. 16-17).

Devi, S. S., Sheikh, S. A. & Laskar, R. H. (2016). Erythrocyte Features for Malaria Parasite Detection in Microscopic Images of Thin Blood Smear: A Review. *IJIMAI*, *4*(2), 34-39.

Di Ruberto, C., Dempster, A., Khan, S. & Jarra, B. (2000). Automatic thresholding of infected blood images using granulometry and regional extrema. In *Proceedings*. *15th International Conference on Pattern Recognition, 2000.* (Vol. *3*, pp. 441-444). IEEE.

Di Rubeto, C., Dempster, A., Khan, S. & Jarra, B. (2000). Segmentation of blood images using morphological operators. In *Proceedings. 15th International Conference on Pattern Recognition, 2000* (Vol. *3*, pp. 397-400). IEEE.

Dougherty, G. & Henebry, G. M. (2001). Fractal signature and lacunarity in the measurement of the texture of trabecular bone in clinical CT images. *Medical Engineering & Physics*, *23*(6), 369-380.

Esgiar, A. N. & Chakravorty, P. K. (2005, September). Wave nature of fractal lacunarity: a higher resolution scale to capture subtle changes in ECG signals. In *Computers in Cardiology*, 2005 (pp. 1009-1012). IEEE.

Falconer, K. (2004). *Fractal geometry: mathematical foundations and applications*. John Wiley & Sons.

Frean, J., Perovic, O., Fensham, V., McCarthy, K., Gottberg, A. V., Gouveia, L. D., ... & Alemu, W. (2012). External quality assessment of national public health laboratories in Africa, 2002-2009. *Bulletin of the World Health Organization*, *90*, 191-199.

Gefen, Y., Meir, Y., Mandelbrot, B. B. & Aharony, A. (1983). Geometric implementation of hypercubic lattices with noninteger dimensionality by use of low lacunarity fractal lattices. *Physical Review Letters*, *50*(3), 145.

Keller, J. M., Chen, S. & Crownover, R. M. (1989). Texture description and segmentation through fractal geometry. *Computer Vision, Graphics, and Image Processing*, *45*(2), 150-166.

Landini, G. (2011). Fractals in microscopy. *Journal of Microscopy*, *241*(1), 1-8.

Lee, W. L., Chen, Y. C. & Hsieh, K. S. (2003). Ultrasonic liver tissues classification by fractal feature vector based on M-band wavelet transform. *IEEE Transactions on Medical Imaging*, *22*(3), 382-392.

Loddo, A., Di Ruberto, C. & Kocher, M. (2018). Recent Advances of Malaria Parasites Detection Systems Based on Mathematical Morphology. *Sensors*, *18*(2), 513.

Lupo, M., Leguto, A. J., Bortolato, S. A. & Korol, A. M. (2016). Evolution of erythrocytes aggregation: A fractal approach when incubated with Trichinella spiralis and Ascaris lumbricoides. *Ain Shams Engineering Journal*.

Mehrjou, A., Abbasian, T. & Izadi, M. (2013, February). Automatic malaria diagnosis system. In *2013 First RSI/ISM International Conference on Robotics and Mechatronics (ICRoM)* (pp. 205-211). IEEE.

O'Meara, W. P., Barcus, M., Wongsrichanalai, C., Muth, S., Maguire, J. D., Jordan, R. G., ... & McKenzie, F. E. (2006). Reader technique as a source of variability in determining malaria parasite density by microscopy. *Malaria Journal*, *5*(1), 118.

Poostchi, M., Silamut, K., Maude, R., Jaeger, S. & Thoma, G. (2018). *Image Analysis and Machine Learning for Detecting Malaria*. Translational Research.

Prabha, S., Anandh, K. R., Sujatha, C. M. & Ramakrishnan, S. (2014, August). Total variation based edge enhancement for level set segmentation and asymmetry analysis in breast thermograms. In Engineering in Medicine and Biology Society (EMBC), 2014 *36th Annual International Conference of the IEEE* (pp. 6438-6441). IEEE.

Prabha, S., Suganthi, S. S. & Sujatha, C. M. (2015). An approach to analyze the breast tissues in infrared images using nonlinear adaptive level sets and Riesz transform features. *Technology and Health Care*, *23*(4), 429-442.

Prabha, S., Suganthi, S. S. & Sujatha, C. M. (2017, December). Analysis of Breast Thermal Images Using Anisotropic Diffusion Filter Based Modified Level Sets and Efficient Fractal Algorithm. In *International Conference on Cognitive Computing and Information Processing* (pp. 10-17). Springer, Singapore.

Rapa A (2005). Fractal dimensions in red blood cell. *Turk J Vet Ani Sci*, *29* (6), 1247–53.

Raviraja, S., Bajpai, G. & Sharma, S. K. (2007). Analysis of detecting the malarial parasite infected blood images using statistical based approach. In *3rd Kuala Lumpur International Conference on Biomedical Engineering 2006* (pp. 502-505). Springer, Berlin, Heidelberg.

Razzak, M. I. (2015). Automatic detection and classification of malarial parasite. *International Journal of Biometrics and Bioinformatics (IJBB)*, *9*(1), 1-12.

Razzak, M. I. & Alhaqbani, B. (2015). Automatic detection of malarial parasite using microscopic blood images. *Journal of Medical Imaging and Health Informatics*, *5*(3), 591-598.

Royal Perth Hospital, Western Australia, *Malaria*, An on-line Resource Website: http://rph.wa.gov.au/malaria.html.

Smyth, J. D. & Wakelin, D. (1994). *Introduction to animal parasitology.* Cambridge University Press.

Suganthi, S. S. & Ramakrishnan, S. (2014). Anisotropic diffusion filter based edge enhancement for segmentation of breast thermogram using level sets. *Biomedical Signal Processing and Control*, *10*, 128-136.

Tek, F. B., Dempster, A. G. & Kale, I. (2009). Computer vision for microscopy diagnosis of malaria. *Malaria Journal*, *8*(1), 153.

Wongsrichanalai, C., Barcus, M. J., Muth, S., Sutamihardja, A. & Wernsdorfer, W. H. (2007). A review of malaria diagnostic tools: microscopy and rapid diagnostic test (RDT). *The American Journal of Tropical Medicine and Hygiene*, *77*(6_Suppl), 119-127.

Zhu, H., Sencan, I., Wong, J., Dimitrov, S., Tseng, D., Nagashima, K. & Ozcan, A. (2013). Cost-effective and rapid blood analysis on a cell-phone. *Lab on a Chip*, *13*(7), 1282-1288.

Chapter 5

A THREE TIER PRE-PROCESSING VALIDATION FOR IMAGE SEGMENTATION AND ANALYSIS OF RBCS IN SEM IMAGES

E. Priya*, PhD

Department of Electronics and Communication Engineering,
Sri Sairam Engineering College, Chennai, India

ABSTRACT

Images play a major role in understanding of biological processes. The procedure to extract information regarding the specimen from a microscope image is greatly enhanced by digital image processing. In this work, digital image processing of Red Blood Cells (RBCs) in Scanning Electron Microscopy (SEM) is attempted. The shape-based analysis of RBCs plays an important role in clinical examination of blood cell's diseases and could also help in counting RBCs. The digital image processing of microscopic images involves pre-processing, segmentation and validation. Preparing the image for proper analysis and to arrive at accurate diagnostic inference is more crucial. Thus pre-processing of

---

* Corresponding Author's Email: priya.ece@sairam.edu.in.

these images is attempted by retrospective methods such as Surface Fitting Method (SFM), Multiple Regression Method (MRM) and Bi-dimensional Empirical Mode Decomposition (BEMD). Segmentation of the RBC images is a critical procedure for automatic counting of cells, analysis and classification in clinical diagnosis. The segmented images are validated using similarity, overlap and distance measures. The results of the three tier validation process demonstrate that SFM performs better in preparing the images for further stages. It is observed that active contour-based segmentation has identified most of the contours of the RBCs and performs better than other conventional procedures. It also helps in extracting quantitative information about the SEM RBCs and can transform the image so that the displayed version is much more informative than it would otherwise be. This automated analysis would thus enable shape-based investigation for clinical diagnosis and treatment of blood cell diseases.

Keywords: surface fitting method, regression analysis, bi-dimensional empirical mode decomposition, marker controlled watershed, image gradients, active contour model, similarity metrics

INTRODUCTION

Medical imaging technology has seen progressive advancements in recent decade especially significant growth in computational techniques of medical images (Savkare and Narote, 2015). Computer assisted methods are becoming a valuable tool for interpretation and useful information extraction from biological images especially from microscopic samples. Recent advances in microscopic image acquisition systems and the trend in sophisticated image processing algorithms plays a major role in biomedical research (Rittscher et al., 2008).

Microscopes are extensively used to capture, observe, measure and analyse the images of different living organisms and structures at view fields far below normal human visual perception. Digital imaging has started governing the technology after the genesis of affordable, high-

performance computer and imaging sensor technology. It has replaced traditional film-based photomicrography which is the most widely used method for microscope-based image acquisition, storage and analysis (Wu et al., 2010).

The recent development in computer assisted approaches by building novel image processing algorithms has paved way for advancements in microscopy particularly in cell identification (Gamarra et al., 2017). There are imaging modalities in microscopic techniques where the image becomes suitable for viewing only after processing of the digital images. Thus digital processing of microscope images has opened up new realms of medical research and brought about the possibility of advanced clinical diagnostic procedures (Wu et al., 2010).

Qualitative and quantitative characterisation of cell images is vital for clinical applications especially in diagnosis and treatment of disease. Human expert-based classification of these images is tedious, elaborate procedure and time consuming. Pattern identification and machine learning techniques alleviate these issues as they have the potential to objectively and effectively analyse (Gamarra et al., 2017).

The analysis of blood cells has gained more importance in the field of biomedical engineering. Procedure involving human for manual testing and analysis may lead to errors. Method involving digital image processing, a software-based approach is a cost effective and an efficient alternative in recognizing and analyzing blood cells (Bhamare and Patil, 2013). This helps in identifying different blood component so as to detect the parasites present in blood cells. Human blood includes various types of cells such as white blood cell, Red Blood Cells (RBCs), platelets, tissue specific cells and various combinations of them (Savkare and Narote, 2015; Shirazi et al., 2015).

RBCs impart red colour to the blood and are the most common type of blood cells which are responsible for the emancipation of oxygen to all body tissues. The deficiency or the abnormality in them may lead to stroke, anemia and other fatal diseases. Manual techniques prevail for the diagnosis of blood cell's diseases till now and the accuracy of them

depends on the expert's decision. Even though number of efforts are made for accurate blood cells image identification and characterization, still a unique workflow is difficult due to the complexity of overlapping objects and shapes in microscopic images of blood cells. Thus computer-based tools are becoming popular for the quantitative analysis of blood samples to help experts in diagnoses of blood cells disorder. The prime and foremost step of the blood cells image analysis is the image pre-processing where unwanted noise is removed from the image (Shirazi et al., 2015). This makes the image suitable for further analysis so that a concise conclusion can be arrived at the earliest.

Pre-processing is the basic step that is performed to improve the image quality so that the contrast of foreground objects are improved and highlighted against the background (Bhamare and Patil, 2013; Wollmann et al., 2017). The quality of images that are acquired from microscopes may suffer from various types of noises including camera lens, exposure time, aging filament, temperature of light source, contaminated aperture and faulty reference voltages. Thus the illumination is not homogeneous most often throughout the view field and thus a bright smudge is seen in the middle of the field (Shirazi et al., 2015; Tasdizen et al., 2005; Lumb et al., 2015; Priya et al., 2014).

Several authors have reported to resolve the illumination issue using image enhancement techniques as a pre-processing step. Local and adaptive histogram equalization has been used for contrast enhancement of parasites and RBCs in Scanning Electron Microscopy (SEM) images. Pre-defined illumination factor has been attempted for illumination correction. The issues relevant to the discernible of features are rectified by paraboloid modal. Method such as rolling ball background subtraction has been reported in the literature to remove the image gradient in the background (Shirazi et al., 2015; Wollmann et al., 2017).

The next step in identifying foreground objects from background is the image segmentation. Image segmentation and pattern recognition techniques are essential procedures in computer-aided diagnosis, and

have revealed great deal of clinical applications (Savkare and Narote, 2015). Segmentation partitions the input image into its constituent parts or objects and distinguishes between regions. The segmentation step brings the process a long way towards successful solution of an imaging problem if necessary conditions in identifying the objects are not satisfied. Segmentation still remains a challenging task in the field of biomedicine because of complex nature of the image so as to segment objects from its background (Bhamare and Patil, 2015; Maitra et al., 2012).

The segmentation stage aids in extracting features from the segmented blood cells and discriminates normal from the infected ones. The traditional procedure of blood cell analysis is tedious and time consuming as it is subjected to manual analysis involving human intervention. It is a challenging task to analyze them manually because of complex cell structure and overlapping between the cell regions and background. The result of manual process is subjective as it depends on the expertise of the technician (Shirazi et al., 2015).

The automated procedure such as pattern recognition techniques are used to analyse different cells by means of microscopic images. Analysing these cells is very helpful in diagnosis of various fatal diseases. The automated methods are flexible and felicitate precise results as compared to the conventional manual procedures. However, even now image segmentation of overlapping cells and complex shapes is challenging task for accurate blood cell analysis (Shirazi et al., 2015).

Several state-of-the-art techniques have been proposed in the literature relevant to image segmentation. But analysis on microscopic image segmentation is rarely reported in the literature. Precise segmentation of blood cell images is crucial in preserving the shape, identification of disease and in enumeration of cells. Various methods for segmentation and classification of blood cells are reported in literature but have some limited application. Traditionally used approaches include region growing, watershed segmentation and thresholding approach such as Otsu, histogram-based thresholding. But

all of these methods experience inconsistencies especially when there are significant irregularities in the images (Shirazi et al., 2015).

The broad categories of image segmentation include edge or contour-based and region-based techniques. Some of the region-based segmentation methods implemented for blood cell demarcation are morphological operators, watershed segmentation approaches, edge-based hue saturation intensity model and colour space-based segmentation using the G channel from RGB colour coordinates. Techniques such as fuzzy c-means clustering are used to segment the cell constituents in the blood cell images. More accurate segmentation results from methods similar to parametric deformable model, Hough transform techniques and normalized cut (Gamarra et al., 2017; Bhamarre and Patil, 2013; Wang and Fang, 2012).

However in the presence of overlapping objects, the automation of cell segmentation is not a simple task. The segmentation of blood cell is challenging because of varied reasons. The cells in these images have low contrast with variation in shapes. In some cases the boundaries of cells are missing and vague which make the segmentation more obscure (Shirazi et al., 2015).

The performance of segmentation methods has a direct impact on the detection, identification and target description, as well as in monitoring of disease progression. Statistical-based validation analysis is attempted against the binary segmented results with that of the gold standard derived from expert's manual segmentation. Apart from these methods, information theory, probabilistic, pair counting, volumetric, voxel-based expectation-maximization algorithms and receiver operating characteristics curves are implemented for proving the relevancy of segmentation (Zou et al., 2004; Taha and Hanbury, 2015; Warfield et al., 2002; Zou et al., 2004).

The performance of the segmentation procedure is evaluated by performance metrics so as to develop an automated system for the analysis of blood cell images. The spatial overlap-based metrics

specifically true positive, false positive, true negative and false negative are used for evaluation (TarasKotyk et al., 2016).

The quality of measure that is implemented to compare segmented and ground truth is the correctness of segmentation. The correctness gives the measure of error introduced by automatic segmentation method (de Graaf et al., 1992).

Correlation of numerical methods in comparison of ground truth with algorithm segmentation is implemented in three groups such as volumetric, overlap and geometric measures (Frounchi et al., 2011).

Useful features are required to be found from the delineated objects after the segmentation stage to identify the constituents of blood cell images. The extraction of feature results in quantitative information that differentiates the class of one cell from other. Quite different ranges of feature sets are used in cell identification which include, texture, shape and colour features. Texture features are derived from gray level co-occurrence matrix. colour histogram, colour features, mean, standard deviation from International Commission on Illumination Standardization colour space (Bhamare and Patil, 2013).

The shape-based feature extraction of red blood cells provides more valuable information, since it assists in accurate diagnosis of the disease which cannot be expected from intensity or a colour image. In cell-based diagnosis, geometrical features aid the hematologists or pathologist to make a decision based on the number of cell count (Shirazi et al., 2015; Wang and Fang, 2012).

Literature reveals that geometric features including size, perimeter, circularity, compactness, area of cell and intensity features including minimum, maximum, and mean intensity can pretty well identify the cells. Based on the extracted features, undesired segmented cells with certain properties out of range such as too dim, too small, too big can be excluded from further analysis (Bhamare and Patil, 2013; Wollmann et al., 2017).

In this chapter the RBC SEM images are pre-processed so that the image details are demarcated by the active contour segmentation procedure. The segmented results are validated by similarity, overlap and distance measures. Relevant geometric shape-based features are derived from the segmented binary image for identification of the RBCs.

METHODOLOGY

SEM RBC Image

The microscopic image analysis is elaborated in this chapter by considering a typical SEM image of RBC. The horizontal and vertical resolution of the image is of 200 dpi each. The original image is of size 1240×904 pixels and has grid lines which are included for the purpose of enumeration. To avoid grid lines a typical portion of size 291×299 pixels is cropped from the original image for further analysis.

Steps to Image Analysis

Analyses of microscopic images need to be automated to retrieve qualitative and quantitative information from the cells (Wollmann et al., 2017). An automated image analysis workflow is discussed in this chapter for characterisation of RBCs in SEM images. The workflow consists of image acquisition, pre-processing, segmentation and feature extraction. The schematic workflow is shown in Figure 1, where the pre-processing stage improves the image quality and enhances meaningful information by reducing noise. The segmentation and
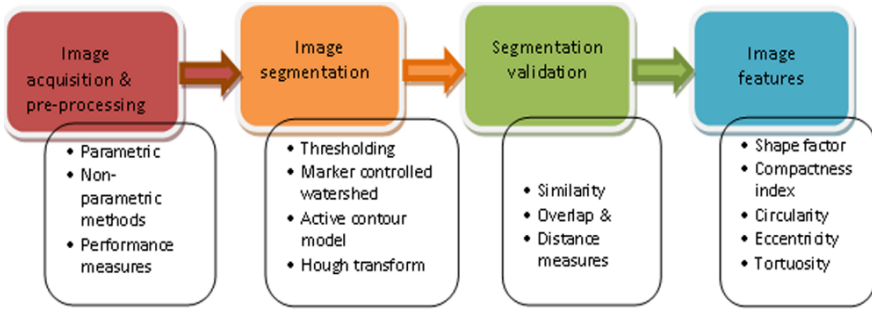
Figure 1. Typical pipeline of the workflow.

feature extraction help in object identification, pattern recognition and classification.

Illumination variations in the blood cell images may lead to biased analysis as they degrade the efficiency of both the manual and automated system. Therefore, image pre-processing is required to minimize these variations which facilitates the image segmentation and also improves the accuracy of identification and classification (Shirazi et al., 2015).

Sources of Errors in Microscopic Imaging

Microscope has unique mechanical and optical properties leading to inhomogeneous illumination (Tomori et al., 2009). The sources of errors are microscopic optics, vignetting, out of focus, field diaphragm, dust, faulty reference voltages, aging filaments, spherical aberration, contaminated aperture, uneven sample preparation and non-uniform illumination. The background illumination intensity is most often not homogeneous throughout the view field, so a bright spot is visualized in the middle of the field (Tasdizen et al., 2005; Lumb et al., 2015).

Illumination Correction Methods

The prevailing illumination correction methods are broadly classified into two category namely prospective and retrospective methods.

Prospective Methods

Prospective methods use special hardware or specific sequences to avoid non-uniform illumination in the acquisition process.

Retrospective Methods

Retrospective methods rely mostly on the image data and thus can be applied to remove the non-uniform illumination. In this chapter, non-uniform illumination in SEM RBCs images is corrected by retrospective methods. Methods such as Surface Fitting Method (SFM), Multiple Regression Method (MRM), Bi-dimensional Empirical Mode Decomposition (BEMD) are attempted to remove non-uniform illumination in these images. The intensity variation in the microscopic imaging can be described by the following model:

$$I(x, y) = I_l(x, y) \cdot a(x, y) + offset(x, y) \tag{1}$$

where $I(x, y)$ is the final digital image recorded from the digital camera mounted on the microscope and (x, y) represents the spatial coordinates. The effect of the camera offset is represented as $offset(x, y)$. The image $I(x, y)$ is produced by the interaction of

microscope illumination $I_l(x, y)$ with the specimen $a(x, y)$ (Wu et al., 2010).

Surface Fitting Method

The second order polynomial function used in this work to fit the background is represented as

$$z(i, j) = Ax(i, j)^2 + Bx(i, j)y(i, j) + Cy(i, j)^2 + Dx(i, j) + Ey(i, j) + F$$

(2)

where (i, j) represent the sample points of mesh grid, x and y the arrays of the mesh grid. The polynomial surface is initially fitted to the whole image $I(x, y)$ and is subtracted from the original image to get the estimate of the background compensated image. This procedure is iterated until the average change in pixel value between two successively calculated backgrounds is less than half the original quantization step of the image (Wahlby et al., 2002).

Multiple Regression Method

This method is a statistical technique in linear regression model for multivariate case and is represented by

$$[Y] = [X][\beta] + [e]$$

(3)

where Y is the response vector, X the input matrix, β the regression coefficient and e the random error vector. The new intensity value of the location is calculated after estimating the parameter β which

represents the best fit intensity plane of the image. This best fit intensity plane represents the estimated background. Thus the illumination corrected image is derived by subtracting the best fit intensity plane from the original image. This procedure is iterated until minimum difference between the successive estimated backgrounds is reached. This method only considers the correction using illumination density plane in one direction, which is much more restricted and not robust (Ko et al., 2002; Guo et al., 2005; Kahraman and Stegmann, 2006).

Bi-Dimensional Empirical Mode Decomposition

This method decomposes a given image into finite number of two dimensional intrinsic mode function based on the local frequency or oscillation information. It then selectively reconstructs the original image $I(x, y)$, by adding IMFs with the nth residue ignoring the IMFs whose contributions to the image are undesirable and is represented as

$$I(x, y) = \sum_{i=1}^{n} imf_1(x, y) + R_n(x, y) \qquad (4)$$

Selective combination of IMFs that do not contain illumination effects, thus enable to reconstruct the image without the unwanted effects of illumination variation (Bhagavatula and Savvides, 2007; Yuehui and Minghui, 2008).

Performance Measures

The illumination correction techniques employed are evaluated qualitatively and quantitatively. A three tier validation procedure is

followed to find the best pre-processing method for SEM RBC images. The systematic three tier validation procedure is presented in Figure 2.

The first tier includes the qualitative method which is carried out by plotting the intensity profile along a row of pixels in the original and corrected images. The second tier comprises of quantitative method based on histogram features. The third tier yet again a quantitative method includes the image quality measures. This computes error and statistical measure to quantify the sharpness of the image. The RBC cells in the illumination corrected images are thus identified by segmentation procedure followed by relevant feature extraction.
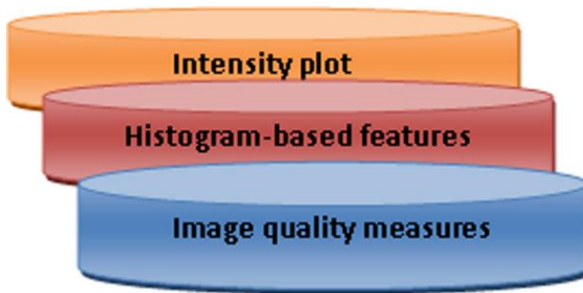
Figure 2. The three tier pre-processing validation.

Segmentation

Separating the contents of an image into regions of interest that is into foreground and background objects is called segmentation. This stage is a prime and crucial stage as further analysis and information extraction depend on the result of segmentation. Segmentation is one of the challenging problems in image analysis and more work has been focused especially in trying to segment various types of cells present in biological images (Vromen and McCane, 2009; Sintorn, 2005). If image segmentation is done properly then it would result in accurate processing of subsequent stages. Also the performance of segmentation

methods has a direct impact on the detection and monitoring of disease progression (Shirazi et al., 2015; Zou et al., 2004; Below, 2012).

Segmentation Techniques

Two main segmentation approaches apart from the basic thresholding technique are region and edge-based technique. RBCs in blood cell images are semi-transparent and hence their boundaries for overlapping cells are difficult to identify (Vromen and McCane, 2009).

Since the images are corrected for illumination, the image gradients are stronger and thus more focus is done based on edge-based techniques than region-based ones. Commonly used edge-based methods include model fitting, deformable templates, active contours or level sets, and a combination of level sets and watersheds (Vromen and McCane, 2009).

Thresholding

Thresholding is a simple segmentation method useful in cases where regions of interest can be identified as image elements having similar gray-levels and at the same time remaining image elements have different gray-levels. To find one (or more) suitable threshold values, it is often useful to study the gray-level histogram of the image (Sintorn, 2005). Any point (x, y) in the image at which $f(x, y) > T$ is called an object point, otherwise the point is called a background point. The segmented image $g(x, y)$ is given by

$$g(x, y) = \begin{cases} 1 \ \text{if} \ f(x, y) > T \\ 0 \ \text{if} \ f(x, y) \leq T \end{cases} \tag{5}$$

where T is called as threshold, can be fixed as a constant for both local or global to the image.

Thresholding is the basic and most widely used automated image segmentation method. This method assigns label of background to every pixel in the image whose value falls below a chosen threshold, while the label of foreground is assigned to each pixel that matches or exceeds the value of the threshold. Latest thresholding methods choose the threshold value adaptively by computing global or even local image histograms. But thresholding methods cannot be used alone in microscope images as they contain noise and are not illuminated uniformly. Thus these methods are used only as an initialization to other segmentation ones (Rittscher et al., 2008).

However, thresholding method tends to show good results only on uniform images and do not produce consistent results.

Marker Controlled Watershed

The watershed segmentation is an intuitive method that produces a complete division of the image in separated regions, thus avoiding the need for any kind of joining contours. Here the image is considered as a topographical surface, and "flood" the surface from its local minima by computing the intensity levels. A dam is built when two regions merge and thereby represents an edge or boundary. This method can be applied directly to the raw images or to processed images such as edge-enhanced or distance transformed ones. However it results in over segmentation of images and careful initialization (seeding) must be used (Rittscher et al., 2008).

Marker controlled watershed segmentation is performed to reduce the issue of over segmentation. In this method, the distance transform is used as edge detection for the watershed computation. The foreground markers are computed by performing reconstruction based opening and

closing that are more effective than standard opening and closing. This removes small blemishes without affecting the overall shape of the object. Reconstruction transformations of the marker function g in the image f, using geodesic dilations and erosions, expressed by $R(f,g)$ and $R^*(f,g)$ respectively are defined by

$$R(f,g) = \lim_{n \to \infty} \delta_f^n(g)$$

$$R^*(f,g) = \lim_{n \to \infty} \varepsilon_f^n(g) \tag{6}$$

where $\delta_f^n(g)$ and $\varepsilon_f^n(g)$ are the geodesic dilation and erosion of size n. The marker function g when equal to the erosion or dilation of the original function, the opening $(\tilde{\gamma}_\mu)$ and closing $(\tilde{\varphi}_\mu)$ by reconstruction are obtained as

$$\tilde{\gamma}_\mu(f) = \lim_{n \to \infty} \delta_f^n(\varepsilon_\mu(f))$$

$$\tilde{\varphi}_\mu(f) = \lim_{n \to \infty} \varepsilon_f^n(\delta_\mu(f)) \tag{7}$$

where μ is an homothetic parameter representing the size of the structure. The binary foreground marker can be obtained by calculating the regional maxima of the reconstructed image.

$$RMAX_e(f) = f - HMAX_{1,e}(f) \tag{8}$$

where e denotes the connectivity used and $HMAX$ represents the h-maxima operation with height attribute equal to one, that is, there are no other level components above them (Wu et al., 2010).

Hough Transform

The Hough transform is actually a feature extraction technique in image analysis and computer vision especially in digital image processing. It is initially used as a method to detect lines in edge maps and is later extended to detect general low-parametric objects such as circles and even ellipse.

Hough transform works by splitting the input image into a set of voting elements. Each such element votes for the hypotheses that might have generated this element. The votes from different voting element pixels are added together into a Hough image, with the height of the peak providing the confidence of the detection. The equation for circle detection which is referred as

$$(x-a)^2 + (y-b)^2 = r^2 \tag{9}$$

which contain three unknown (a,b,r) parameters and therefore the accumulator cell should be of three dimensional for three unknown variables (Maitra et al., 2012).

The RBCs in SEM image is approximately elliptical, at least in a global sense, but there are local variations that are often far from elliptical too and this could misinterpret in diagnosing and treating disease stages (Vromen and McCane, 2009).

Active Contour Model

Active contour is otherwise known as a snake and has been proposed as one of the most promising methods for medical image segmentation. The snake algorithm is useful for the segmentation of objects where the edges are not well defined. The snake segmentation technique has a number of attractive characteristics that makes it useful

for shape detection. The snake model can be parameterized contour defined within an image domain. The internal forces within the image domain control the bending characteristics of the line, while forces like image gradient act to push the snake toward image features (Shirazi et al., 2015; Soomro et al., 2018).

Chan-Vese active contour method, unlike other methods uses level set and does not rely on gradient of image.

$$F(c^+, c^-, \phi) = \mu |C(\phi)| + \lambda^+ \int_{\phi \geq 0} |u_0(x, y) - c^+|^2 dxdy + \lambda^- \int_{\phi < 0} |u_0(x, y) - c^-|^2 dxdy$$

(10)

This method identifies by partitioning the input image I into two regions namely, the objects to be detected and the background based on intensity averages (Chang and Vese, 2001).

There are several advantages in formulating level-set of active contour model. The changes in topology of the object boundaries are handled automatically without extra effort. Therefore the technique can easily be extended to three or more dimensions, especially if changes in topology are involved. The drawback of level-set method is that the level-set function ϕ needs to be computed throughout the domain of the image, even though only a contour or sets of contours are desired (Rittscher et al., 2008).

Segmentation Validation with Ground Truth

The accuracy of an individual experimental segmentation is usually given through the measure of a region's overlap and its distance from the ground truth. Distance transforms are used in matching issues because they make distance-based similarity measures more practicable. The overlap measure is characterized by a similarity measure between experimental and ground truth. Cates et al., (2005),

Zhou and Wang (2009) have addressed the mathematical formulations of the similarity, overlap and distance measures.

Image Features

Necessary features are required to be extracted from the segmented images to distinguish between cells, viruses or other micro-organisms. This stage allows to characterize the cells or viruses and thus helpful to perform a posterior classification of the cells. Several types of image features have been attempted in the literature which includes shape-based morphological, co-occurrence matrix, Haralick features, texture, moment invariants such as Hu and Zernike moments features, spectral features, Fourier descriptors and colour features (Priya et al., 2012; Tomita and Tsuji, 1990; Lestrel, 2008; Birgale et al., 2006; Gitelson and Merzlyak, 1994; Gamarra et al., 2017).

The shape-based geometric features are accounted in this chapter as the contour of the RBCs is only interested rather than counting of blood cells in SEM images. Geometric shape descriptors are derived to extract useful characteristics from the segmented images as it is essential for describing the shape of the cells (Hiremath and Bannigidad, 2010). The definition of the features addressed in this chapter is given in Table 1.

Table 1. Definition of geometric shape descriptors

S. No.	Geometric shape descriptors	Definition
1	Shape factor	Ratio of length to width
2	Compactness index	Ratio of square of the perimeter to the area. This index provides a measure that describes the closeness of the shape of the object to that of a circle
3	Circularity	Ratio of the area of a shape to the area of a circle having the same perimeter
4	Eccentricity	Ratio of the length of major axis to the length of minor axis. Eccentricity of ellipse is greater than zero but less than one
5	Tortuosity	Ratio of major axis length to perimeter

RESULTS AND DISCUSSION

The cropped portion of the SEM image is presented in Figure 3 (a). A bright spot is observed in the image which represents the illumination component present in the image. These images are subjected to illumination correction methods such as SFM, MRM and BEMD. The results of these methods are shown in Figure 3 (b)-(d). The low frequency illumination component that is removed as background is visualized in Figure 3 (f) and the corresponding illumination corrected image is shown in Figure 3 (b) for SFM. The background and the illumination corrected image by MRM are presented in Figure 3 (g) and (c). Similarly the IMF1 and the reconstructed image using BEMD is shown in Figure 3 (h) and (d).
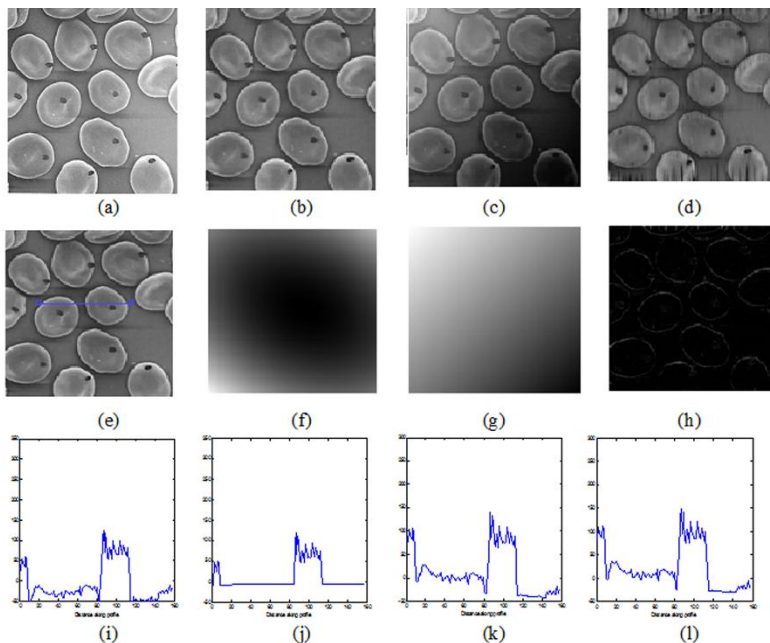
Figure 3. (a) Typical SEM RBC cropped image (b) SFM (c) MRM (d) BEMD corrected images (e) a line drawn on the image to study intensity profile (f)-(h) corresponding background image (i)-(l) intensity profile before and after illumination correction.
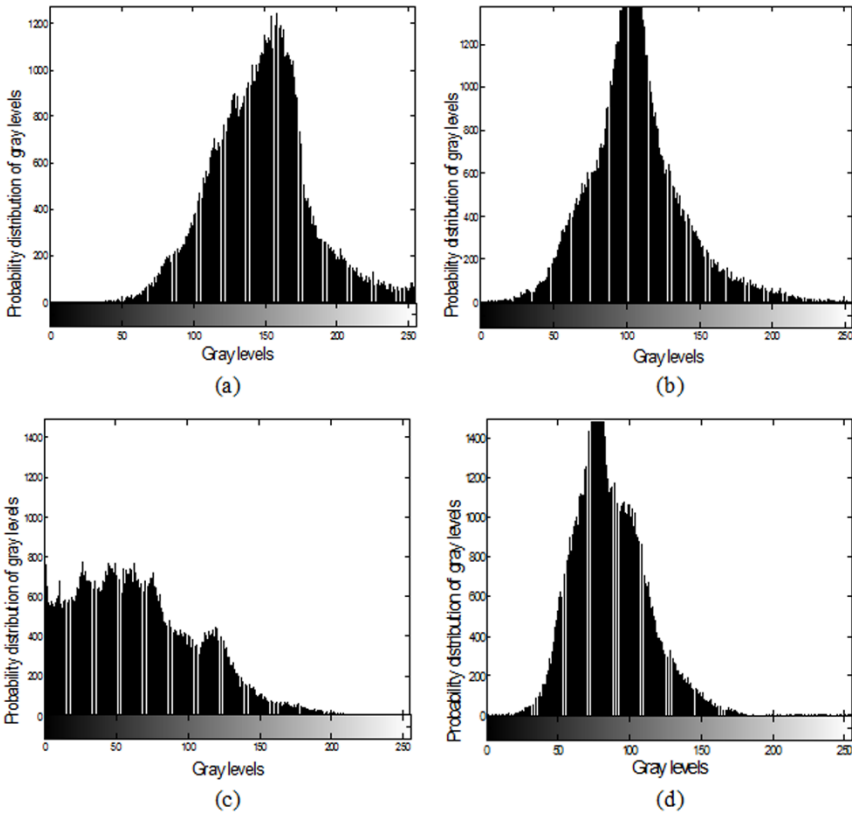
Figure 4. Histogram of SEM RBC image (a) before illumination correction (b) after surface fitting method (c) multiple regression method and (d) bi-dimensional empirical mode decomposition.

As mentioned in the methodology, the first tier validation involves a qualitative procedure. The corrected images are qualitatively analysed by plotting the intensity profile. The intensity profile is plotted along a line drawn in the image as shown in Figure 3 (e). Figure 3 (i)-(l) shows the intensity profile of the RBC image along the line before and after correction by the respective methods. It is observed that the base line wandering effect is observed in the image before correction and the same trend is visualized for the images corrected by MRM and BEMD. The base line wandering effect problem is over ridden in SFM compared to other methods as observed from Figure 3 (j).

The intensity distribution of these images is further studied by plotting the histogram for the images before and after illumination correction. The corresponding histogram plot is presented in Figure 4. The right skewed histogram plot observed in Figure 4 (a) represents the original SEM RBC image with low intensity distribution. This is due to the presence of low frequency illumination component in the image. The skewness of histogram is corrected in the SFM as shown in Figure 4 (b). But the histogram of MRM corrected image is translated to the dark portion of histogram stating that an additional dark patch is visible in the image. This could be due to generalized inverse procedure adopted for calculating the best fit plane using regression in the MRM procedure. The histogram presented in Figure 4 (d) for the BEMD method shows a slight left skewness indicating the improvement in contrast of the image. Few dark lines are also present in the corrected images. In this method, IMF1 is retained and rest of the IMFs corresponding to low frequency intensity components are eliminated manually.
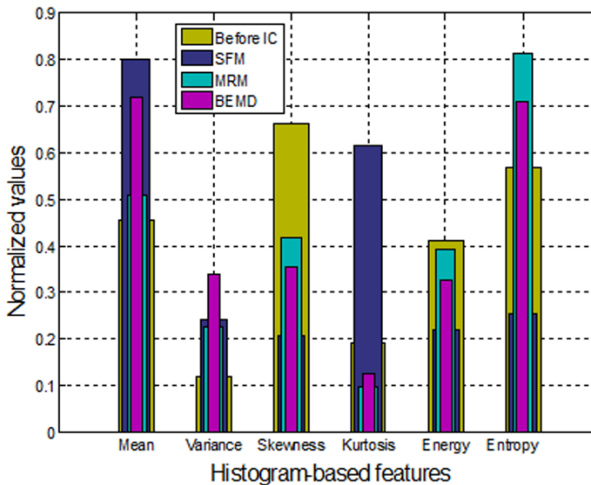
Figure 5. Overlay bar graph of the normalized average values for histogram-based features (*IC-Illumination Correction).

The results are further validated by histogram-based features which are computed from the images before and after correction. This includes the second tier of validation procedure. The overlay bar graph of the normalized average values for histogram features are presented in Figure 5. Since brightness of the image is poor before illumination correction the mean of the histogram is low and is observed to be high for SFM.

Results demonstrate that variance is high for BEMD than other methods and this is because of the increase in image contrast. It is observed from overlay bar graph that skewness is low for SFM because of uniform background intensity values which aid in distinguishing RBCs from background. Since the RBCs visibility and the sharpness around edges are improved, the SFM has high kurtosis than MRM and BEMD. The histogram presented in Figure 5 (a) is skewed due to lower in number of gray level values. Hence energy of the image before illumination correction is found to be high as observed in Figure 5. Since the gray level distribution is uniform and not random, the histogram feature entropy is low for SFM and is high for MRM and BEMD. This is due to the presence of dark patch in MRM corrected image and extraneous pixels in BEMD method.

The third tier of validation is inferred from the image quality measures. The box plot of the normalized average values for image quality measures are plotted in Figure 6. These values are computed for the three illumination correction methods against before correction. The Mean Square Error (MSE) difference is lower for SFM than other methods. Because of this, Peal Signal to Noise Ratio (PSNR) value is high for SFM as the low frequency illumination component is removed. The Least Mean Square Error (LMSE) and Normalized Absolute Error (NAE) measures are observed to be low for SFM. Since dark intensity spot and lines are visible in MRM and BEMD corrected images, the error measures are reported to be high.
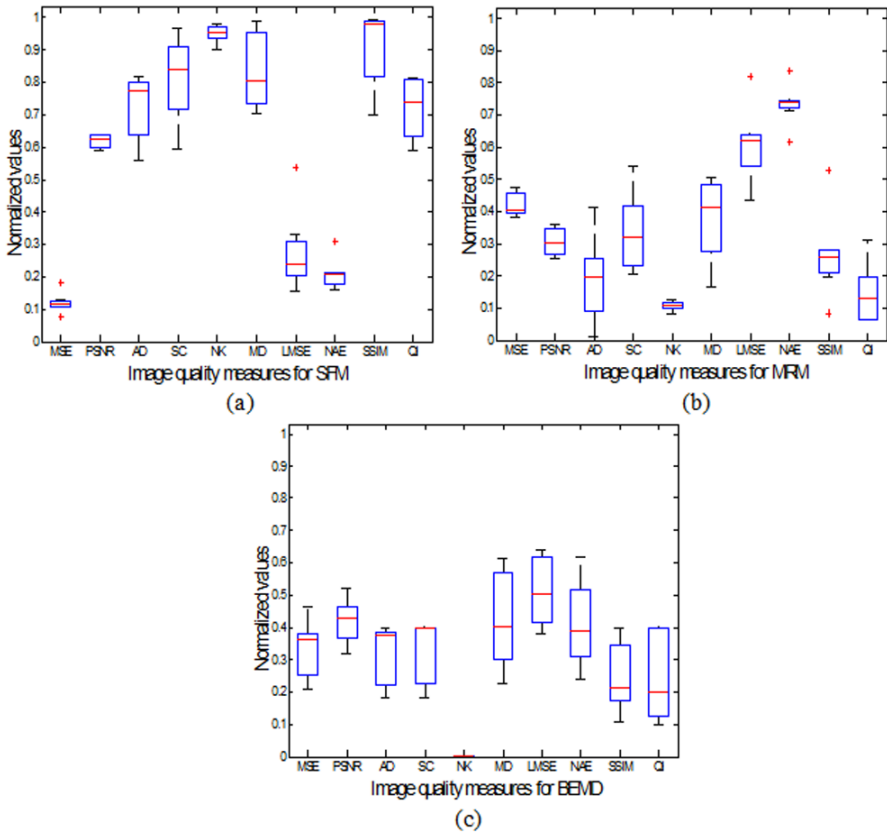
Figure 6. Box plot representing the image quality measures for (a) SFM (b) MRM and (c) BEMD-based method.

It could be inferred from Figure 6 that average and maximum difference is low for MRM and BEMD methods as intensity in pixel difference is more or less same with that of the image before illumination correction than SFM. The image quality for the rest of the four metrics such as Normalized Cross Correlation (NK), Structural Content (SC), Structural Similarity Index (SSIM) and Quality Index (QI) was tested with the ground truth images. High correlation and structural similarity was observed between SFM corrected images and ground truth images. High correlation refers to a value closer to 1, inferring that the images corrected using SFM seems similar to the

ground truth images. The image quality was also tested by considering blocks of pixels and is compared with the ground truth. Results demonstrate that in all the three validation stages SFM performs better in removing the low frequency illumination from the SEM RBC images. The pre-processed images using SFM are segmented to identify the RBCs, so that enumeration could be performed in later stages for proper diagnosis of disease.

The illumination corrected image is segmented so that shape based features are extracted to identify the shape deformity analysis in clinical relevant blood diseases. The result of thresholding, Sobel gradient and watershed is shown in Figure 7 (b), (c) and (d). The edges are not much emphasized in threshold based segmentation and only nine out of seventeen RBCs have been identified by watershed segmentation. To improve the results of watershed segmentation, gradient of the image is derived to be used as marker in marker controlled watershed segmentation. It is observed from Figure 7 (e) that out of seventeen RBCs sixteen are identified, but the background pixels is also wrongly identified as foreground object. Also some foreground pixels is found missing.

Since the RBCs are almost round in shape, Hough circle and ellipse-based segmentation is also attempted. Hough results presented in Figure 7 (f)-(h) are derived by applying Prewitt, Roberts gradient and log transformation as an edge map. It is observed from the results that Hough circle identifies only ten RBCs when Prewitt gradient is used and nine when log transformation is applied. Hough transform missed some of the RBCs which are elliptical in shape, hence to segregate them ellipse Hough transform is attempted. The cells which are in border of the images are not correctly identified as observed from Figure 7 (i). It is found that without prior gradient information of overlapping cells the segmentation result proved to be difficult.
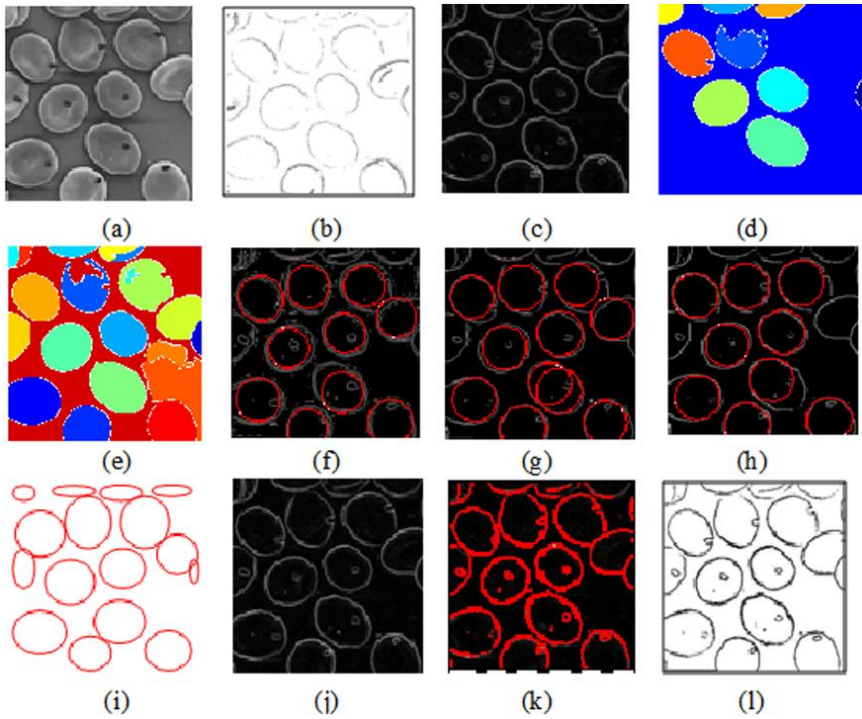
Figure 7. Segmentation results (a) original cropped image (b) thresholding (c) Sobel gradient (d) watershed (e) marker controlled watershed (f)-(h) circle Hough transform for Prewitt and Roberts gradient, log (i) ellipse Hough transform (j) Prewitt gradient magnitude (k) active contour-based boundary (l) active contour segmented binary output.

To alleviate the above said problems, an attempt has been made to implement level set-based active contours to segment the RBCs from SEM images. An edge map using Prewitt gradient magnitude is derived for which active contour splits and evolves until the boundaries of the cells. The edge map, boundary identification and segmented binary output are shown in Figure 7 (j)-(l). The edges of cells are separated from its background and distinguish boundaries are visible for overlapping cells. Results demonstrate that all the cells present in the image has been identified with less noise and redundant search of the edges.
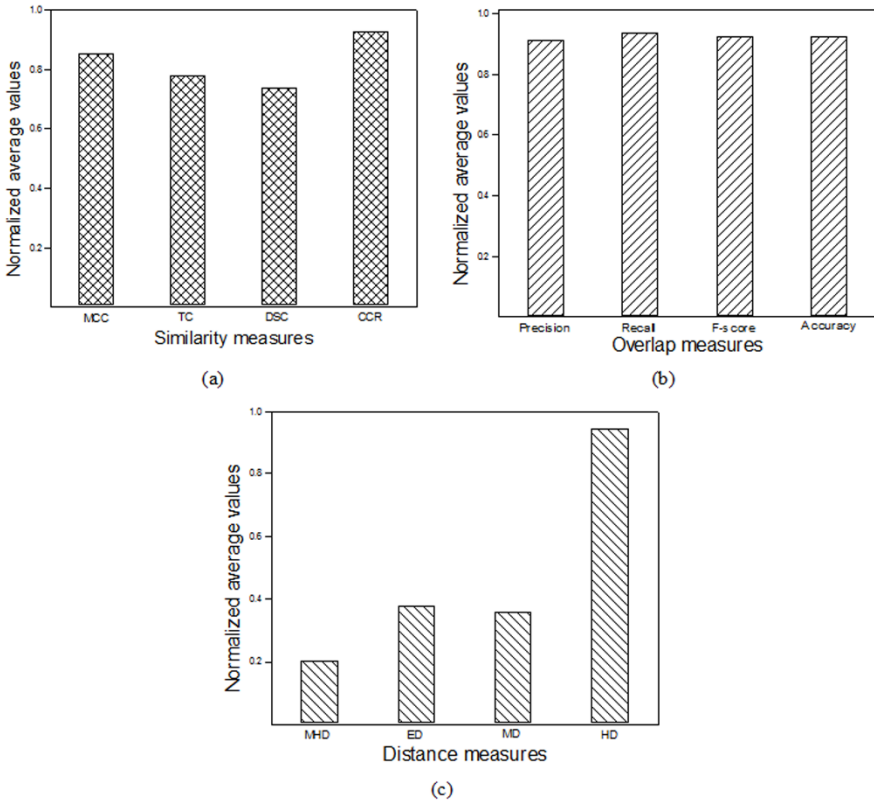
Figure 8. Segmentation validation metrics (a) similarity (b) overlap and (c) distance measures.

Table 2. Average and standard values of ratiometric geometric features

Shape factor	Compactness index	Circularity	Eccentricity	Tortuosity
Mean ± standard deviation				
0.91 ± 0.03	0.84 ± 0.14	0.89 ± 0.22	0.81 ± 0.08	0.45 ± 0.06

The results of the active contour segmented output are validated with ground truth using similarity, overlap and distance measures. The normalised similarity measures presented in Figure 8 (a) are observed to be high. This refers to the existence of similar regions present in both segmented output and the ground truth. The precision and recall

measures presented in Figure 8 (b) indicate the false positive and false negative being low. This pretty well explains that most of the pixels detected by the segmentation method are also present in ground truth. The results of distance measures shown in Figure 8 (c) are low for Modified Hausdorff Distance (MHD), Euclidean Distance (ED) and Minkowski Distance (MD). Hence it is understood that there is a close match between segmented output and ground truth such that the distance between groups of pixels in segmented output is in close proximity with ground truth. The Hamming Distance (HD) value is high compared with others as it presents the total area under intersection between the segmentated and ground truth.

Appropriate features describing the shape of the cells such as geometric shape descriptors are extracted from the segmented images. The normalized average and standard deviation values of the shape descriptors are presented in Table 2. It is observed that almost all the features except tortuosity are nearer to one. This is because the RBCs resembles a biconcave shape and are having a slight elongated circle shape. Since RBCs deprive of curves and bents which are expected in elliptical shape, the tortuosity values are presented to be low.

CONCLUSION

Nowadays the use of computer assisted methods for the analysis and evaluation of microscopic images are inevitable. The pilot task of image processing is to enhance the quality of digital images acquired from the microscopes for further analysis. The image processing techniques help in locating, measuring, identifying, and counting the objects of interest in a microscope field of view (Michler, 2008; Castleman, 1998).

Automated processing of these images is essential for mass screening of diseases rather than manual image analysis carried out by

human experts. There are few processing stages involved in microscopic image analysis. Each stage deals with wide field of research: pre-processing to improve the image quality, segmentation, feature extraction and feature selection, and finally classification (Gamarra et al., 2017).

In this chapter the cell shape characterisation of RBCs in SEM images is studied. The images are pre-processed by retrospective methods such as SFM, MRM and BEMD. A three tier validation process is followed to find the best method to pre-process. These images are segmented by methods involving edge and region-based methods. The segmentation procedure is validated by the ground truth images using similarity, overlap and distance measures. Geometric shape-based features are derived from the segmented images for characterising the shape of the blood cells.

Results demonstrate that SFM method performs better in removing the non-uniform illumination component when compared to MRM and BEMD methods. Further validation of SFM is done by tier 1: intensity profile plot; tier 2: histogram-based features and tier 3: image quality measures. It is observed that active contour-based level-set segmentation procedure has segmented the contour of RBCs with less noise and redundant search. A close match of 80% is observed between the segmented images and ground truth preserving the edges of all the cells. Significant shape-based geometric features characterise the shape of RBCs in SEM images which would aid in diagnosis and continuous monitoring of blood cell disease progression.

REFERENCES

Below, A. A. L. (2012). Guide to medical image analysis methods and algorithms. *Advances in Computer Vision and Pattern Recognition.*

Bhagavatula, R., & Savvides, M. (2007, April). Analyzing facial images using empirical mode decomposition for illumination artifact removal and improved face recognition. In *Acoustics, Speech and Signal Processing, 2007. ICASSP 2007. IEEE International Conference on* (Vol. 1, pp. I-505). IEEE.

Bhamare, M. G., & Patil, D. S. (2013). Automatic blood cell analysis by using digital image processing: a preliminary study. *Int. J. Eng. Res. Tech*, *2*(9), 3135-3141.

Birgale, L., Kokare, M., & Doye, D. (2006, July). Colour and texture features for content based image retrieval. In *Null* (pp. 146-149). IEEE.

Castleman, K. R. (1998). Concepts in imaging and microscopy: color image processing for microscopy. *The Biological Bulletin*, *194*(2), 100-107.

Cates, J. E., Whitaker, R. T., & Jones, G. M. (2005). Case study: an evaluation of user-assisted hierarchical watershed segmentation. *Medical Image Analysis*, *9*(6), 566-578.

Chan, T. F., & Vese, L. A. (2001). Active contours without edges. *IEEE Transactions on Image Processing*, *10*(2), 266-277.

de Graaf, C. N., Koster, A. S., Vincken, K. L., & Viergever, M. A. (1992, June). A methodology for the validation of image segmentation methods. In *Proceedings Fifth Annual IEEE Symposium on Computer-Based Medical Systems* (pp. 17-24). IEEE.

Frounchi, K., Briand, L. C., Grady, L., Labiche, Y., & Subramanyan, R. (2011). Automating image segmentation verification and validation by learning test oracles. *Information and Software Technology*, *53*(12), 1337-1348.

Gamarra, M., Zurek, E., San-Juan, H., Eng, S., & Norte, U. (2017). A study of image analysis algorithms for segmentation, feature extraction and classification of cells. *Journal of Information Systems Engineering & Management*, *2*(4), 20.

Gitelson, A., & Merzlyak, M. N. (1994). Spectral reflectance changes associated with autumn senescence of Aesculushippocastanum L. and Acer platanoides L. leaves. Spectral features and relation to chlorophyll estimation. *Journal of Plant Physiology*, *143*(3), 286-292.

Guo, Y., Zhang, X., Zhan, H., & Song, J. (2005). A novel illumination normalization method for face recognition. In *Advances in Biometric Person Authentication* (pp. 23-30). Springer, Berlin, Heidelberg.

Haralick, R. M., Shanmugam, K., & Dinstein, I. H. (1973). Textural features for image classification. *IEEE Transactions on Systems, Man, and Cybernetics*, *3*(6), 610-621.

Hiremath, P. S., & Bannigidad, P. (2010). Automatic identification and classification of bacilli bacterial cell growth phases. *IJCA Special Issue on Recent Trends in Image Processing and Pattern Recognition*, *1*, 48-52.

Kahraman, F., & Stegmann, M. B. (2006, June). Towards illumination-invariant localization of faces using active appearance models. In *Signal Processing Symposium* (pp. 102-105).

Ko, J., Kim, E., & Byun, H. (2002, August). Illumination normalized face image for face recognition. In *Joint IAPR International Workshops on Statistical Techniques in Pattern Recognition (SPR) and Structural and Syntactic Pattern Recognition (SSPR)* (pp. 654-661). Springer, Berlin, Heidelberg.

Lestrel, P. E. (Ed.). (2008). *Fourier descriptors and their applications in biology*. Cambridge University Press.

Lumb, R., Van Deun, A., Bastian, I., & Fitzgerald, M. (2015). *Laboratory diagnosis of tuberculosis by sputum microscopy—the handbook global*.

Maitra, M., Gupta, R. K., & Mukherjee, M. (2012). Detection and counting of red blood cells in blood cell images using Hough transform. *International Journal of Computer Applications*, *53*(16).

Michler, G. H. (2008). *Electron microscopy of polymers*. Springer Science & Business Media.

Priya, E., Srinivasan, S., & Ramakrishnan, S. (2012, November). Classification of tuberculosis digital images using hybrid evolutionary extreme learning machines. In *International Conference on Computational Collective Intelligence* (pp. 268-277). Springer, Berlin, Heidelberg.

Priya, E., Srinivasan, S., & Ramakrishnan, S. (2014). Retrospective Non-Uniform Illumination Correction Techniques in Images of Tuberculosis. *Microscopy and Microanalysis*, *20*(5), 1382-1391.

Rittscher, J., Machiraju, R., & Wong, S. T. (2008). *Microscopic image analysis for life science applications*. Artech House.

Savkare, S. S., & Narote, S. P. (2015, December). Blood cell segmentation from microscopic blood images. In *Information Processing (ICIP), 2015 International Conference on* (pp. 502-505). IEEE.

Shirazi, S. H., Umar, A. I., Haq, N. U., Naz, S., & Razzak, M. I. (2015, April). Accurate microscopic red blood cell image enhancement and segmentation. In *International Conference on Bioinformatics and Biomedical Engineering* (pp. 183-192). Springer, Cham.

Sintorn, I. (2005). *Segmentation methods and shape descriptions in digital images: Applications in two-dimensional and three-dimensional microscopy*.

Soomro, S., Munir, A., & Choi, K. N. (2018). Hybrid two-stage active contour method with region and edge information for intensity inhomogeneous image segmentation. *PloS one*, *13*(1), e0191827.

Taha, A. A., & Hanbury, A. (2015). Metrics for evaluating 3D medical image segmentation: analysis, selection, and tool. *BMC Medical Imaging*, *15*(1), 29.

TarasKotyk, N. D., Ashour, A. S., Victoria, A. D. C., Gaber, T., Hassanien, A. E., & Snasel, V. (2016). Detection of Dead stained microscopic cells based on Color Intensity and Contrast. In: Gaber T., Hassanien A., El-Bendary N., Dey N. (eds) *The 1st International*

Conference on Advanced Intelligent System and Informatics (AISI2015), November 28-30, 2015, BeniSuef, Egypt. Advances in Intelligent Systems and Computing, vol 407. Springer, Cham.

Tasdizen, T., Whitaker, R., Marc, R., & Jones, B. (2005). *Automatic correction of non-uniform illumination in transmission electron microscopy images*. Scientific Computing and Imaging Institute, University of Utah.

Tomita, F., & Tsuji, S. (1990). Statistical Texture Analysis. In *Computer Analysis of Visual Textures* (pp. 13-36). Springer, Boston, MA.

Tomori, Z., Capek, M., Michalek, J., & Kubinova, L. (2009). Compensation of illumination inhomogeneities in multi-resolution image acquisition in confocal microscopy. In: *19th International Conference on Computer Graphics and Vision GraphiCon '2009*, Moscow, Russia.

Vromen, J., & McCane, B. (2009, November). Red blood cell segmentation from SEM images. In *Image and Vision Computing New Zealand, 2009. IVCNZ'09. 24th International Conference* (pp. 44-49). IEEE.

Wählby, C., Lindblad, J., Vondrus, M., Bengtsson, E., & Björkesten, L. (2002). Algorithms for cytoplasm segmentation of fluorescence labelled cells. *Analytical Cellular Pathology*, *24*(2-3), 101-111.

Wang, R., & Fang, B. (2012). A combined approach on RBC image segmentation through shape feature extraction. *Mathematical Problems in Engineering*, *2012*.

Warfield, S. K., Zou, K. H., & Wells, W. M. (2002, September). Validation of image segmentation and expert quality with an expectation-maximization algorithm. In *International Conference on Medical Image Computing and Computer-Assisted Intervention* (pp. 298-306). Springer, Berlin, Heidelberg.

Wollmann, T., Erfle, H., Eils, R., Rohr, K., & Gunkel, M. (2017). Workflows for microscopy image analysis and cellular phenotyping. *Journal of Biotechnology*, *261*, 70-75.

Wu, Q., Merchant, F., & Castleman, K. (2010). *Microscope image processing*. Elsevier.

Yuehui, S., & Minghui, D. (2008, November). Robust face recognition for illumination removal using DT-CWT and EMD. In *Communication Systems, 2008. ICCS 2008. 11th IEEE Singapore International Conference on* (pp. 357-361). IEEE.

Zhou, Z. Q., & Wang, B. (2009, April). A modified Hausdorff distance using edge gradient for robust object matching. In *Image Analysis and Signal Processing, 2009. IASP 2009. International Conference on* (pp. 250-254). IEEE.

Zou, K. H., Warfield, S. K., Bharatha, A., Tempany, C. M., Kaus, M. R., Haker, S. J., ... & Kikinis, R. (2004). Statistical validation of image segmentation quality based on a spatial overlap index1: scientific reports. *Academic Radiology*, *11*(2), 178-189.

Zou, K. H., Wells III, W. M., Kikinis, R., & Warfield, S. K. (2004). Three validation metrics for automated probabilistic image segmentation of brain tumours. *Statistics in Medicine*, *23*(8), 1259-1282.

Chapter 6

THE INFLUENCE OF NANO POWDER ADDITION AND EMULSIFICATION TECHNIQUE ON ENGINE'S BEHAVIOUR OF A WASTE COOKING OIL BASED DIESEL ENGINE

M. Senthilkumar[*]

Department of Automobile Engineering,
MIT Campus, Anna University, Chennai, India

ABSTRACT

The influence of emulsification and nano powder addition on the performance and emission characteristics of a compression ignition engine operating on a waste cooking oil (WCO) of sunflower oil, was studied experimentally. Initially, the neat diesel (ND) and neat waste cooking oil (NWCO) were used as fuels to operate the test engine in

---

[*] Corresponding Author's Email:mskiitm@yahoo.com.

single fuel mode at different loading conditions. In the second phase, WCO was transformed into its emulsion (WCO-EM) and was used to test the engine. The WCO emulsion was further converted into a solid nano additive emulsion (WCO-NF-EM) and testing was performed. Experimental investigations revealed that NWCO resulted in inferior engine operation with higher smoke, HC and CO emissions when compared to ND at all power outputs. Emulsification and nanofluids addition lead to substantial enhancement in BTE. Further, there was a significant decrease in smoke and NOx emissions, with all the methods. Also,HC and CO emissions were further reduced by WCO-EM and WCO-NF-EM, at all the power outputs. Results demonstrate that WCO can be used efficiently in diesel engines by converting into its solid nano additive emulsion in the un modified engine with the engine operation comparable to diesel based engine.

INTRODUCTION

Vegetable oils show most promising alternative fuel for diesel engine due to their favourable properties very close to diesel fuel (Knežević et al., 2015; Tomić et al. 2013).Earlier studies have reported significant engine results with different vegetable oils as fuels (Hemanandh & Narayanan, 2015; Monirul et al., 2017; Corsini et al. 2015). However, the use of edible oils directly affects the consumer in cost and availability when used as engine fuel. In this regard used cooking oil as fuel, appears to be very attractive for diesel engines. Past engine studies revealed that WCO could be used in diesel engines as fuel (da Silva et al., 2017; Corsini et al., 2016). However international standards prevent the straight usage of such oils in an unmodified diesel engine. WCO could be utilized as fuel in diesel engines effectively with slight modifications either in fuel or in engine side. Transesterification is one of the widely used fuel modifications for converting neat WCO into its ester (Hwang et al., 2016; Qu et al., 2016). This process has the

advantages of reduced viscosity, improved cetane number as compared to its neat oil. But complexity and cost factor make the transesterfication process as an unfavourable method. Emulsification process shows another option in utilizing WCO effectively as diesel engine fuel (Kumar & Jaikumar, 2014; Bora et al., 2016). Earlier research studies reported simultaneous decrease of oxides of nitrogen and smoke emissions in diesel engines emulsified vegetable oils as fuel (Kumar & Jaikumar, 2014; Bora et al., 2016). Hence modifying the WCO into its stable emulsion and using as fuel can achieve reduced smoke and NOx emissions andsuperior thermal efficiency. Recent studies indicated involvement in nanotechnology in improving the engines performance using nano fluids as fuels and promising result outcomes were reported in recent times (Saxena et al., 2017, Mirzajanzadeh et al., 2015; Chandrasekaran et al., 2016). Nano fluids are the fluids dispersed with nano particle in the homogeneous liquids. Nano fluids find a wide range of applications in engine propulsion system, engine cooling system etc. due to its high thermal conductivity. Nano fluids are also used as fuel additives to enhance combustion behaviour of hydrocarbon fuels in engines. Researchers reported that the oxidation of metal content of nano fluid tends to produce more heat as compared to diesel and other fuel when used as an additive along with them. Experiments conducted with four different nano catalysts such as Cerium, Iridium, Palladium and Rhodium in a diesel engine resulted in improved emission and combustion characteristics of biodiesel blend (Saxena et al., 2017). It is clear from the above studies that emulsifying the oil is a simple and efficient method of utilizing vegetable oils as fuel in compression ignition engines. However, past research indicated no results on the influence of nano additives with vegetable oil emulsions as fuel on engines behaviour of diesel engines. Adding solid nano additives with the emulsions and using them as fuel could achieve significant decrease in all the emissions and also an improvement in engines performance. Hence, an attempt was made to utilize WCO effectively in a compression ignition engine. In the first

phase the engine was tested for its performance using neat WCO as fuel followed by WCO emulsion. In the second phase solid nano powder (Al_2O_3) was mixed with WCO emulsion by using an ultrasonic agitator and tested as fuel under variable load conditions. All the methods were compared at 20%,40%,60%, 80% and 100% power outputs.

FUEL PREPARATION AND PROPERTIES STUDY

For the engine trials WCO of sunflower was procured form the institute hostel for about 25 litres. Collected WCO was filtered with course and fine filters and properties such as density, viscosity, etc. were measured. The measured properties are presented in Table1.

Table 1. Properties of fuels

Properties	ND	NWCO	WCO-EM	WCO- NF-EM
Viscosity (cst)	4.6	45	49	44
Density (Kg/m^3)	840	886	895	880
Calorific value (kJ/kg)	43500	40000	38000	41000
Cetane number	45	37	42	44

(ND – Neat Diesel, NWCO – Neat Waste Cooking Oil, WCO-EM – Waste Cooking Oil Emulsion, WCO–NF–EM- Waste Cooking oil solid Nano additive Emulsion).

WCO EMULSION PREPARATION

In general, emulsions are obtained by mixing two different immiscible liquids in the presence of a stabilizer known as a surfactant. The water gets mixed well with oil due to the surfactant. The interfacial tension of the oil is reduced by the surfactant and it permits the water droplets to spread uniformly in the continuous oil phase. A suitable surfactant must be selected since it affects the type of emulsion

formation and its stability. For the present work, surfactant having HLB value less than 7 has to be used for preparing water in oil emulsion. Hence, SPAN 80 (with HLB value as 4.2) was selected as the best surfactant aimed at making water WCO emulsion. The WCO emulsions were prepared by using a mechanical agitator which rotated at the speed of 2000 rpm. Initially a number of trials were made with different combinations of water, oil, surfactant and co surfactant. Ternary diagram shown in Figure 1 was plotted to study the stability of the prepared emulsions. From the stability point the mixture of 75% of WCO, 15% of water, 5% of SPAN 80 and 5% ethanol by volume resulted in maximum stability for 10 days. Hence the above combination was selected for engine tests. The same was used for preparing the WCO emulsion with solid nano additive as well.
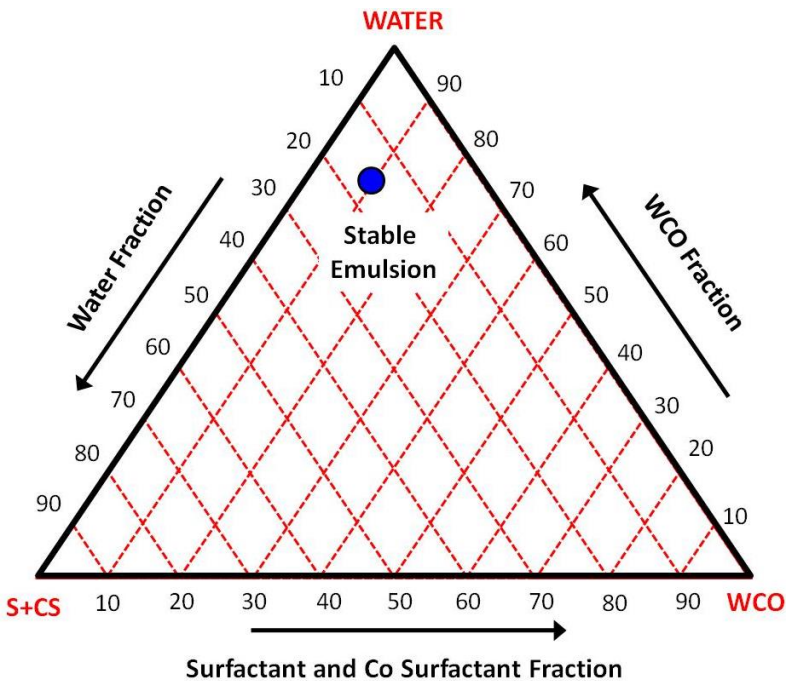
Figure 1. Ternary Diagram for stable emulsion.

SOLID NANO POWDER ADDITION

Nano fluids are the fluids with dispersed nano particles present in it. WCO- NF- EM was prepared by using an ultrasonic agitator and the mechanical stirrer as shown in Figure 2. For the work is Aluminium oxide of size 50-60 nm was selected was selected for preparing the WCO solid nano additive emulsion due to its better thermal conductivity. Initially 50 ppm of aluminium oxide nano particles was made dispersed in 15% by volume of water with help of the ultrasonicator. The ultrasonic agitator was allowed to operate at the amplitude of 20 µm with a frequency of 20 kHz spanning a period of 30 minutes aimed at the complete distribution of nano particles in water. Prepared nano powder was mixed well with WCO emulsion with the help of mechanical agitator to obtain the WCO-NF-EM. From the stability test it was observed that the nano additive with the WCO emulsion was stable for 7 days.

Figure 2. Ultrasonic agitator and mechanical stirrer arrangement.

ENGINE EXPERIMENTAL SETUP
AND EXPERIMENTS CONDUCTED

The engine utilized for this study was a constant speed, single cylinder, naturally aspirated, water cooled compression ignition engine with a rated power output of 3.7kW at 1500 rpm. Burette and stop watch arrangement was used to record the flow rate of the fuel. Engine speed was measured by an inductive pick and the torque was measured using an Eddy current dynamometer (BENZ SYSTEMS) fixed directly to the engine. An AVL NDIR exhaust analyzer was utilized for determining HC, CO and NO in the exhaust. The HC and NO emissions were recorded in terms of particles per million (ppm) and CO emission was measured as percentage by volume in standard units. Black carbon smoke levels were found with a standard AVL smoke meter. The test engine setup is presented in Figure 3.

Figure 3. Photographic view of the test engine setup.

The engine was initially run with ND and NWCO as fuels in single fuel mode at different loading conditions such as 20%, 40%, 60%, 80% and 100% loads (power outputs) to provide baseline reference. Engine experiments were repeated with WCO-EM and the WCO-NF-EM as fuels for comparison. Engine trials were initially made to optimise the injection timing for the all the methods adopted. The injection timing was varied from 21 to 29º BTDC with 2º crank angle intervals for each method. The engine's brake thermal efficiency was considered for the optimisation criteria. The injection timing with maximum brake thermal efficiency was selected as the optimal injection timing. From the experiments the fuel injection timing was optimised and set as 25º BTDC for single fuel operation and 27º BTDC for WCO, WCO-EM and WCO-NF-EM. The same injection timing was used for dual fuel operation also. The optimal injection timing for diesel was 23ºBTDC. Readings for engine speed, torque and exhaust gas temperature and fuel flow were recorded for obtaining performance parameters. Emissions were obtained from analyzers for each loading conditions. All the experiments were repeated three times to check for repeatability in measured values.

RESULTS AND DISCUSSION
ENGINE PERFORMANCE CHARACTERISTICS

Variation of brake thermal efficiency with brake power of ND, NWCO, WCO-EM and WCO-NF-EM and the WCO-NF-EM-LPG could be seen in Figure 4. It is clear from the graph, brake thermal efficiency of all the fuel increased with brake power. It can be seen that NWCO resulted in lower BTE as compared to ND operation at all power outputs. It was 24% with NWCO and 31.9% with ND at the maximum power output of 3.7 kW. The reduction in brake thermal efficiency of NWCO is due to the incomplete combustion of the highly

viscous NWCO as a result of poor atomisation and vaporisation process. However, with WCO-EM the BTE was observed to be superior at all power outputs and found as 26% at the maximum power output. The increase in BTE of WCO -EM is mainly due to the presence of water molecule in the emulsion which resulted in the micro-explosion of the emulsified fuel. Micro-explosion resulted in the secondary atomization of the injected fuel which could help in improvement in mixture preparation and paid for more amount of energy release due to complete combustion. Further increase in the brake thermal efficiency was observed with WCO-NF-EM at all power outputs as compared to WCO-EM and NWCO It could be explained that the presence of metal based catalyst (Al_2O_3) in the WCO-NF-EM increased the mixing characteristics of injected fuel and air due to its higher surface to volume ratio. The improvement in calorific value of the WCO-NF-EM may have helped in more energy release and increased the brake thermal efficiency. The BTE was noted as 27.2% with the WCO-NF-EM at peak power output.
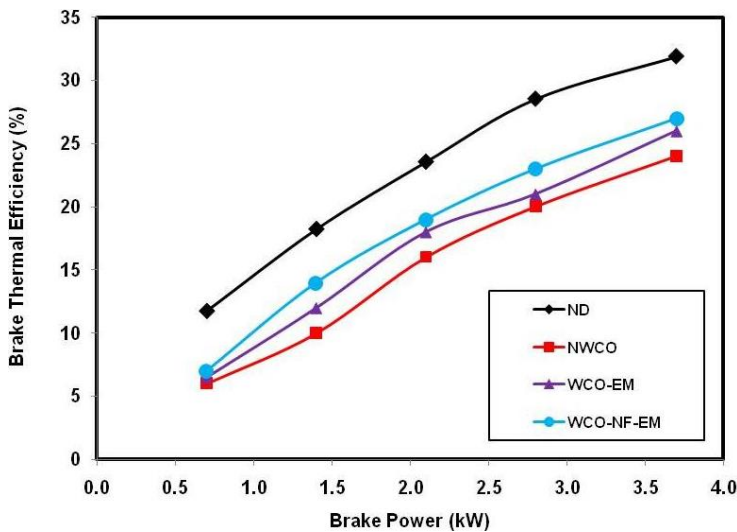
Figure 4. Variation of brake thermal efficiency with brake power.

ENGINE EMISSION CHARACTERISTICS

The variation of HC (hydrocarbon) and carbon monoxide emissions with brake power for ND, NWCO, WCO-EM, WCO-NF-EM and WCO-NF-EM-LPG can be seen in Figures 5 and 6 respectively. HC emission was found to increase with increase in brake power for all the methods. This is due to the amount of fuel supplied to be more with raise in engine power.

Due to the fixed air supply in diesel engines, the air fuel ratio becomes rich when the load is increased. Hence the oxygen availability is reduced at higher power outputs and results in higher HC emissions. NWCO resulted in higher HC emissions as compared to ND at all power outputs. The maximum value of HC was found to be 150 ppm at peak power output where as it was 80 ppm with ND. The high viscosity and slow burning nature of vegetable oil based fuels may be the reason for the increased HC emission with WCO. WCO-EM showed lower values of HC emissions at all power outputs as compared to NWCO. It can be explained by micro explosion of the emulsified fuel which improved the atomization characteristics of WCO emulsion, resulted in better mixing of fuel and air and improved the rate of combustion. Use of WCO-NF-EM reduced the HC emissions further at all power outputs as seen in Figure 5.The reduction in HC emission with the solid nano additive emulsion may be explained by the presence of oxygen in the nano powder which helped in oxidation of the hydrocarbon fuel as reported by Chandrasekaran et al. (2016). It has been reported by Mirzajanzadeh et al. (2015) that the higher surface to volume ratio of aluminium oxide may result in better mixing of air and injected fuel which helps in increased rate of combustion. All these factors may have involved in complete combustion of WCO-NF-EM. CO indicated in Figure 6 increased with increase in engine's power with all the methods as expected due to the reduced availability of oxygen for the oxidation of partially burned CO molecules. NWCO indicated very high levels of

CO emissions as compared to ND operation at all operating conditions. The value was found to be 0.42% at peak power output where as it was 0.35% with ND operation. The raise in CO emission with NWCO can be explained by the low combustion temperature of the fuel which was not sufficient to oxidise the CO formed due to inferior combustion. WCO-EM showed reduced CO emissions as compared to NWCO at all power outputs. The reduction in CO emission with the emulsified WCO can be explained by the micro explosion process which helped in complete combustion of the fuel even with the reduced peak cycle temperature. The value at peak power output was noted to be 0.3% with WCO-EM. Further reduction in CO emission was noted with the WCO-NF-EM at all power outputs. The CO was reduced further to 0.25% with the solid nano additive emulsion at peak power which is still lower than diesel value. The reduction in CO emission was noted to be 29% and 40% as compared to ND and NWCO respectively. The reduction in WCO-NF-EM could be explained by the presence of excess oxygen content of the nano additive in the fuel which supported in the oxidation of CO molecule to carbon dioxide. Thus the level of carbon monoxide emission was lower.
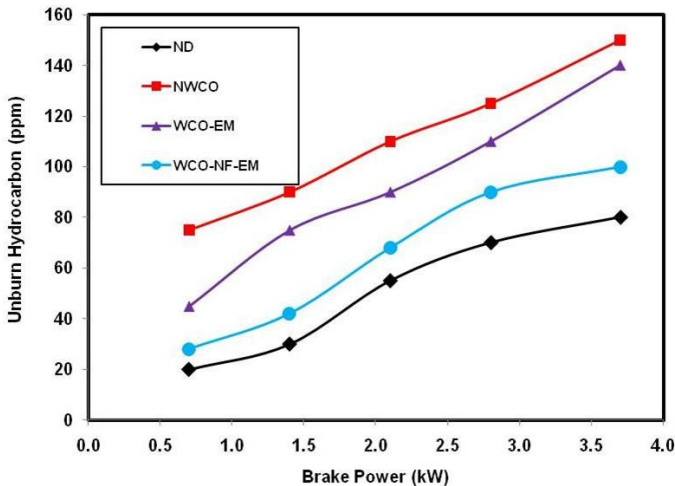
Figure 5. Variation of unburn hydrocarbon with brake power.
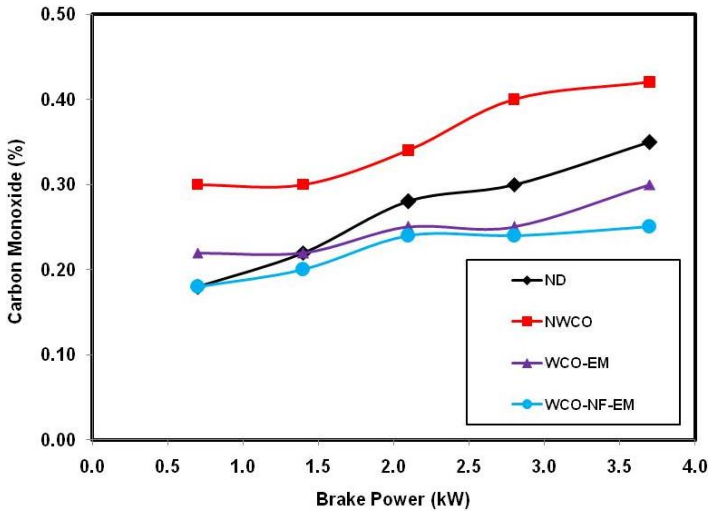
Figure 6. Variation of carbon monoxide with brake power.

The variation of oxides of nitrogen and smoke emissions with brake power can be seen in Figures 7 and 8 respectively for all the methods tried. As expected ND experienced highest oxides of nitrogen emission of all the fuels used at all power outputs. On the other hand, lesser oxides of nitrogen emission were observed with NWCO as compared to ND. The values were noted to be 300 ppm with NWCO and 350 ppm with ND at peak power output. As a result of reduced cycle temperature due to incomplete combustion of the NWCO the NOx emission was found to be lower. Conversion of WCO into its emulsion and used as fuel indicated considerable reduction in NOx emissions at all power outputs as compared to NWCO. The higher latent heat of vaporization of ethanol and water present in the emulsion absorbed more heat for their evaporation and resulted in lesser cycle temperature. Thus WCO emulsion produced 250 ppm of oxides of nitrogen emission which was comparatively lesser than neat diesel and WCO. It must be noted that the NOx emission was further reduced with the WCO-NF-EM mainly at higher power outputs. However past studies reported increase in NOx with the solid nano additive emulsion as fuel. The reduction in NOx

emission with the WCO solid nano additive emulsion could be due to the availability of less oxygen participated in formation of NOx. Referring to the Figure 7 that CO emission was minimal for the WCO-NF-EM at all power outputs which indicated that the availability of oxygen was utilised mainly for the formation of CO_2 was more. The NOx emission was recorded as 180 ppm with the WCO solid nano additive emulsion at the maximum power output.

Experimental results presented in Figure 8 indicated very high levels of smoke emissions with NWCO at all power outputs as compared to ND. The value was noted to be 90% and 60% respectively for NWCO and ND at peak power output. The very high viscosity which is about 10 times higher than ND leads to poor atomisation of the injected fuel which resulted in course droplets to be present in the combustion chamber. Poor mixture preparation due to its higher viscosity and lower volatility reported maximum smoke values with NWCO at all power outputs as compared to ND operation. However the emulsified WCO (i.e., WCO-EM) reported comparatively lesser smoke emissions (80%) as compared to NWCO. It is mainly due to the secondary atomization of injected emulsified fuel because of the phenomenon called as micro-explosion. Inclusion of aluminium oxide solid nano additive with the WCO emulsion further reduced the smoke emission of the engine operated on WCO-NF-EM to a minimum of 65%. The above statement can be supported by the higher surface to volume ratio of the nano particles which helped in the better mixture formation and resulted in the reduction of smoke emissions at all power outputs. Dual fuel operation with LPG induction further reduced the smoke values of WCO-NF-EM mainly at high power outputs. At peak power output the smoke value was observed to be 55% which is noted to be still lower than ND value. In dual fuel operation with LPG induction the smoke reduction could be explained mainly by the combustion process of the engine following the spark ignition combustion process. The smoke reductions with different methods were

noted to be 11%, 28% and 39% respectively with WCO-EM and WCO-NF-EM as compared to NWCO at peak power output.
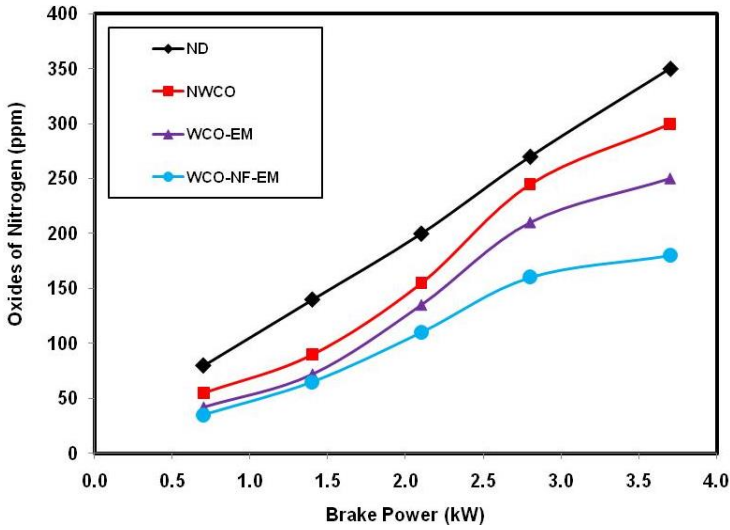
Figure 7. Variation of oxides of nitrogen with brake power.
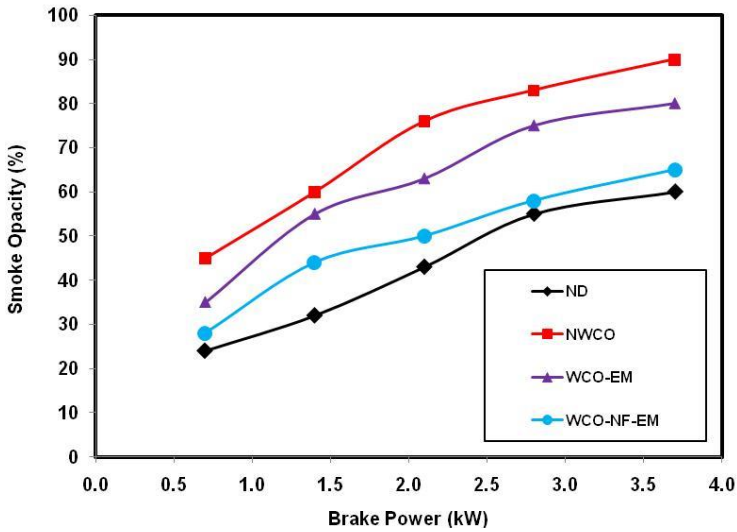
Figure 8. Variation of smoke opacity with brake power.

CONCLUSION

Effect of emulsification and solid nano powder addition on the performance of the engine and the emission characteristics of a WCO based diesel engine was studied. WCO-EM considerably increased the BTE and reduced smoke NOx, HC and CO emissions of the engine at all power outputs. Conversion of WCO-EM into WCO-NF-EM and using as fuel achieved further improvement in BTE and reduction in all emissions. It is demonstrated that the WCO can be efficiently utilized in compression ignition engines by altering it into its solid nano additive emulsion in the unmodified engine.

REFERENCES

Bora, P., Boro, J., Konwar, L. J., & Deka, D. (2016). Formulation of micro emulsion based hybrid biofuel from waste cooking oil–A comparative study with biodiesel. *Journal of the Energy Institute*, 89(4), 560-568.

Chandrasekaran, V., Arthanarisamy, M., Nachiappan, P., Dhanakotti, S., & Moorthy, B. (2016). The role of nano additives for biodiesel and diesel blended transportation fuels. *Transportation Research Part D: Transport and Environment*, 46, 145-156.

Corsini, A., Di Antonio, R., Di Nucci, G., Marchegiani, A., Rispoli, F., & Venturini, P. (2016). Performance analysis of a common-rail Diesel engine fuelled with different blends of waste cooking oil and gasoil. *Energy Procedia*, 101, 606-613.

Corsini, A., Fanfarillo, G., Rispoli, F., & Venturini, P. (2015). Pollutant emissions in common-rail diesel engines in extraurban cycle: rapeseed oils vs diesel fuel. *Energy Procedia*, 82, 141-148.

da Silva, M. A. V., Ferreira, B. L. G., da Costa Marques, L. G., Murta, A. L. S., & de Freitas, M. A. V. (2017). Comparative study of NOx

emissions of biodiesel-diesel blends from soybean, palm and waste frying oils using methyl and ethyl transesterification routes. *Fuel*, 194, 144-156.

Hemanandh, J., & Narayanan, K. V. (2015). Emission and performance analysis of hydrotreated refined sunflower oil as alternate fuel. *Alexandria Engineering Journal*, 54(3), 389-393.

Hwang, J., Bae, C., & Gupta, T. (2016). Application of waste cooking oil (WCO) biodiesel in a compression ignition engine. *Fuel*, 176, 20-31.

Jamuwa, D. K., Sharma, D., & Soni, S. L. (2016). Experimental investigation of performance, exhaust emission and combustion parameters of stationary compression ignition engine using ethanol fumigation in dual fuel mode. *Energy Conversion and Management*, 115, 221-231.

Knežević, D., Tomić, M., Stajić, V., Petrović, V., & Bulatović, Ž. (2015). The characteristics of combustion process of diesel engine using vegetable oil methyl esters. *Thermal Science*, 19(6), 2255-2263.

Kumar, M. S., & Jaikumar, M. (2014). A comprehensive study on performance, emission and combustion behavior of a compression ignition engine fuelled with WCO (waste cooking oil) emulsion as fuel. *Journal of the Energy Institute*, 87(3), 263-271.

Kumaraswamy, A., & Prasad, B. D. (2012). Performance analysis of a dual fuel engine using LPG and diesel with EGR system. *Procedia Engineering*, 38, 2784-2792.

Lata, D. B., & Misra, A. (2010). Theoretical and experimental investigations on the performance of dual fuel diesel engine with hydrogen and LPG as secondary fuels. *International Journal of Hydrogen Energy*, 35(21), 11918-11931.

Mirzajanzadeh, M., Tabatabaei, M., Ardjmand, M., Rashidi, A., Ghobadian, B., Barkhi, M., & Pazouki, M. (2015). A novel soluble nano-catalysts in diesel–biodiesel fuel blends to improve diesel

engines performance and reduce exhaust emissions. *Fuel*, 139, 374-382.

Monirul, I. M., Kalam, M. A., Masjuki, H. H., Zulkifli, N. W. M., Shahir, S. A., Mosarof, M. H., & Ruhul, A. M. (2017). Influence of poly (methyl acrylate) additive on cold flow properties of coconut biodiesel blends and exhaust gas emissions. *Renewable Energy*, 101, 702-712.

Nadar, K. N., & Reddy, R. P. (2008). Combustion and emission characteristics of a dual fuel engine operated with mahua oil and liquefied petroleum gas. *Thermal Science*, 12(1), 115-123.

Palanimuthu, V., & Nagarajan, G. (2010). Performance, emission, and combustion characteristics of a CI engine using liquid petroleum gas and neem oil in dual fuel mode. *Thermal Science*, 14(4), 923-935.

Qu, L., Wang, Z., & Zhang, J. (2016). Influence of waste cooking oil biodiesel on oxidation reactivity and nanostructure of particulate matter from diesel engine. *Fuel*, 181, 389-395.

Saxena, V., Kumar, N., & Saxena, V. K. (2017). A comprehensive review on combustion and stability aspects of metal nanoparticles and its additive effect on diesel and biodiesel fuelled CI engine. *Renewable and Sustainable Energy Reviews*, 70, 563-588.

Tira, H. S., Herreros, J. M., Tsolakis, A., & Wyszynski, M. L. (2012). Characteristics of LPG-diesel dual fuelled engine operated with rapeseed methyl ester and gas-to-liquid diesel fuels. *Energy*, 47(1), 620-629.

Tomić, M. D., Savin, L. Đ., Mićić, R. D., Simikić, M. D., & Furman, T. F. (2013). Effects of fossil diesel and biodiesel blends on the performances and emissions of agricultural tractor engines. *Thermal Science*, 17(1), 263-278.

Chapter 7

SYNTHESIS TECHNIQUES OF NANOSTRUCTURED MATERIALS AND ITS IMAGE ANALYSIS FOR PARTICLE SIZE DISTRIBUTION

G. Padmalaya, B. S. Sreeja and G. Kavitha[*]

[1]Department of Electronics and Communication Engineering,
SSN College of Engineering, Chennai, India
[2]Department of Electronics Engineering,
Madras Institue of Technology, Chromepet, Chennai, India

ABSTRACT

The most critical challenge in nanotechnology is the ability to characterize structures created by nanoparticle (NP) which gets assembled with prescise engineered properties. An exploration pushes to control the spatial dispersion of NPs traverses a tremendous scope of nanomaterials and its physical properties that directs towards the diverse

---

[*] Corresponding Author's Email: kavithagmit@gmail.com.

applications. In this chapter, an outline of various synthesis routes for obtaining structural NPs such as metal oxide and metal NPs has been discussed. The analysis of nanostructured materials with its properties has been diversified for image processing which endures the measurement on size distribution specifically for soot nanoparticles. The same has been discussed elaborately using Euclidian distance mapping -Surface based scale (EDM-SBS) analysis.

Keywords: nanomaterials, synthesis, nanostructures, soot particles, image processing

The most critical challenge in nanotechnology which has an ability to characterize more predominant structures created by nanoparticle (NP) gets assembled with precise engineered properties. An exploration pushes to control the spatial dispersion of NPs transverses a tremendous scope of nanomaterials and its physical properties that directs towards the diverse applications. In this chapter, an outline of various synthesis routes for obtaining structural NPs such as metal oxide and metal NPs has been discussed. Moreover discussion based on analysis of nanostructured materials with its properties has been diversified for image processing which endures the measurement on size distribution specifically for soot nanoparticles has been elaborated with EDM-SBS algorithm.

INTRODUCTION

Nanotechnology manages "nanoscale" materials with structures and synthesis routes dealing with high standards of applications. Despite the fact that the word "nanoscale" is largely considered to speak with prescribed size 1 nm to 100 nm. It is understood that "nano" is small and its appreciable uses with this context are overwhelming. For

instance, the upper end of the nanoscale is 100 nm which is thickness of the strand of human hair split 100 times.

The fantastic and favourable circumstances root of the nanotechnology showed kind qualities which includes surface area to volume ratio and quantum effects for numerous materials. These facts additionally improve the material properties such as strength, reactivity, electrical, optical characteristics and etc., (Gunasekaran, 2014). During last decades, the characteristic features for nanoparticles made the fluctuating dependence properties on size, temperature and inter-particle interaction has been investigated extensively. For understanding the size distribution of nanoparticles it is essential to have a contingent ability on experimental results. Electron Microscopic techniques are commonly applied to estimate such particle size distributions. With the specific end goal to acquire dependable size distributions, it is important to accomplish the PC method which is attractive for determining the particle sizes.

The utilization of picture examination to characterize particle gatherings is an entrenched practice in material science. As early as in 1979, Forrest and Witten Jr. utilized picture investigation of transmission electron micrographs to distinguish and consider the fractal structure of smoke molecule aggregates. From that point onward, picture examination has been utilized to describe colloidal and NP totals as far as different properties. For instance, the size circulation of such totals has been investigated by indigenously created picture examination methodology or by means of open space picture handling software. While few have focused in general picture investigation programming, for example, Image J can play out the sort of molecule distinguishing proof and checking required for ascertaining NP total sizes. Specifically, NPs are known to collect into perplexing, higher-arrange structures, for example, strings, fractal trees, sheets, and permeating systems that require more detailed measurements for portraying their shape, self-likeness and topology. While a few examinations have broken down the fractal measurement and shape

measurements of NP totals through picture investigation and, most of the time, the techniques were robotized (Murthy et al., 2015).

In this chapter, different synthesis routes of nanoparticles and characteristic properties investigation by various imaging software techniques are discussed elaborately.

TYPES OF NANOPARTICLES

There is a consideration and expanding research exercises in the behavior and fate results of nanomaterials. The synthesis and preparatory techniques of nanoparticles provides the behavioral understanding in studying the characteristics properties using software based image analysis. The surface and quantum properties of NPs extends their impacts for making wonders with their molecules leading to their physiochemical properties which forms a mainstream for researchers. Novel nanoscale properties have been abused by means of modern nanotechnology to deliver the tremendous amount of engineered NPs to serve for special purposes.

Considerable methods have utilized to produce nanoparticles, these methods have progressed quickly and keep on improving the generation on controlled shape and size of the developed nanoparticles. Shenhar & Rotello (2003) discussed about two distinguished methodologies which were used to obtain nanostructures called bottom up method. The other technique was top down approach where the molecules are composed from diminution of ions which are amassed to generate nanostructures. These two methods are implemented in gas, supercritical fluids, liquids, in vacuum and as solid states and additionally, numerous critical points for enhancing the physical properties such as size, shape, distribution, composition and degree of agglomeration. The stabilization of the particles considered to be one of the important aspects to avoid coalescence and aggregation and it can occur in many different ways.

Numerous kinds of nanomaterial have been created for various applications and business exercises. Metal oxides are imperative inorganic nanoparticles because of the novel optical, attractive and electrical properties. Metal oxides NPs are utilized in numerous appropriate exercises including sensors, catalysis, biomedical diagnostics, ecological remediation and electronic materials. The accompanying exchange features the preliminary systems, focal points and burdens of most normal NPs (Iron oxide, Titanium oxide, Cerium oxide, Zinc oxide) and metal NPs (Silver, Gold) (Lee & Ahmed, 2016).

There are two most normal types of iron oxide NPs (γ-Fe_2O_3 and magnetite Fe_3O_4) and they offer a high potential for a few biomedical applications because of their super-attractive properties, this applications including tissue repair; attractive reverberation imaging, medicate conveyance and hyperthermia (Ali et al., 2016). The examination of its belongings against natural contaminants utilizing picture processing approach are discussed in later segment.

Titanium dioxide has four precious cystal structures in particular: brookite, rutile, anatase and TiO_2. They may be integrate dutilizing some imperative systems:co-precipitation, sol–gel synthesis process, synthetic vapor statement, reverse micelle synthesis, micro emulsion synthesis process and hydrothermal reaction method. It is essential that the changing conduct from the indistinct to the anatase stage isaffected by the assembling conditions. NPs are misused by an assortment of fields because of their appealing properties as a high refractive list, light ingestion/diffusing particularly with ease generation of compound relatively titanium dioxide. Titanium oxide has an extensive variety of utilization, for example, pigments, cosmetics, catalysts and photocatalysts (Chen & Mao, 2007).

Zinc Oxides in nanoscale have received the logical consideration as of late because of thei rproperties and its capacities are relevant in numerous fields. They have become imperative part in biomedical and antimicrobial operators (Shi et al., 2014). A great deal of literary works are specified on a few amalgamation strategies, for example, chemical

vapour deposition, thermal decomposition, spray pyrolysis, laser ablation, sol-gel method, molecular beam epitaxy and hydrothermal synthesis have contemplated for the synthesis of ZnO nanostructures and also improved their new path of different applications by modifying the surfaces with organic compounds (Brayner et al., 2010).

Nanoscale metals can be fabricated in numerous shapes and sizes relying upon the coveted properties which make the particles not the same as both mass and atomic structure of materials (Di Guglielmo et al., 2010). Some critical applications exploited novel nanoscale viewpoints, similar to antimicrobial uses to water cleansings or waste water treatment. In addition, execution of fabricated NPs with different strategies are connected to tune the size and shape of particles focusing for particularpurpose (Tedesco et al., 2010).

SYNTHESIS AND CHARACTERISATION OF NANOPARTICLES

The nanoparticles have made the great attention towards various applications due to their mechanical, electrical, optical and magnetic properties owing to their dimenions 0 to 100 nm, as these are called nanopowders (Lee & Ahmed, 2016) obtained from the techniques suchas bottom-up and top-down approaches which was discussed in preparatory techniques for Ag NPs and Au NPs. This part deals with some of the common processes that have been used in recent years for the preparation of NPs in many laboratories.

SYNTHESIS OF IRON OXIDE NPS

A comparision of various techniques for preparingiron oxide NPs and their advantages/disadvantages are shown in Table 1.

Table 1. A comparision of various synthesis routes of iron oxide NPs with respect to morphology, size, advantages and disadvantages

S. No	Method	Product Morphology	Advantages	Disadvantages
1.	Physical Deposition of gas phase Electron beam lithography	Spheres and irregular spheres Spheres and rods	Easy to prepare Controlled interparticle spacing	Size control is difficult Requires expensive and highly complex machines to operate
2.	Chemical Sol-gel Oxidation	Spheres, irregular spheres Porous and nonporous spheres or spindles, elongated small spheres	Controlled size formation and internal structure	High premeability, weak bonding, low wear resistance Maintainence of precise stoichiometric phase High temperature reaction It requires continuous or segmented mixing of reagents Inability to reproduce Requires very high temperatures Difficulty in understanding the mechanism Complicated Conditions
	Chemical Oxidation	Spheres	Simple and effective	
	Hydrothermal	Elongated, compact irregular spheres and numerous shapes	Particle size and shapes are controllable	
	Flow injection	Small rods, irregular spheres, sheets or rhombic shapes	Homogeneity with high mixing with a accurate control of the procedure and good reproducibility	
	Electrochemical	SphericalNPs, nanorods, hexagonal nanocrystals and facets	Controllable particle size	
	Aerosol/Vapour phase	Mesoporous single crystals and small particles	Large-scale products	
	Sono chemical deposition	Bi pyramids, spheres or truncated rods	Size distribution in narrow particle	
	Using nanoreactors	Spheres, hollow and spherical NPs	Likelihood to specifically control the size of NPs	
3.	Biological Microbial incubation	Small platelets, spherical or rods like spheres and irregular spheres	Good reproducibility, scalability, high yield and lowcost	Slow and laborious

Synthesis of Titanium Di Oxide Nanoparticles

Titanium di-oxide (TiO_2) has been broadly utilized in the field of pigment, sunscreens, paints salves and toothpastes. In 1972, Fujishima and Honda found the wonder of photocatalytic part of water on TiO_2 electrode under ultraviolet (UV) light. Many efforts has been made onwards to TiO_2 material which are used in many applications from photovoltaics to sensors (Chen and Mao, 2007). These applications can be generally isolated into two groups such as energy and environment. Various methods has been adopted to prepare the TiO_2 nanoparticles and those techniques are tabulated in Table 2.

Table 2. Various methods of preparation of TiO_2 nanoparticles

S. No	Techniques	Morphology obtained	Advantages	Disadvantages
1.	Sol-Gel method	Nanorods, spheres, hexagonal, nanowires, nanocubes	Highlyporous with high surface area, low density material is formed	Proper pH, temperature has to be maintained
2.	Micelle and Inverse micelle method	Shuttle like round shape	High cystallinity	Due to various phase formation, structure maintanence was difficult
3.	Hydrothermal	Nanorods, nanowires, nanosheets, nanotubes	Simple and easy process	Under prescribed ratio and temperature is maintained
4.	Solvothermal	Nanodumbells, nanowires, nanorods in flower morphology	Under different solvent conditions structures are formed	Higher concentration of solvents affects the polarity and solution viscosity
5.	Sonochemical method	Nanowhiskers, mamotubes	High surface area	Ultrasound radiation is used
6.	Microwave method	Nanowires, nanotubes	Rapid heat transfer, volumetric and selective heating	High frequency produces losses and inability.

SYNTHESIS OF ZINC OXIDE NPS

A few techniques including sol-gel strategy, hydrothermal synthesis, mechano-chemical technique and vapor phase method have been received for the formulation of ZnO nanoparticles. ZnO nanoparticles can be acquired by these strategies through altering parameters, for example, temperature, pressure, the hydrolysis proportion and precursors. All synthesis methods of ZnO nanoparticles mentioned in this paper can also be conducted on a laboratoryscale. In addition, the similar synthesis methods are applicable to ZnO nanoparticles as like TiO_2 nanoparticles (Table 1) which also carries a like morphological features based advantages and disadvantages.

SYNTHESIS OF GOLD AND SILVER NPS

Gold NPs with their large surface area and high electron conductivity they are diversely used in biomedicine and other applications like biosensors. At nanometeres range, it was monitored for enhnacing the binding energy with biological cells. This was expected to happen due to permeability and retention property of NPs that tends to accumulate for interacting with biocells. These gold NPs are synthesized using physcial and chemical routes. One of the popularly speaking physical method was laser ablation method (Madu et al., 2011) in which material is allowed to pass laser radiation to break the material into nm range. Further, by surface modification with polymers and enzymes the electrontransfer rate can be increased. Their applications was enormous in which some of the popular applications are biosensor, drug delivery agents, immuno sensor, cancer therapheutics, that means it forms a construction block for nanotechnology. Moreover, structural design forms an alternative for

generation of important properties like non toxic and biocompactible (Chen et al., 2008).
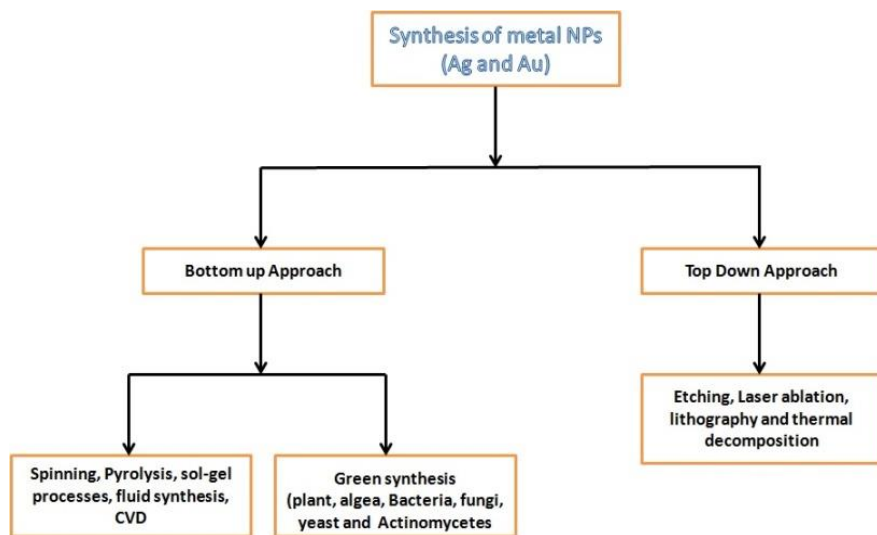
Figure 1. Various methods for synthesizing gold and silver NPs.

Silver NPs forms most fascinating material with typical properties such as good conductivity, chemcial stability, catalytic activity and antimicrobial activity. They are also playing major role in water and air filtration applications. Surface coated Ag NPs are highly showed excellent activity towardsv arious applications such as paint, anitmicrobial, antibacterial, sensitive detection etc. Figure 1 shows the common synthesis routes for the preparation of Au and Ag NPs.

NANOSTRUCTURAL IMAGE ANALYSIS USING IMAGE PROCESSING

The most prime significance for nanoparticles is characterized which is utilized to give logical parameters particularly on microscopic based structural investigations; size and morphology are driving the part

for the conduct properties of nanoparticles. For uniform size particles, the size can be effectively decided by using particle size analyser. The determination of different size scales was determined by behavioral properties of nanoparticles and this can be more apt for aggregated particles. (Bescond et al., 2014) reported on aggregated particles carrying the normal size was analysed by TEM analysis for soot application and it was also found that primary particle size can also be calculated. For accurate measurement of size distributions, the primary particle diameter indicating nonspherical shaped nanoparticles has been considered (Barone et al., 2006) Aggregate size investigations, involving size distributions especially for primary sphere diameter was determined by in situ methods such as small angle X-ray scattering (SAXS), laser indued incandescence with optical were used without disturbing the environment.

Figure 2(a) and (b) are scanning electron micrographs of (a) rGO/ZnO nanocomposite with nano rice like structure and (b) shows the spherical shape of chitosan/ZnO nanocomposite. These micrographs are digitized and stored as 1, 024 x1, 024 pixel images.
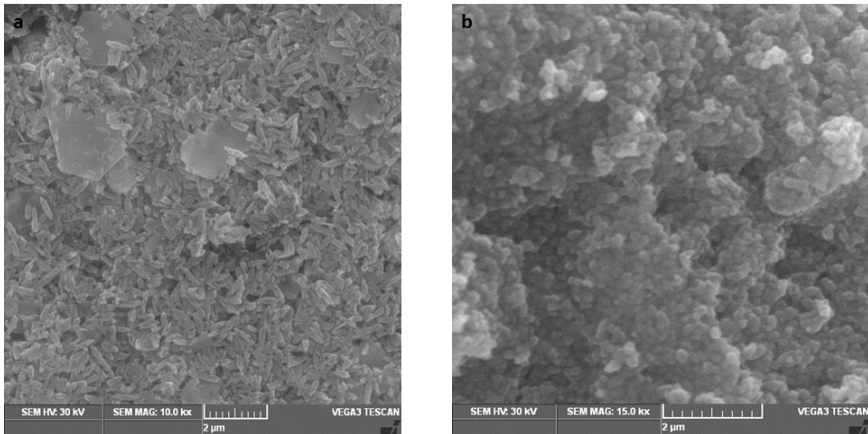
Figure 2. (a) SEM image of rGO/ZnO nanocomposite and (b) Chitosan/ZnO nanocomposite.

The measurements based on sampling for the nanoparticles was carried out by posteriori analysis which comes under the ex-situ techniques specially meant for investigating the microscopical structural images such as transmission electron microscopy (TEM) and scanning electron microscopy (SEM). For agglomerated morphologies the determination of size based on TEM analysis relies on (D_p, D_f) indicating the controlled postprocessing and faster processing of images. Some of the authors (Bescond et al., 2014) reported on soot origins with different statistical levels that forms distribution (D_p) suggesting the normal and lognormal distribution. Another algorithm used for determining the primary particle size distribution for TEM images known as modified Hough transforms. Its was found to be more effective for detecting spherical and well contrasted particles that are aligned at the border of aggregated particles.

For overlapped and necked effects, Euclidian distance mapping surface –Based Scale Analysis (EDM-SBS) was carried out which is used for describing the atomization process and was first introduced by (Danielsson, 1980). Especially, for soot size determination, A. Bescond et al., carried out EDM-SBS for studying the surface function with scaling of 2k+1 by known parameter image resolution (R) expressed in pixels per nanometer, there is possibility for converting the scale diameter D into nanometers and image surface into square nanometers.

$$D = (2K+1)/R \quad \text{surf} = N_{pixel}/R^2 \tag{1}$$

EDM-SBS function is also called as surf function (D) for processing an image in aggregated form. From the images analysed by authors (Lu & Sorensen, 1994) aggregate image corresponds to pherical structure with diameters 30 to 60 nm. For N aggregate images, the normalized surf function was found to be D=0 indicating the average surf function for aggregates of different sizes and orientations. It should be understood that, surf function for determining length of aggregates

was not same and at the same time the determination of the S function for larger scales may suffer of lack of statistics.

PARAMETRIC STUDY OF THE EDM-SURFACE-BASED SCALES ANALYSIS WITH WELL-DEFINED VIRTUAL AGGREGATES

For virtual aggregates, the primary particle size was determined and generated by "DLCA" (Diffusion Limited Cluster Aggregation) algorithm similar to that developed by Hayashi (Hayashi et al., 1999; Bescond et al., 2014). It forms a set of structures carrying normal or lognormal distribution aligned randomly in virtual 3D position and also specially meant for aggregated nanoparticles which has tendency to collide each other with thermal disturbances. This algorithm is focused for point contact indicating the nanoparticles touches on a single point. For calculating parameters like reso and P, 3D images were projected on a 2D space for manipulating the TEM pictures.

According to (Sorensen & Roberts, 1997; Brasil et al., 1999), virtual aggregates carrying primary particle size was analysed using the parameters corresponding to different $D_{p, mod}$, σ_p for normal distributions and $D_{p,geo}$, $\sigma_{p,geo}$ for lognormal distributions. The measured values for aggregates generated by combustion processes attributing to fractal dimensions D_f lie between 1.66 and 1.87 and prefactor k_f fluctuates from 1.13 to 1.47 respectively (Hayashi et al., 1999; Seuk-Cheun & Seul-Hyun, 2018).

It was understood that, EDM-SBS analysis is excellent morphological descriptor. To be sure, this method plainly underlines the contrast between point contact circles and genuine agglomerates. Extra advancements on this technique could prompt deciding different parameters than essential circle breadth conveyance, for example, covering among circles and necking impacts.

CONCLUSION

Nanotechnology based applications made the beginning and lightened up our lives with their significant factors. The nanostructural synthesis routes for various nanomaterials discussed in this chapter are only a small subset of a vast range of techniques that are available. The applications for each nanomaterial have been covered as outline in this chapter. Image analysis using TEM images for soot NPs using EDM-SBS analysis and their benefits are highlighted. For engineered nanomaterials with different particle characteristics, image analysis has to be implemented based on size distribution analysis in near future.

REFERENCES

Ali, A., Hira Zafar, M. Z., ul Haq, I., Phull, A. R., Ali, J. S., & Hussain, A. (2016). Synthesis, characterization, applications, and challenges of iron oxide nanoparticles. *Nanotechnology, Science and Applications*, 9, 49.

Barone, T. L., Lall, A. A., Zhu, Y., Yu, R. C., & Friedlander, S. K. (2006). Inertial deposition of nanoparticle chain aggregates: theory and comparison with impactor data for ultrafine atmospheric aerosols. *Journal of Nanoparticle Research*, 8(5), 669-680.

Bescond, A., Yon, J., Ouf, F. X., Ferry, D., Delhaye, D., Gaffié, D., ... & Rozé, C. (2014). Automated determination of aggregate primary particle size distribution by TEM image analysis: application to soot. *Aerosol Science and Technology*, 48(8), 831-841.

Brasil, A. M., Farias, T. L., & Carvalho, M. G. (1999). A recipe for image characterization of fractal-like aggregates. *Journal of Aerosol Science*, 30(10), 1379-1389.

Brayner, R., Dahoumane, S. A., Yéprémian, C., Djediat, C., Meyer, M., Couté, A., & Fiévet, F. (2010). ZnO nanoparticles: synthesis,

characterization, and ecotoxicological studies. *Langmuir,* 26(9), 6522-6528.

Chen, P. C., Mwakwari, S. C., & Oyelere, A. K. (2008). Gold nanoparticles: from nanomedicine to nanosensing. *Nanotechnology, Science and Applications*, 1, 45.

Chen, X., & Mao, S. S. (2007). Titanium dioxide nanomaterials: synthesis, properties, modifications, and applications. *Chemical Reviews*, 107(7), 2891-2959.

Danielsson, P. E. (1980). Euclidean distance mapping. *Computer Graphics and Image Processing*, 14(3), 227-248.

Di Guglielmo, C., López, D. R., De Lapuente, J., Mallafre, J. M. L., & Suàrez, M. B. (2010). Embryotoxicity of cobalt ferrite and gold nanoparticles: a first in vitro approach. *Reproductive Toxicology*, 30(2), 271-276.

Gunasekaran, S. (2014). 8 Nanotechnology for Food: Principles and Selected Applications. *Food Processing: Principles and Applications*, 171-205.

Hayashi, S., Hisaeda, Y., Asakuma, Y., Aoki, H., Miura, T., Yano, H., & Sawa, Y. (1999). Simulation of soot aggregates formed by benzene pyrolysis. *Combustion and Flame*, 117(4), 851-860.

Lee, Y. S., & Ahmed, A. I. (2016). Synthesis Techniques and Evaluation Methods of Nanoparticles as Fungicides. In *Advances and Applications through Fungal Nanobiotechnology* (pp. 141-168). Springer, Cham.

Lu, N., & Sorensen, C. M. (1994). Depolarized light scattering from fractal soot aggregates. *Physical Review*, 50(4), 3109.

Madu, A., Njoku, P., Iwuoha, G., & Agbasi, U. M. (2011). Synthesis and characterization of gold nanoparticles using 1-alkyl, 3-methyl imidazolium based ionic liquids. *International Journal of Physical Sciences*, 6(4), 635-640.

Murthy, C. R., Gao, B., Tao, A. R., & Arya, G. (2015). Automated quantitative image analysis of nanoparticle assembly. *Nanoscale,* 7(21), 9793-9805.

Seuk-Cheun Choi & Seul-Hyun Park (2018) Quantitative Image Analysis of Carbon Nanostructure of Particles Produced from Combustion Process. *J. Nanosci. Nanotech* 18, 2148-2151.

Shenhar, R., & Rotello, V. M. (2003). Nanoparticles: scaffolds and building blocks. *Accounts of Chemical Research*, 36(7), 549-561.

Shi, L. E., Li, Z. H., Zheng, W., Zhao, Y. F., Jin, Y. F., & Tang, Z. X. (2014). Synthesis, antibacterial activity, antibacterial mechanism and food applications of ZnO nanoparticles: a review. *Food Additives & Contaminants: Part A*, 31(2), 173-186.

Sorensen, C. M., & Roberts, G. C. (1997). The prefactor of fractal aggregates. *Journal of Colloid and Interface Science,* 186(2), 447-452.

Tedesco, S., Doyle, H., Blasco, J., Redmond, G., & Sheehan, D. (2010). Oxidative stress and toxicity of gold nanoparticles in Mytilus edulis. *Aquatic Toxicology*, 100(2), 178-186.

ABOUT THE EDITORS

K. Kamalanand, PhD
Assistant Professor
Department of Instrumentation Engineering, MIT Campus,
Anna University, Chennai, India

Dr. K. Kamalanand completed his PhD at MIT Campus, Anna University. At present he is an Assistant Professor at the Department of Instrumentation Engineering, Madras Institute of Technology Campus, Anna University, Chennai, India. His research focuses on biomedical nanotechnology and mathematical modeling of systems.

D. Najumnissa Jamal, PhD
Professor
Electronics and Instrumentation Engineering,
B. S. Abdur Rahman Crescent Institute
of Science & Technology, India

Dr. D. Najumnissa Jamal received her PhD from Anna University in the field of Medical Electronics. She has been working at Crescent Engineering College since 1990, in various positions. At present she is a

Professor in the Department of Electronics and Instrumentation Engineering, B.S.A. Crescent Institute of Science and Technology, India. Her area of research includes Bio-Medical Engineering and Artificial Intelligence.

P. Mannar Jawahar, PhD

Vice Chancellor of Karunya Institute of Technology and Sciences,
Senior Professor (Rtd.) and
8th Vice Chancellor of Anna University, Chennai, India

Dr. P. Mannar Jawahar completed his PhD at I.I.T. Delhi and subsequently did his Post Doctoral Research work at Warsaw University of Technology, Poland. He joined Anna University, Chennai, India, as a Faculty in 1978 and has put in more than three decades of service in the teaching profession in various capacities. He served as the Vice Chancellor of Anna University from June 2008 to June 2012. At present, he is the Vice Chancellor of Karunya Institute of Technology and Sciences.

LIST OF REVIEWERS

Anamul Islam

Motor Control & NeuroRecovery Lab, College of Staten Island, City University New York, US

J. Sakthi Swarrup

Centre for Nanotechnology Research, Vellore Institute of Technology, India

M. Murugappan

Department of Electronic and Communications Engineering, Kuwait College of Science and Technology, Kuwait

A. Bakiya

Department of Instrumentation Engineering, MIT Campus, Anna University, India

A. Paramasivam

Department of Instrumentation Engineering, MIT Campus, Anna University, India

C. N. Savithri
Department of Electronic and Communications Engineering, Sri Sairam Engineering College, India

G. Shanthakumari
Department of Electronic and Communications Engineering, Sri Sairam Engineering College, India

INDEX

O

P

R

S

T

Related Nova Publications

FIRST-PRINCIPLE VS. EXPERIMENTAL DESIGN OF NANOMATERIALS
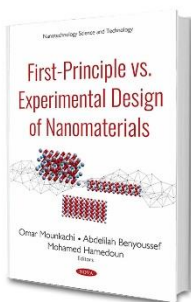
AUTHORS: Omar Mounkachi, Abdelilah Benyoussef, and Mohamed Hamedoun

SERIES: Nanotechnology Science and Technology

BOOK DESCRIPTION: The first-principle approach is designed for the interpretation of the experimental observations and prediction of properties for new nanomaterials. The understanding of physical phenomena requires a description at the atomic scale where size and geometric organization play important roles.

SOFTCOVER ISBN: 978-1-53613-984-6
RETAIL PRICE: $95

FIRST-PRINCIPLE VS. EXPERIMENTAL DESIGN OF DILUTED MAGNETIC SEMICONDUCTORS
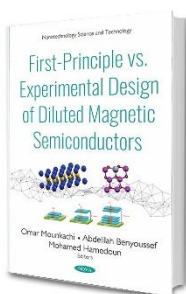
AUTHORS: Omar Mounkachi, Abdelilah Benyoussef, and Mohamed Hamedoun

SERIES: Nanotechnology Science and Technology

BOOK DESCRIPTION: Recent discoveries have given rise to a new class of electronics known as "spin electronics" or "spintronics," which uses the electron spin rather than its charge to create polarized currents. Spintronics is currently experiencing an extraordinary development with the manufacture of nanoscale devices based on ferromagnetic materials and semiconductors.

HARDCOVER ISBN: 978-1-53614-077-4
RETAIL PRICE: $195

To see complete list of Nova publications, please visit our website at www.novapublishers.com